THE HONG KONG
POLYTECHNIC UNIVERSITY
香港理工大學
Pao Yue-kong Library
包玉剛圖書館

Copyright Undertaking

This thesis is protected by copyright, with all rights reserved.

By reading and using the thesis, the reader understands and agrees to the following terms:

1. The reader will abide by the rules and legal ordinances governing copyright regarding the use of the thesis.
2. The reader will use the thesis for the purpose of research or private study only and not for distribution or further reproduction or any other purpose.
3. The reader agrees to indemnify and hold the University harmless from and against any loss, damage, cost, liability or expenses arising from copyright infringement or unauthorized usage.

If you have reasons to believe that any materials in this thesis are deemed not suitable to be distributed in this form, or a copyright owner having difficulty with the material being included in our database, please contact lbsys@polyu.edu.hk providing details. The Library will look into your claim and consider taking remedial action upon receipt of the written requests.

Pao Yue-kong Library, The Hong Kong Polytechnic University, Hung Hom, Kowloon, Hong Kong

http://www.lib.polyu.edu.hk

THE HONG KONG POLYTECHNIC UNIVERSITY

DEPARTMENT OF MECHANICAL ENGINEERING

DEVELOPMENT OF A BROADBAND SILENCER IN FLOW DUCT

WANG CHUN-QI

A thesis submitted in partial fulfillment of the requirements for the Degree of Doctor of Philosophy

December, 2007

CERTIFICATE OF ORIGINALITY

I hereby declare that this thesis is my own work and that, to the best of my knowledge and belief, it reproduces no material previously published or written, nor material that has been accepted for the award of any other degree or diploma, except where due acknowledgement has been made in the text.

_____(Signed)

WANG CHUN-QI

DECEMBER, 2007

ABSTRACT

A broadband passive silencer, which works effectively in the low frequency range in a flow duct, is developed in the present work. When a segment of a rigid duct is replaced by a plate backed by a hard-walled cavity, grazing incident sound waves induce plate bending motion, hence sound reflection. The principle of acoustic energy conservation guarantees that, whatever amount of sound reflection is, the same amount of reduction is induced in the sound energy flux transmitted to the downstream of the device. As the sound reflection is solely caused by the vibration of the plate, such a device is called plate silencer. The present study focuses on the theoretical modelling, the performance optimization, as well as the experimental realization of the proposed plate silencer.

A two-dimensional analytical model is first established for a typical plate silencer which consists of an expansion chamber with two side-branch cavities covered by light but stiff plates. The leading and trailing edges of the plate can be either simply supported or clamped, while the other two lateral edges are set free. The plate response to a grazing incident wave is formulated by solving the fully coupled dynamic equations of motion of the plate and acoustic radiation. Mean flow effect is taken into account in the analytical modelling. The theoretical model is tested experimentally using balsawood. The spectral peaks and shapes of the measured transmission loss curve are in agreement with those calculated theoretically. Attempts are made to account for the considerable sound absorption in the test rig.

Silencing performance of the plate silencers is studied and optimized based on the validated theoretical model. It is found that the clamped boundary condition is

easier to implement in practice than the simply supported one, but the stopband of the clamped plate silencer shrinks and the lower band limit is pushed to higher frequency. Theoretical study suggests that the performance of the clamped plate silencer can be enhanced by adopting nonuniform plates with softer ends. Analyses show that the performance improvement is attributed to the increased acoustic radiation efficiency over the bulk length of the nonumiform plate, which behaves like a rigid plate. The acoustic benefit of using three-dimensional configurations in a plate silencer is also investigated with a verified finite element model. Simulation shows that the three-dimensional design expands the bandwidth in both lower and higher frequency regions. Hybrid arrangement, which combines plate silencer and traditional dissipative chambers in parallel, is also studied to achieve a silencer effective from low to high frequency range.

Theoretical studies show that a good plate silencer requires light but extremely stiff plates, which are out of the reach of existing homogeneous materials. Hence, the feasibility of using sandwich construction is explored. A broadband low frequency plate silencer is realized using sandwich plate and experimentally tested. The prototype plate silencer demonstrates much better silencing performance than the expansion chamber of the same geometry (duct cross section: 100 mm×100 mm; expansion ratio: 3), with a stopband from 133 Hz to 274 Hz in which the transmission loss is higher than 10 dB over the whole frequency band. The possibility of modelling the sandwich plate silencer using a simplified mathematical model is also investigated. As far as low frequency is concerned, the experimental results are in fair agreement with the predictions. Sandwich plates with different mechanical properties are also tested and compared, which partially confirms the theoretical findings on the effect of plate properties on the silencer performance.

LIST OF PUBLICATIONS ALREADY PUBLISHED, ACCEPTED OR SUBMITTED

Refereed Journal Articles:

Wang Chunqi, Han Jun and Huang Lixi, (2007),"Optimization of a Clamped Plate Silencer," *The Journal of the Acoustical Society of America* 121(2), 949-960.

Wang Chunqi, Huang Lixi, (2008), "Analysis of absorption and reflection mechanisms in a three-dimensional plate silencer," *Journal of Sound and Vibration* 313(3-5), 510-524.

Wang Chunqi, Cheng Li and Huang Lixi, (2007) "Realization of a broadband low frequency plate silencer using sandwich plates," *Journal of Sound and Vibration*, in press.

Conference Proceedings:

Wang Chunqi, Cheng Li, Huang Lixi (2007), "Experimental realization of a broadband low frequency plate silencer," *Proceedings, 12th Asia Pacific Vibration Conference*, August 6-9, Hokkaido University, Sapporo, Japan.

Wang Chunqi, Huang Lixi (2006), "Experimental study of duct noise reflection by a side-branch plate supported by a cavity," *Proceedings, Inter-noise 2006*, December 3-6, Honolulu, Hawaii, USA.

ACKNOWLEDGEMENTS

I am deeply grateful to my supervisors, Professor Cheng Li and Dr. Huang Lixi, for their creative ideas and insights that have had such a strong influence on this thesis. I thank them for giving me the opportunity to learn so much at The Hong Kong Polytechnic University, and giving encouragement and support throughout the duration of this project. The project would not be successful without their guidance and enlightenment.

I would like to thank Dr. Choy Yat-Sze, Dr. Peng Shuzhi and Ms. Han Jun for their kind assistance and discussions during the past three years. I would also like to thank all the staff and technicians in the laboratories and offices for their support.

Finally, I wish to express my thanks to my late father who will forever be my inspiration and my mother for her love and support. Special thanks go to my wife, Wang Yanling, for all of her supports, help and understanding during my PhD study.

TABLE OF CONTENTS

Certificate of originality **i**

Abstract **ii**

List of publications already published, accepted or submitted **iv**

Acknowledgements **v**

Table of contents **vi**

List of figures and tables **ix**

Nomenclature **xv**

1 Introduction **1**

1.1 Background 1

1.2 Literature review on duct noise control methods 2

1.2.1 Dissipative noise control 2

1.2.2 Reactive noise control 4

1.2.3 Active noise control 7

1.2.4 Drumlike silencer 8

1.3 Motivations and objectives 11

1.4 Outline 13

2 Theoretical modelling on sound reflection by plates covering side-branch cavities in a flow duct **15**

2.1 Introduction 15

2.2 Sound radiation in hard-walled duct with mean flow 18

2.2.1 Radiation pressure of a point source 18

2.2.2 Distributed source in a rectangular cross-section 21

2.3 Analytical modelling of the plate silencer 22

2.3.1 Coupled dynamics of the sound-plate interaction 22

2.3.2 Radiation and cavity impedances 24
2.3.3 Transmission loss, TL 31
2.3.4 Conservation of acoustic energy 34
2.4 Performance analysis without mean flow effect 35
2.4.1 Transmission loss spectrum 35
2.4.2 Free vibration of a simply supported plate backed by rigid cavity 38
2.5 Effect of mean flow 42
2.6 Summary 46

3 Theoretical study on design parameters 47

3.1 Introduction 47
3.2 Theoretical formulation 49
3.2.1 *In vacuo* mode of the clamped plate 49
3.2.2 Modal dynamics of the sound-plate interaction 51
3.3 Performance analysis 54
3.4 Effect of various design parameters 57
3.4.1 Cavity shape 58
3.4.2 Plate mass 58
3.4.3 Plate bending stiffness 60
3.4.4 Acoustic leakage 63
3.5 Nonuniform plate 65
3.5.1 Method of solution 65
3.5.2 Optimization of $B(x)$ 67
3.6 Summary 75

4 Experimental validation and performance assessment of prototype silencer 77

4.1 Introduction 77
4.2 Experimental rig 78
4.3 Validation experiment 82
4.3.1 Mechanical properties of the balsawood plate 82
4.3.2 Results analysis 84
4.4 Plate silencer using sandwich plate 88

4.4.1 Sandwich construction 88
4.4.2 Experimental results on sandwich plates I, II & III 92
4.4.3 Partial sandwich plate 100
4.5 Summary 102

5 Analyses of sound reflection and absorption mechanisms in a three-dimensional plate silencer 105

5.1 Introduction 105
5.2 Theoretical outline 107
5.2.1 Finite element modelling 107
5.2.2 Model validation 113
5.3 Three-dimensional wave reflector 115
5.3.1 Silencing performance 115
5.3.2 Discussion 124
5.4 Hybrid silencer 129
5.5 Summary 134

6 Conclusions and recommendations 136

6.1 Summary and conclusions 136
6.2 Recommendations for future study 140

Appendix 142

References 154

List of figures and tables

Figure 2.1	Two-dimensional configuration of a side-branch plate silencer.	16
Figure 2.2	Sketch of a duct containing a point source.	18
Figure 2.3	TL comparison of the simply supported plate silencer (solid line) with the expansion chamber of the same cavity geometry of L=5h, h_c=h. The plate has a mass ratio m=1 and optimal bending stiffness B_{opt} =0.129. The TL of the plate silencer is calculated with different numbers of vibration modes N.	36
Figure 2.4	Root-mean-square (rms) level of the plate vibration. The open circles indicate the corresponding TL peaks of the plate silencer.	37
Figure 2.5	Comparison of the first vibration mode of the beam-cavity system and the plate response of the plate silencer at the first TL spectral peak.	40
Figure 2.6	Comparison of the second vibration mode of the beam-cavity system and the plate response of the plate silencer at the second TL spectral peak.	41
Figure 2.7	Comparison of the third vibration mode of the beam-cavity system and the plate response of the plate silencer at the third TL spectral peak.	41
Figure 2.8	Variation of TL spectrum with respect to the Mach number, M, for the simply-supported plate silencer with L =5, h_c =1, m =1 and B=0.129.	43
Figure 2.9	Predicted TL spectra of a plate silencer in a flow duct with different bending stiffness (solid line: B=0.129; dashed line: B=0.14). The Mach number of the mean flow is, M=0.045. The cavity is of L =5 and h_c =1. The mass ratio of the plate is m =1.	45
Figure 3.1	TL comparison of the clamped plate silencer (solid line, with B=0.07) with drumlike silencer (dashed line, with T=0.475) with the same cavity geometry of L=5h, h_c=h, and the same mass ratio of m=1.	56
Figure 3.2	TL comparison of the clamped plate silencer (solid line, with B=0.07) with the simply supported silencer (dashed line, with B=0.129) with the same cavity geometry of L=5h, h_c=h, and the same mass ratio of m=1.	57

Figure 3.3	Variation of the optimal performance of the clamped plate silencer with respect to the mass ratio *m*. (a) Bandwidth f_2 / f_1. (b) Required optimal bending stiffness. The cavity geometry is $L = 5h$ and $h_c = h$.	59
Figure 3.4	Variation of TL spectrum with respect to the plate bending stiffness B. The mass ratio is fixed at $m = 1$, and the cavity geometry is $L = 5$ and $h_c = h$.	61
Figure 3.5	Schematic of the gaps between the plate and the duct walls. The width of the duct is D, and the gaps are τ_1 and τ_2, respectively.	64
Figure 3.6	Variation of TL spectra with respect to the gap width τ.	65
Figure 3.7	Optimization of the non-uniform plate. (a) Optimal distribution of the bending stiffness along the length of the plate. (b) TL. (c) Bandwidth f_2 / f_1 with respect to the relative bending stiffness at the two thin ends. (d) Bandwidth f_2 / f_1 with respect to the length of the thick part of the plate. The cavity geometry is $L = 5h$, $h_c = h$; average mass ratio $\overline{m} = 1$.	69
Figure 3.8	Comparison of the vibration velocity distribution $V(x)$ between the clamped nonuniform plate (solid lines) and the simply supported plate (dashed lines). (a) $f = 0.037$, real parts. (b) $f = 0.2$, real parts. (c) $f = 0.037$, imaginary pars. (d) $f = 0.2$, imaginary parts.	71
Figure 3.9	Comparison of the clamped nonuniform plate (solid lines) with the simply supported uniform plate (dashed lines). The cavity geometry is of $L = 5h$, $h_c = h$, and $\overline{m} = 1$. (1a) TL. (2a) Odd-even modal interference index. (3a) Sound reflected by the even modes. (4a) Sound reflected by the odd modes. The second and third columns compare the modal amplitude, $\lvert V_j \rvert$, the modal reflection coefficient, $\lvert R_j \rvert$, the single mode reflection, $\lvert V_j R_j \rvert$, and the modal contribution γ_j of the two plate silencers. The four peak positions are identified in all the subfigures.	74
Figure 4.1	Schematic of the four-microphone, two-load measurement system. (dimensions in *mm*)	79
Figure 4.2	Photo of a prototype plate silencer using balsawood plates.	79

Figure 4.3	Comparison of the measured data (with open circles) with theoretical predictions (without open circles) for the expansion chamber. (a) TL. (b) The absorption coefficient α. (c) The reflection coefficient β.	81
Figure 4.4	Three-point bending test of the balsawood plate. (a) Schematic of the bending test. (b) Load versus extension at the middle point.	83
Figure 4.5	Comparison of experimental data (with open circles) with theoretical predictions (without open circles). (a) TL, (b) The absorption coefficient α . (c) The reflection coefficient β. The plate properties are measured as: bending stiffness B=0.0123; mass ratio m=3.4.	85
Figure 4.6	Modelling of plate damping mechanisms with two set of damping factors. (1a), (1b), and (1c) show the results with $\sigma_m = 0.15, \sigma_s = 0$. (2a), (2b), and (2c) show the results with $\sigma_m = 0.05, \sigma_s = 0.05$.	87
Figure 4.7	Cross sectional view of the sandwich plate consisting of two thin skin sheets each of thickness, h_t, and a thick core of thickness , h_0.	89
Figure 4.8	Optimal design of the sandwich construction with given core material (Rohacell IG-31) and skin sheet (aluminium). (a) Variation of E/ρ_s^3 with respect to the ratio of h_t / h_0. (b) Comparison between the achievable maximum bending stiffness, B_1 , and the required optimal bending stiffness B_{opt}. The curve for B_2 shows the situation where 50% loss of bending stiffness occurs during the sandwich construction.	90
Figure 4.9	Schematic for the perforated foam core used in the sandwich construction. Perforation diameter: 5 mm.	91
Figure 4.10	Measured data for plate silencer I. (a) TL. The predicted TL for an expansion chamber of the same cavity geometry is also given in dashed line for comparison. (b) Absorption coefficient. (c) Reflection coefficient.	94
Figure 4.11	Comparison of experimental data (solid curves with open circles) with theoretical predictions (solid curves: without structural damping; dashed curves: with structural damping: σ_m =0.15 and σ_s =0.05.) for plate silencer I. (a) TL. (b) Absorption coefficient. (c) Reflection coefficient.	96

Figure 4.12 TL comparison among three plate silencers with different plate properties (I: m=2.4, B=0.061; II: m=2.75, B=0.061; III: m=2.4, B=0.037). (a) Experimental results. (b) Predictions with the structural damping of the plate modelled as σ_m =0.15 and σ_s =0.05. 99

Figure 4.13 Cross section of the partial sandwich plate (dimensions in mm). 101

Figure 4.14 Experimental data for the partial sandwich plate. (a) TL. (b) Absorption coefficient. (c) Reflection coefficient. 102

Figure 5.1 The quarter model of a four-cavity wave reflector (or hybrid silencer). The bottom and top (not shown) cavities have a length of L and depth h_{c1}; the back and front (not shown) cavities have a length of L and depth h_{c2}. In the case of a hybrid silencer, the bottom and top cavities are used to reflect sound and the other two cavities are filled with sound absorption materials. Otherwise, all of the four cavities are for sound reflection. 108

Figure 5.2 Comparison between the FEM simulations (open circles) and the analytical solutions (solid lines). (a) TL spectra of a two-cavity wave reflector. The cavities have a length of L = 5 and depth h_c = 1. The plates with stiffness B=0.129 and mass ratio m=1 are simply-supported at the leading and trailing edges. (b) TL spectra of duct lining filling (flow resistance R_{sam}=1.4) two cavities of depth h_c =1 and length L = 5. 114

Figure 5.3 Cross sections for the three-dimensional wave reflectors. (a) Four-cavity wave reflector. Four backing cavities with depth h_c are shown in shadowed area. Four plates forming part of the otherwise rigid duct walls are shown in thick solid lines. (b) Rectangular duct with circular chamber of radius R. (c) Regular octagon duct with circular chamber of radius R. The side length of the octagon a satisfies the relationship: $2(1+\sqrt{2})a^2 = h^2$. (d) Rectangular duct with rectangular chamber. The side lengths for the outer and inner square cross sections are H and h, respectively. 116

Figure 5.4 TL comparison between the 3D plate silencer I (four-cavity, B_{opt} =0.215) and the 2D design (2-cavity, B_{opt} =0.129). The two configurations have the same cavity volume Λ =10, cavity length L=5, and mass ratio m=1. 119

Figure 5.5 Figure 5.5: Normalized error $|\alpha|$ for the 3D plate silencer I. 120

Figure 5.6 Geometry and structured mesh for the circular chamber (quarter model). 121

Figure 5.7 TL comparison between the 3D plate silencer II (rectangular duct with circular chamber, B_{opt} =0.212) and the 2D design (2-cavity, B_{opt} =0.129). The two configurations have the same cavity volume Λ =10, cavity length L=5, and mass ratio m=1. 122

Figure 5.8 TL comparison between the 3D plate silencer III (regular octagon duct with circular chamber, B_{opt} =0.188) and the 2D design (2-cavity, B_{opt} =0.129). The two configurations have the same cavity volume Λ =10, cavity length L=5, and mass ratio m =1. 123

Figure 5.9 TL comparison between the three-dimensional plate silencer II (rectangular duct with rectangular chamber, B_{opt} =0.215) and the two-dimensional design (2-cavity, B_{opt} =0.129). The two configurations have the same cavity volume Λ =10, cavity length L=5, and mass ratio m=1. 124

Figure 5.10 Three dimensional effect of the four-cavity wave reflector. (a) Contour of the velocity potential inside the duct at the cross section of x=0 for f=0.05. (b) Velocity response of the plate at frequency f=0.05. 126

Figure 5.11 Comparison of the optimal performance for the circular wave reflector (3D plate silencer III) with the 2D design of the same total cavity volume Λ =10. (a) TL spectra. (b) Contribution by the odd axial modes towards the total sound wave reflection. (c) Contribution by the even axial modes towards the total sound wave reflection. (d) Odd-even interference index. The positions of the three spectral peaks are marked by vertical dotted lines. 128

Figure 5.12 Optimal performance of the hybrid silencer. (a) TL. (b) Absorption coefficient, α . (c) Reflection coefficient, β . The optimal bending stiffness B_{opt} =0.0627 and optimal flow resistance $R_{sam,opt}$ =1.4 are obtained with the following parameters given: L =5, h_c =1, m=1. 131

Figure 5.13 TL comparison between the four-cavity hybrid silencer (L=5, B_{opt} =0.0627, $R_{sam,opt}$ =1.4) and a four-cavity absorptive chamber (L=5, 10, $R_{sam,opt}$ =1.4). The cavity depth is h_c=1 for the two designs. 133

Figure 5.14	TL comparison between a hybrid silencer and a four-cavity wave reflector of the same total cavity volume $\Lambda = 20$.	134
Table 2.1	Natural frequencies of the beam in vacuum, the rigid cavity and the beam-cavity coupling system.	39
Table 3.1	Dimensionless bending stiffness for plates made of different materials.	63
Table 4.1	Properties of the sandwich plates.	92

Nomenclature

Symbol	Description
A	Area of the cross section of a duct
b	Breadth of the rectangular duct
B	Bending stiffness, normalized
B_{opt}	Optimal bending stiffness, normalized
c_0^*	Speed of sound in free space (m/s)
c_0	Normalized speed of sound in free space
c_c	Complex speed of sound in the porous media, normalized
c_r	Phase speed of the rth duct mode, normalized
c_{rs}	Phase speed of the (r, s) cavity mode, normalized
E^*	Young's modulus (Pa)
E	Normalized Young's modulus
f	Normalized frequency
f_1	Lower frequency limit of the stopband
f_2	Upper frequency limit of the stopband
H	Heavside function
h^*	Duct height (m)
h	Normalized duct height
h_c	Normalized cavity depth
h_t	Thickness of the skin sheet of the sandwich plate, normalized
h_0	Core thickness of the sandwich plate, normalized
i	Imaginary unit
j	Subscript denoting the vibration mode, vibration mode

k_0^*	Total wavenumber, defined as, $k_0^* = \omega^* / c_0^*$
k_0	Normalized total wavenumber
k_r	Modal wavenumber, defined as $k_r = \omega / c_r$
k_{rs}	Modal wavenumber, defined as $k_{rs} = \omega / c_{rs}$
L^*	Length of the plate (m)
L	Length of the plate, normalized
l	Subscript denoting the vibration mode, vibration mode
L_j	The jth mode property constant of the plate
L_{opt}	Optimal plate length, normalized
M	Mach number
m^*	Surface density of the plate (kg/m^2)
m	Plate-to-air mass ratio, mass ratio
$\overline{m}$	Average mass ratio of the nonuniform plate
$\vec{n}$	Normal direction of the surface
p	Normalized sound pressure
p_0	Normalized ambient pressure
p_i^*	Incident sound wave (Pa)
p_i	Normalized incident sound wave
p_r	Normalized reflected sound wave
p_t	Normalized transmitted sound wave
p_+	Fluid loading (sound pressure) on the upper surface, normalized
p_-	Fluid loading (sound pressure) on the lower surface, normalized
p_{+rad}	Radiation pressure in the duct, normalized
$p_{+rad,j}$	Radiation pressure in the duct induced by the jth modal vibration of unit amplitude, normalized

p_{cav}	Acoustic pressure inside the cavity, normalized
$p_{cav,j}$	Acoustic pressure inside the cavity induced by the jth modal vibration of unit amplitude, normalized
Q_0	Volume velocity amplitude, normalized
R	Radius of a circular chamber, normalized
R_{sam}	Flow resisitivity
$R_{sam,opt}$	Optimal flow resisitivity
R_j	Complex amplitude of the reflected sound by the jth modal vibration of unit amplitude
Re	Real part of a complex number
r,s	Subscripts denoting the acoustic mode, acoustic mode
TL	Transmission loss
TL_{cr}	Criterion level of the transmission loss
t^*	Time (s)
t	Time, normalized
U^*	Flow velocity (m/s)
u	Particle velocity, normalized
V	Normal velocity of the plate, normalized
V_j	Vibration amplitude of the jth *in vacuo* mode
V_{rms}	Root-mean-square level of the plate velocity response
W_{in}	Incident acoustic energy flux
W_r	Reflected acoustic energy flux
W_t	Transmitted acoustic energy flux
x^*, y^*, z^*	Cartesian coordinates, dimensional
x, y, z	Cartesian coordinates, normalized

x', y'	Cartesian coordinates for the sound source, dimensionless
Z_{jl}	Modal radiation impedance on the jth vibration induced by the lth vibration mode
Z_{+jl}	Component of Z_{jl} due to p_{+rad}
Z_{cjl}	Component of Z_{jl} due to p_{cav}
α	Coefficient of sound power dissipated or absorbed
β	Reflection coefficient of sound energy flux
β_j	Weighted natural frequency of a beam
γ_j	Modal reflection contributed by the jth vibration mode towards the total sound reflection
$\delta(\,)$	Dirac delta function
δ_{ij}	Kronecker delta function
ζ_{rs}	Damping ratio of the (r,s) cavity mode
η^*	Displacement of the plate
η	Normalized displacement of the plate
θ	Phase angle between the reflected wave from the odd modes and that from the even modes.
I_j	Modal coefficient of the incident wave
$\mathrm{K}_{rs}^{\pm}$	Modal wavenumber in mean flow (+: downstream; −: upstream)
κ_{rs}	Characteristic wavenumber
Λ	Total cavity volume
ξ	Local dimensionless variable defined as $\xi = x/L + 1/2$
ξ'	Dimensionless source coordinate defined as $\xi' = x'/L + 1/2$
ρ_0^*	Air density (kg/m^3)

ρ_0	Normalized air density
ρ_s^*	Density of engineering materials (kg/m^3)
ρ_c	Equivalent complex density of the porous media
ρ_s	Normalized density of engineering materials
σ_m	Mass damping coefficient in the Rayleigh damping model
σ_s	Stiffness damping coefficient in the Rayleigh damping model
τ	Gap width between the plate and the duct wall
υ	Poisson's ratio
ϕ	Velocity potential
φ_j	The jth *in vacuo* vibration mode of the plate (beam)
ψ_r	The rth duct acoustic mode
ψ_{rs}	The (r, s) cavity acoustic mode
ω^*	Angular frequency (rad/s)
ω	Normalized angular frequency

CHAPTER 1

INTRODUCTION

1.1 Background

Duct acoustics is an area of continuous interest for its theoretical and practical importance. A typical example is the excessive noise associated with the Heating Ventilation and Air Conditioning (HVAC) system, which travels along the ductwork and finally enters the working or living area. The major source of noise in a duct system is the fan. Apart from mechanical noise, such as that caused by bearings, motors, belts, etc., fans produce two major types of aerodynamic noise, i.e., rotation noise and turbulent flow noise (Sharland, 1964; Longhouse, 1976; Woods, 1976). Rotational noise arises from the interaction between the blades and the surrounding air. The steady rotation of fan blades gives a periodically varying pattern of high and low static pressures when observed by a stationary listener. Turbulent flow noise is caused by turbulent flow. It has a random frequency distribution, and as such no individual tones can be detected in the component of the fan noise. Each of the two types tends to produce a broadband sound spectrum. A better structural design can help to reduce the fan noise, however, it is impossible to eliminate it. In addition to fan noise, regenerated noise and breakout noise may also pose a problem in the ductwork system. Regenerated noise refers to the noise resulting from the flow of air through the ductwork system. For instance, when a rectangular duct changes size or direction, airflow noise is created due to turbulence. Breakout noise refers to the

noise emission outside the ductwork. This problem is rather common but unfortunately hard to cure.

When noise reduction cannot be achieved at the source, it may be useful to modify the noise propagation path. Toward this purpose, various noise control methods have been developed. According to whether there is a powered system involved, these methods can be classified into two main types: active and passive noise control methods. In general, high frequency noise can be easily tamed via the use of sound absorbing materials. However, the low frequency noise is difficult to control and remains a technical challenge, especially through passive methods.

1.2 Literature review on duct noise control methods

1.2.1 Dissipative noise control

The passive noise control can be further categorized as dissipative and reactive methods, depending on whether the acoustic energy is dissipated or reflected back. A dissipative noise control device usually involves the use of sound absorbing materials such as mineral wool, foams or fibreglass. Due to the friction between the oscillating air and the fibres of porous material, together with the viscous damping within the air itself, acoustic energy can be converted to heat and then dissipated. This is the main mechanism associated with the dissipative noise control. Other energy loss mechanisms include the isothermal compression of air at low frequencies, direct conversion of acoustical energy into heat owing to a time lag between compression, and heat flow that takes place in closed cell foams (Mechel and Ver, 1992). Porous media have been the backbone of almost all dissipative noise abatement techniques.

Lining a duct with porous sound absorbing materials is a very mature and reliable technique which can tackle the medium-to-high frequency noise (Mechel and Ver, 1992; Ingard, 1994). The theory of sound attenuation in a lined duct has also been well developed (Morse and Ingard, 1968; Allard, 1993; Ingard, 1994). Basically, the duct liner can be categorized as locally reacting and non-locally reacting. A locally reacting liner model applies when various parts of the porous surface are not strongly coupled together, and the normal motion of one portion of the surface is dependent only on the acoustic pressure incident on that portion and independent of the motion of any other part of the area. Otherwise, non-locally reacting liner model should be used. To predict the noise abatement, propagation constant and characteristic impedance of the sound absorbing materials should be determined. In doing so, empirical formulas based on experimental results can be employed (Delany and Bazley, 1970; Bies and Hansen, 1980; Attenborough, 1983; Utsuno et al., 1989). A well-designed dissipative silencer can provide definite attenuation of sound over a wide range of frequencies.

There are, however, two major concerns on the application of porous sound absorbing materials. Acoustically, existing sound absorption techniques such as duct lining, are usually ineffective in the low frequency range. Take a square duct of cross section $100\,mm \times 100\,mm$ for example. According to Huang (2004), duct linings can achieve satisfactory performance down to the frequency of 260 Hz, however, it does not work well if the frequency goes down further. Generally speaking, the conversion of acoustical energy into heat is effective primarily for high frequencies with short wavelengths. If the thickness of a porous absorber is less than one quarter of the acoustic wavelength, the absorber usually has little effect. This requires a sufficient

thickness. In fact, one challenge in sound absorber design is to keep the absorber thickness to a minimum (Mechel and Ver, 1992). From the environmental point of view, there has been increasing concern about the deposition and accumulation of dusts in the pores of the porous material. A periodical cleaning will obviously increase the maintenance cost of building ventilation systems using porous linings. There are also places, such as operation theatres and clean rooms, where high hygienic requirement forbids the use of such materials. In fact, there are already public concerns of bacteria breeding in the ventilation systems of ordinary commercial buildings and homes equipped with HVAC systems (Batterman and Birge, 1995; Pastuszka, 2000; HKEPD, 2003). Hence, an alternative method, which is both “clean” and effective in the low frequency, is desirable.

1.2.2 Reactive noise control

Sound waves propagating along a duct can also be attenuated using reactive mufflers. A reactive muffler consists of a number of tubular elements of different transverse dimensions joined together so as to cause, at every junction, impedance mismatch and hence reflection of a substantial part of the incident acoustic energy back to the source (Munjal, 1987). These reactive devices include, but are not limited to, expansion chambers, Helmholtz resonators, and Herschel Quincke tubes.

Expansion chambers reflect sound waves by introducing a sudden change in cross sectional area in the duct. They have broadband frequency characteristics, though the attenuation is not high. In contrast to the duct liner using porous sound absorbing materials, a well designed expansion chamber type muffler (for example, the vehicle exhaust muffler) can treat the low frequency noise effectively. However, the most important detrimental effect in a vehicle muffler is the back pressure

(pressure loss) due to the discontinuity of the duct cross section. The back pressure results in extra power consumption. As a result, more noise could be generated by the additional power required to overcome the pressure loss. To reduce the back pressure, straight-through concentric resonator, plug muffler, and three-duct cross-flow muffler have been proposed and their performance has been experimentally verified (Munjal, et.al., 1993; Zha et al., 2002). The existence of passband is another problem associated with the expansion chamber. The passband may be eliminated either by the connection of multiple chambers via internal connecting tubes of suitable lengths (Davis et al., 1954) or by using multiple chambers of different dimensions (Ingard and Pridmore-Brown, 1951). But such a device is usually rather bulky.

Helmholtz resonators are also widely used in ducts, pipes, as well as many other applications (for instance, Munjal, 1987; Fry, 1988). In a Helmholtz resonator, the air in the chamber acts as a spring, while the air in the neck works as a mass attached to the spring. The mass-spring system has a resonance frequency at which oscillation becomes self-sustained. Zero acoustic pressure at the mouth of the resonator is maintained, which means a complete reflection of grazing incident waves in the duct. As an effective noise control method, a lot of efforts have been made on how to predict and improve the performance of such a resonator in the past few decades. For example, Ingard (1953) discussed the absorption and scattering from resonators in a free field and in an infinite wall. Anderson (1977) studied the effect of flow when a single side-branch Helmholtz resonator is attached to a circular duct. Helmholtz resonators with different geometries and complicated arrangements have also been proposed and investigated (Chanaud, 1994; Mechel, 1994; Selamet and Lee, 2003; Tang, 2005; Li and Vipperman, 2004; Li and Cheng, 2007).

The main advantage of the Helmholtz resonator lies in its strong sound attenuation property once properly tuned to the target frequency (Harris, 1991). However, for slightly different frequencies, its performance deteriorates sharply which leads to a very narrow TL spectrum unless a resonator array comprising multiple resonators is used (Seo and Kim, 2005; Li, et al., 2007). Moreover, when using Helmholtz resonator to control relatively low frequency noise, the cavity volume or the neck length must be very large due to the extremely high cavity stiffness, which also limits its application in the situation where the installation space is restricted. It is possible to use some adaptive techniques to tune automatically the resonator parameters to control tonal noise with varying frequencies (Bedout, et al., 1997; Nagaya, et al., 2001). Active side-branch resonators are applied to control duct noise by many researchers (Taki, et al., 1991; Okamoto, et al., 1994; Utsumi, 2001; Radcliffe and Birdsong, 2002). But obviously it would be much better if the bandwidth of the resonator can be extended with a purely passive set-up. Efforts are also made to achieve a passive broadband silencer based on the principle of Helmholtz resonator. A typical example is the microperforated panels (Maa, 1975, 1998; Fuchs and Zha, 1997; Kang and Fuchs, 1999), which can be considered as an array of Helmholtz resonators. However, its low frequency performance is still hampered by the cavity stiffness.

The Herschel-Quincke (HQ) tube is another commonly-used acoustic attenuation device for duct systems. An HQ tube is essentially a hollow side-tube that travels along a main duct axis and attaches to the main duct at each of the two ends of the tube (Stewart 1928). The incident sound wave divides at the first intersection and later recombines at the second intersection of the side-tube and the main-duct. Due to

the difference of wave propagation path, resonance occurs at a number of discrete frequencies when the acoustic volumetric flow from the side tube cancels that of the wave along the main duct. For the case when the side tube has twice the length of the main duct with the same dimension, the transmission loss is about 8 dB over one octave band. Like the Helmholtz resonator, the attenuation band of the HQ tube is usually narrow (Davis et al., 1954).

1.2.3 Active noise control

Active noise control (ANC) is becoming one popular technique in dealing with low frequency noise, especially, in laboratory studies. The basic idea of ANC can be explained with a simple application associated with attenuation of plane waves propagating in ducts (Pelton, 1993). The ANC system uses a sensor to detect noise as it propagates down a duct. This signal is fed into a digital controller that analyses the frequency content, then produces a control signal to drive a set of secondary or control noise sources (actuators). Usually, the secondary sources will produce a sound field that is out of phase with the original field and noise cancellation occurs due to destructive interference. The number of secondary sources and sensors required is determined by the complexity of the original sound field and the magnitude of cancellation needed. ANC technique has been applied to one-dimensional field and duct noise, enclosed spaces and interior noise, noise in some three-dimensional spaces, and in personal hearing protection (Nelson and Elliott, 1993).

Despite the effectiveness of ANC in many laboratory studies, the number and scope of long term commercial applications are relatively small (Hansen, 1997). A number of technical problems prohibit widespread implementation of the new

technology. The most limiting problem may be the availability of proper sensors and actuators. It is often a challenge to find stable sensors/actuators capable for continuous operation for long periods of time in harsh industrial environments (Hansen and Snyder, 1997). Besides, complexity, cost and maintenance are also important factors that should be considered when designing ANC systems. For example, an active muffler was designed for motor cars (Kim et al., 1998). Although the performance of the proposed ANC muffler is attractive but the system requires many microphones and the cost is quite considerable. Current industrial applications of ANC technology are limited mainly to the control of plane wave sound propagation in air handling ducts, gas turbine exhausts or diesel engine exhausts (Hansen, 2005). Limited by the existing commercially available hardware and software, the most successful industrial applications of ANC usually target single or multiple tonal noise, although applications also exists that produce significant noise reduction over 1/2 to 2 octave frequency range.

1.2.4 Drumlike silencer

The development of the drumlike silencer may be traced back to a previous study by Huang (1999), in which noise reduction by flush-mounted membranes in an otherwise rigid duct was studied theoretically. When waves travel in a passage with considerable cross section distensibility, fluid compressibility gives way to wall compliance as the main mechanism controlling the wave speed (Lighthill, 1978). The sound waves coupled with the flexural waves of a membrane tend to travel much more slowly than the isentropic speed of sound in air, as verified in an experiment carried out later (Huang, et al., 2000). The sudden change of wave speed leads to substantial wave reflection and scattering at the edges where the compliant passage

joins the rigid duct with equal cross section. For the membrane-duct device in Huang (1999), the effect of air outside the duct was excluded. To explore the use of the above concept in a real silencer, a cavity has to be added to prevent the noise break-out, hence, the drumlike silencer (Huang, 2002). A typical drumlike silencer consists of an expansion chamber with two side-branch cavities covered by light membranes under a fairly high tension. Theoretical study shows that the drumlike silencer works effectively over a broad band in the low frequency range when a certain high tension is applied on the membrane in the axial direction of the duct (Huang, 2002). The prototype device has also been tested successfully without (Choy and Huang, 2002) and with flow (Choy and Huang, 2005). Besides the team led by Huang, other researchers also showed their interest in duct noise control by panel reflection. Following the idea proposed in Huang (1999), Choi and Kim (2002) studied the frequency characteristics and sound reduction performance of the duct-membrane device theoretically. Ramamoorthy and Grosh (2002, 2003) proposed a similar idea of drumlike silencer as an analogy to the function of cochlea. Lawrie and Guled (2006) tried to tune the silencer by varying the position of the tensioned membrane that is otherwise flushed-mounted with the duct wall in the drumlike silencer.

Besides the broad stopband in the low frequency region, the drumlike silencer carries several extra potential merits compared with other traditional methods. First, the drumlike silencer provides a fiber-free solution to the duct noise problem, so that it is more environmental-friendly than the porous duct lining. Second, because the membranes are flush-mounted with the duct and there is no sudden change of duct cross section area, the flow can pass the silencer smoothly without causing any noticeable pressure loss when compared with a uniform duct of the same total length.

Third, since there is no flow separation as in an expansion chamber, the extra noise associated with the turbulent flow due to the flow separation is also avoided. Another benefit of the drumlike silencer is that the use of membrane completely separates the duct from the gas flow in the duct, as shown by Huang and Choy (2005), which eliminates the chance of dust accumulation and other possible long-term environmental and maintenance problems. The complete separation of flow in the duct from the cavity also allows the use of a low impedance gas, such as helium, to fill the cavity to further enhance the silencer performance (Choy and Huang, 2003).

Note that plates and membranes have also been used in many other noise abatement applications. For example, panel absorbers have been used in broadcasting studios and other architectural practices (Brown, 1964; Ford and McCormick, 1969; Sakagami *et al*., 1996; Horoshenkov and Sakagami, 2001). A membrane absorber called 'membrane absorber box' has also been successfully used as a splitter silencer in the exhaust stacks of paper mills (Ackermann, et al., 1988, 1989; Fuchs 1993). It is made by a host of combined Helmholtz and panel resonators in a honeycomb structure. A typical resonator unit consists of a rectangular cavity covered by a perforated membrane. It has been shown that the behaviour of the absorbing element in the membrane absorber box is mainly determined by a combination of Helmholtz resonance and plate resonance (Frommhold, et al., 1994). Moreover, double leaf structure (Kiyama, et al., 1998), perforated panel (Lee and Swenson, 1992) and stiff light composite panels (Tang, et al., 2003) find applications in noise abatement as well. However, in all these applications, the panel, or membrane, is a component of the resonator which works for a narrow frequency band, and the structural mass is a means to achieve a low resonance frequency. For the drumlike silencer, the most

desirable properties of the membrane are the high stiffness and low density, which contrasts with the characteristic of the existing use of panels. The main difference between the drumlike silencer and the previous use of membrane or panel in resonators is that the former aims for a broadband performance with one set of membrane.

1.3 Motivations and objectives

Previous literature review shows that the low frequency duct noise is difficult to deal with, especially through passive methods. Lining a duct with porous sound absorbing material is a mature and reliable technique that can tackle the medium to high frequency noise. However, it does not work well for very low frequencies. Both resonator and expansion-chamber-type mufflers can be used to reduce the low frequency, but the former usually targets for specific frequency while the latter is usually bulky and pressure loss exists. Aiming for a broadband low frequency noise control device, the concept of a drumlike silencer is developed recently. A typical drumlike silencer consists of an expansion chamber with two side-branch cavities covered by light membranes under a fairly high tension. It has been shown that the durmlike silencer achieves its best silencing performance under an optimal tensile force (Huang, 2004). When the membrane is too loose, reflection waves from different parts of the membrane simply cancel themselves out. When the membrane is too tight, it approaches the condition of a hard wall. In practice, however, it is usually difficult to tune or to maintain the tension at the optimal value, since the tension may vary due to membrane relaxation or the change of ambient temperature. Hence, although good silencing performance has been predicted and experimentally

verified for the drumlike silencer, it seems impractical to directly implement such a device in industrial applications.

The difficulty associated with the installation and maintenance of the tensioned membrane calls for a new device that exhibits similar or better performance than the drumlike silencers at low frequencies without using tensioned membranes. To this end, it is proposed to replace the membrane used in the drumlike silencer by a plate, hence a plate silencer. As the plate uses its natural bending moment as the sole structural restoring force, both the installation and the maintenance of the plate silencer are simplified.

The overall objective of this study is to develop a broadband plate silencer that can reduce the low frequency duct noise effectively. In doing so, the following three specific objectives are aimed. First, a theoretical model will be developed to analyze the performance of the plate silencer in a flow duct. Previous analytical work on membrane (or simply supported plate)-acoustics coupling dynamics (Huang, 2002; 2006) is extended to clamped plates which allow easier installation in practice. Moreover, the effect of the mean flow inside the duct, which is excluded in previous studies, is included in the present model. Second, a thorough theoretical study on effects of various design parameters is carried out as a necessary step towards a practical silencer design. Analyses allow the exploration of the working mechanisms and the performance optimization of the silencers. The third objective of this study is the experimental verification of the theory, together with the realization of prototype silencers.

1.4 Outline

The thesis is organized in six chapters. Chapter 1 introduces the background of the present work. At the same time, related previous work is reviewed. Motivations and objectives of this study are presented.

In Chapter 2, a two-dimensional analytical model is established for a typical plate silencer which consists of an expansion chamber with two side-branch cavities covered by light but stiff plates. To simplify the formulation, the simply supported plate model is considered in this chapter. Formula for sound radiation pressure in duct with mean flow is first developed; then the analytical model of the sound-plate interaction in flow duct is established. With the theoretical model established, the performance of the plate silencer is investigated without and with mean flow. Free vibration of the plate-cavity system is also analyzed.

In Chapter 3, the theoretical study previously developed is extended to the boundary condition of clamped plate, which is easier to implement in practice. During the course of this study, it is found that for a clamped plate with constant bending stiffness and mass distribution lengthwise, the stopband of the silencer becomes narrower than that of a simply supported one. Hence, efforts are made to optimize the performance of the clamped plate silencer by adopting nonuniform plates with softer ends. Mechanisms for the performance improvement are also investigated.

The theoretical model is tested experimentally using balsawood in Chapter 4. The spectral peaks and shapes of the measured transmission loss are compared with those calculated theoretically. Attempts are also made to account for the considerable

sound absorption in the test rig. According to the theoretical study, a good design of the plate silencer requires light but extremely stiff plates. Such a requirement for the plate properties is out of the reach of existing homogeneous materials, hence, the feasibility of using sandwich construction is explored, and a broadband low frequency plate silencer is experimentally realized using sandwich plate. Sandwich plates with different mechanical properties are also tested and compared, which partially confirms the theoretical findings about the effect of plate properties on the silencer performance. Issues related to simplification of the sandwich plate modelling are also addressed.

In Chapter 5, the acoustic benefit of using three-dimensional configurations in a plate silencer design is investigated through finite element simulations. The finite element simulation scheme is made out of a software package specializing in solving partial differential equations and multiphysics applications. The code is validated by known analytical solutions. Simulation shows that the three-dimensional design expands the bandwidth in both lower and higher frequency regions relative to the corresponding two-dimensional design. Vibroacoustic analysis on the plate shows that the benefit of three-dimensional design derives from better plate vibration response from axial modes of higher orders. Hybrid arrangement, which combines plate silencer and traditional dissipative chambers in parallel manner, is also studied for a silencer effective from low to high frequency range.

Chapter 6 summarizes the conclusions drawn from the present work.

CHAPTER 2

THEORETICAL MODELLING ON SOUND EFLECTION BY PLATES COVERING SIDE-BRANCH CAVITIES IN A FLOW DUCT

2.1 Introduction

When a segment of rigid duct is replaced by a plate backed by a hard-walled cavity, grazing incident sound waves induce plate vibration, hence sound reflection. Based on this mechanism, a broadband sound wave reflector which works effectively from low-to-medium frequencies can be developed. Because the vibrating plate is the sole element that reflects the incident sound wave, such a device is called a plate silencer in this study. A typical plate silencer consists of an expansion chamber with two side-branch cavities by light but stiff plates. The leading and trailing edges of the plate can be either simply supported or fixed, but only the simply supported boundary condition is considered in this chapter to keep the modelling procedure as succinct as possible. The other two lateral edges of the plate are set free so that the plate can respond to the incident sound waves with high vibration magnitude. Such a configuration is two-dimensional in nature and can be modelled in a two-dimensional manner theoretically.

Figure 2.1 shows the two-dimensional configuration of a side-branch plate silencer. It has a two-dimensional duct (channel) of height h^*, with two plates (beams) flush-mounted on the duct walls. The fluid inside the duct (air) flows and it

is assumed to be uniform and inviscid. The mean flow has a density of ρ_0^*, velocity U^* and Mach number $M=U^*/c_0^*$ where c_0^* is the speed of sound in air. The two plates are simply supported to the rigid duct walls at $|x^*| = L^*/2$, and each plate is backed by a hard-walled cavity of depth h_c^*. A plane incident sound wave comes from the left-hand side of the duct with unit amplitude,

$$p_i^* = \exp[i(\omega^* t^* - k_0^* x^*/(1+M))], \tag{2.1}$$

and it causes the plate to vibrate with a transverse displacement of complex amplitude $\eta^*(x)$ with the same time dependence, $\exp(i\omega^* t^*)$, which is henceforth omitted. The vibration radiates sound towards both ends of the duct. The upstream radiation forms the wave reflection while the downstream radiation combines with the incident wave and destructive acoustic interference then takes place. As the sound field due to the plate vibration also imposes fluid loadings on both sides of the vibrating plate, the problems of acoustics and the plate dynamics are fully coupled to each other.

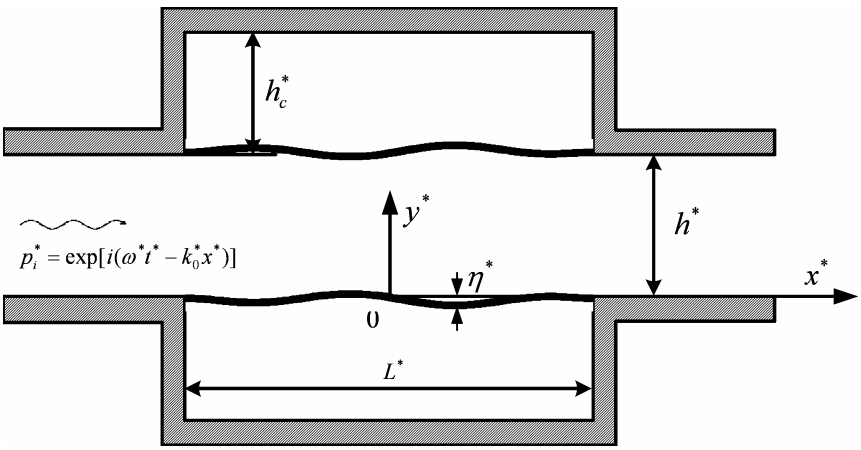

Figure 2.1: Two-dimensional configuration of a side-branch plate silencer.

The main purpose of this chapter is to establish the theoretical framework on the performance analysis of the plate silencer in a flow duct. In doing so, the coupled dynamics problem between the plate vibration and acoustic radiation is solved first. In the current study, a procedure similar to Huang (2002) is followed, with two major modifications being made. First, the mean flow effect is included in the theoretical modelling. Because the flow affects the sound radiation on the panel facing the duct, expressions for the sound radiation pressure in the flow duct need to be established. Second, the fluid loading inside the cavity is characterized via the cavity modes instead of the duct modes, which simplifies the analytical formulation especially in the case when clamped plates are used (see Chapter 3). With the method of solution established, the performance of the proposed silencer is investigated theoretically.

For convenience, all variables are normalized by three basic quantities in the following presentation, that is, air density ρ_0^* , duct height h^*, and speed of sound in free space c_0^*, for instance:

$$x = \frac{x^*}{h^*},\ \ y = \frac{y^*}{h^*},\ t = \frac{c_0^* t^*}{h^*},\ \ L = \frac{L^*}{h^*},\ \eta = \frac{\eta^*}{h^*},\ k_0 = \frac{\omega^* h^*}{c_0^*},$$

$$k_r = -i\sqrt{(r\pi)^2 - k_0^2},\ m = \frac{m^*}{\rho_0^* h^*}\quad \omega = 2\pi \frac{f^*}{c_0^*/h^*} = 2\pi f = k_0,$$

$$\xi = \left(\frac{x}{L}\right) + \frac{1}{2},\quad p = \frac{p^*}{\rho_0^*(c_0^*)^2},\quad B = \frac{B^*}{(h^*)^3 \rho^*(c_0^*)^2}. \tag{2.2}$$

Whenever a dimensional variable is used, a physical unit is given. Otherwise, all variables are considered as dimensionless based on the above normalization scheme. For example, m is the plate-to-air mass ratio, or mass ratio, and B is the dimensionless bending stiffness of the plate.

2.2 Sound radiation in hard-walled duct with mean flow

2.2.1 Radiation pressure of a point source

Theoretical formulation for radiation pressure of a source in a hard-walled duct with non-reflecting terminations and no mean flow has been well-established by Doak (1973). Here, Doak's formulation is extended to the situation where uniform mean flow exists in the duct. As the basis of developing formula for general pressure radiation in hard-walled duct with mean flow, the simplest case of a point source is first investigated.

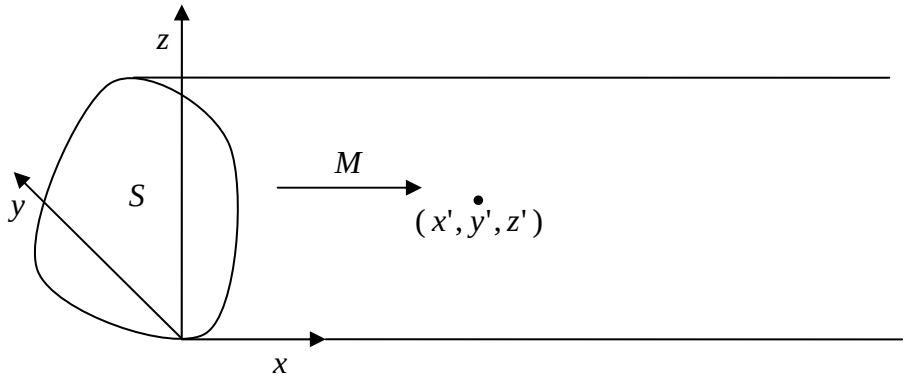

Figure 2.2: Sketch of a duct containing a point source.

Consider a hard-walled duct with cross section S as illustrated in Figure 2.2. Let x denote the Cartesian coordinate along the duct axis and y, z denote the cross section coordinates. The fluid inside the duct is assumed to be inviscid and flows uniformly in the x direction. The mean flow has a density of ρ_0, and Mach number, M. The acoustic perturbation pressure is p (the total pressure being $p+p_0$ where p_0 is the ambient pressure).

A point acoustic source, of simple harmonic time dependence and of volume velocity amplitude Q_0 (complex value, in general), is placed at the point (x', y', z') in the duct. Then the acoustic velocity potential ϕ satisfies the propagation equation,

$$\left(1-M^2\right)\frac{\partial^2\phi}{\partial x^2}+\frac{\partial^2\phi}{\partial x^2}+\frac{\partial^2\phi}{\partial z^2}-\frac{2M}{c_0}\frac{\partial^2\phi}{\partial t\partial x}-\frac{1}{c_0^2}\frac{\partial^2\phi}{\partial t^2}=Q_0e^{i\omega t}\delta(x-x')\delta(y-y')\delta(z-z'), \quad (2.3)$$

where $\delta()$ is the Dirac delta function. The velocity potential ϕ is related to the acoustic pressure p and the acoustic particle velocity u as

$$p=-\rho_0\left(\frac{\partial}{\partial t}+Mc_0\frac{\partial}{\partial x}\right)\phi, \quad (2.4)$$

$$u=\frac{\partial\phi}{\partial x}. \quad (2.5)$$

At the rigid duct walls, the normal component of particle velocity must vanish, thus, the boundary condition on the pressure at the duct wall is

$$\frac{\partial p}{\partial\vec{n}}=0, \quad (2.6)$$

where $\vec{n}$ is (outward) normal to the wall. The velocity potential ϕ fulfils a Sommerfeld condition.

Making use of the separation of variables and assuming a time dependence function $e^{i\omega t}$, the solution to wave Eq. (2.3) may be assumed to be of the form,

$$\phi=\sum_{r,s}J_{rs}(x)\psi_{rs}(y,z)e^{i\omega t}. \quad (2.7)$$

The $\psi_{rs}(y,z)$ is the normalized characteristic functions of the two-dimensional space defined by the duct cross-section, which satisfy the boundary condition:

$$\frac{\partial}{\partial\vec{n}}\psi_{rs}(y,z)=0, \quad (2.8)$$

at the rigid duct walls and the following relationship,

$$\left(\frac{\partial^2}{\partial y^2}+\frac{\partial^2}{\partial z^2}+\kappa_{rs}^2\right)\psi_{rs}(y,z)=0\,, \tag{2.9}$$

where κ_{rs} is the characteristic wave numbers determined by the boundary conditions. Thus, the wave numbers for the axial direction without mean flow, k_{rs}, is determined by the relationship,

$$k_0^2=k_{rs}^2+\kappa_{rs}^2\,, \tag{2.10}$$

where $k_0=\omega/c_0$ is the total acoustic wave number. Additionally, the characteristic functions $\psi_{rs}(y,z)$ are orthonormal to each other which means if the area of the cross-section of the duct *S* is *A*, then:

$$\frac{1}{A}\iint_S \psi_{\mu\nu}^*(y,z)\psi_{rs}(y,z)dydz=\begin{cases}0, & \mu,\nu\neq r,s,\\ 1, & \mu,\nu=r,s.\end{cases} \tag{2.11}$$

Substituting Eq. (2.7) into the wave propagation Eq. (2.3) and noticing that $\delta(y-y')\delta(z-z')$ can be decomposed into the form as,

$$\delta(y-y')\delta(z-z')=\frac{1}{A}\sum_{r,s}\psi_{rs}^*(y',z')\psi_{rs}(y,z)\,, \tag{2.12}$$

we have,

$$\left(1-M^2\right)\frac{d^2}{dz^2}J_{rs}(x)-2ik_0M\frac{d}{dx}J_{rs}(x)+k_{rs}^2J_{rs}(x)=\frac{\psi_{rs}(y'z')}{A}Q_0\delta(x-x')\,. \tag{2.13}$$

An appropriate solution of Eq. (2.13) gives $J_{rs}(x)$ in the form

$$J_{rs}(x)=-\frac{\psi_{rs}(y',z')}{2A\sqrt{(1-M^2)\kappa_{rs}^2-k_0^2}}\left[H\left(z-z'\right)e^{-i\mathrm{K}_{rs}^{+}(x-x')}+H\left(x'-x\right)e^{i\mathrm{K}_{rs}^{-}(x-x')}\right]Q_0\,, \tag{2.14}$$

where H is the Heaviside function and $\mathrm{K}_{rs}^{\pm}$ is defined as

$$\mathrm{K}_{rs}^{\pm} = \frac{\mp k_0 M - i\sqrt{(1-M^2)\kappa_{rs}^2 - k_0^2}}{1-M^2}. \tag{2.15}$$

Thus, the acoustic velocity potential ϕ is found as,

$$\phi = \sum_{r,s} -\frac{\psi_{rs}^*(y',z')\psi_{rs}(y,z)}{2A\sqrt{(1-M^2)\kappa_{rs}^2 - k_0^2}}\left[H(x-x')e^{-i\mathrm{K}_{rs}^{+}(x-x')} + H(x'-x)e^{i\mathrm{K}_{rs}^{-}(x-x')}\right]Q_0 e^{i\omega t}. \tag{2.16}$$

According to Eq. (2.4), the sound radiation pressure generated by a point source at the source point (x', y', z') is,

$$p = i\rho_0 c_0 \sum_{r,s} \frac{\psi_{rs}^*(x',y')\psi_{rs}(x,y)}{2A\sqrt{(1-M^2)\kappa_{rs}^2 - k_0^2}}\left[H(z-z')(k_0 - M\mathrm{K}_{rs}^{+})e^{-i\mathrm{K}_{rs}^{+}(z-z')}\right.$$

$$\left. + H(x'-x)(k_0 + M\mathrm{K}_{rs}^{-})e^{i\mathrm{K}_{rs}^{-}(x-x')}\right] Q_0 e^{i\omega t}, \tag{2.17}$$

where the term $\rho_0 c_0$ can be dropped since it is always unity.

2.2.2 Distributed source in a rectangular cross-section

With the radiation pressure due to a point source at any position established in Eq. (2.17), the sound field of a source distribution in a hard-walled rectangular duct of $b \times h$, dimensions in y and z directions respectively, is formulated. Suppose that a distributed source S' is flush-mounted in the rectangular duct and is assumed to vibrate with a normal velocity $V(x',y',z')e^{i\omega t}$, where the point $(x',y',z') \in S'$. The fluid inside the duct is still assumed to be inviscid and flow uniformly in the x direction. The corresponding normal component of the fluid velocity at the distributed source S' is given by $(V - i\frac{M}{\omega}\frac{\partial V}{\partial x})e^{i\omega t}$, where M is the Mach number of

the mean flow inside the duct. According to Green's theorem and Eq. (2.17), the radiation pressure caused by such a distributed source is

$$p = i\sum_{r,s}\frac{\psi_{rs}(y,z)}{2A\sqrt{(1-M^2)\kappa_{rs}^2 - k_0^2}}\iint_{S'}\Big[H(x-x')(k_0 - M\mathrm{K}_{rs}^{+})e^{-i\mathrm{K}_{rs}^{+}(x-x')}$$

$$+ H(x'-x)(k_0 + M\mathrm{K}_{rs}^{-})e^{i\mathrm{K}_{rs}^{-}(x-x')}\Big]\psi_{rs}^{*}(y',z')(V - i\frac{M}{\omega}\frac{\partial V}{\partial x})e^{i\omega t}dS'. \qquad (2.18)$$

For the hard-walled duct described above, the normalized characteristic function for its rectangular cross-section is

$$\psi_{rs}(y,z) = \sqrt{(2-\delta_{0r})(2-\delta_{0s})}\cos\frac{r\pi y}{b}\cos\frac{s\pi z}{h}, \qquad (2.19)$$

where $\delta_{\mu\upsilon}$ is the Kronecker delta function, which is equal to zero when $\mu \neq \upsilon$ and unity when $\mu = \upsilon$. In the following presentation, the normalized characteristic function is called 'duct acoustic mode' or 'cavity acoustic mode' depending upon whether the duct or the cavity is considered.

2.3 Analytical modelling of the plate silencer

2.3.1 Coupled dynamics of the sound-plate interaction

In the two-dimensional model shown in Figure 2.1, the key element is the plate flush mounted on the wall. For the lower plate (beam), its motion may be described through the usual linear vibration equation,

$$B\frac{\partial^4\eta}{\partial x^4} + m\frac{\partial^2\eta}{\partial t^2} + (p_+ - p_-) = 0, \qquad (2.20)$$

where η is the normal displacement of the plate, $(p_+ - p_-)$ is he fluid loading on the plate located at y =0, m is the plate-to-air mass ratio and $B = Eh^3/12(1-\nu^2)$ is the normalized flexural bending stiffness of the plate.

For harmonic vibration, by introducing the plate normal vibration velocity $V = \partial\eta/\partial t = i\omega\eta$, Eq. (2.20) becomes

$$\frac{B}{i\omega}\frac{\partial^4 V}{\partial x^4} + mi\omega V + (p_+ - p_-) = 0 . \tag{2.21}$$

To solve Eq. (2.21), the standard Galerkin procedure can be followed. As the plate (beam) is simply supported at both ends, the normal velocity V can be expanded as a series of *in vacuo* modes using a local dimensionless variable $\xi = (x/L + 1/2)$,

$$V = \sum_{j=1}^{\infty} V_j \sin j\pi\xi , \tag{2.22}$$

with,

$$V_j = 2\int_0^1 V(\xi,t)\sin(j\pi\xi)d\xi . \tag{2.23}$$

The sine transform of Eq. (2.21) becomes a set of linear equations,

$$L_j V_j + \sum_{l=1}^{N} V_l Z_{jl} = -\mathrm{I}_j , \tag{2.24}$$

where L_j is the structural operator which is defined as,

$$L_j = \left[mi\omega + \frac{B}{i\omega}\left(\frac{j\pi}{L}\right)^4 \right], \quad j=1,2,3,\ldots N . \tag{2.25}$$

L_j may also be seen as the jth mode property constant of the plate. The modal impedance, Z_{jl}, is the radiation impedance on the jth vibration mode induced by the

l^{th} vibration mode, which relates the modal velocity amplitude V_l to the fluid loading $(p_+ - p_-)$. I_j is the modal coefficient of the incident wave. The expressions for Z_{jl} and I_j are found in the following subsections.

2.3.2 Radiation and cavity impedances

When applying the standard Galerkin procedure to solve the coupled dynamics Eq. (2.21), the modal impedance Z_{jl} that relates the plate vibration velocity to the fluid loading ($p_+ - p_-$), must be found. In doing so, the fluid loading can be divided into three parts (Huang, 2002). Part one is the upper surface pressure due to the specified incident wave without considering the plate response,

$$p_i(x,t) = \exp[i(\omega t - k_0 x/(1+M))]. \tag{2.26}$$

The second part is the sound radiated by the plate vibration, including the radiation pressure on the lower side p_{-rad} and the radiation pressure in the main duct p_{+rad}. The third part is due to the reflection by the vertical walls of the cavity located at $|x| = L/2$, denoted as p_{-ref}. Since both the radiation pressure p_{-rad} and the reflection pressure p_{-ref} are acoustic pressure inside the cavity, the two items can be combined into one term, namely, pressure inside the cavity p_{cav}. Therefore,

$$(p_+ - p_-) = p_i + p_{+rad} - p_{cav}. \tag{2.27}$$

Suppose $p_j(x,y)$ is the radiation pressure due to the modal vibration of unit amplitude, $\varphi_j = \sin(j\pi\xi)$. The modal impedance is then defined as

$$Z_{lj} = \int_0^1 2\sin(l\pi\xi)\, p_j(x,0)\, d\xi, \tag{2.28}$$

where subscript j refers to the source vibration mode while l refers to the resulting pressure coefficient. According to Eq. (2.27), the total impedance Z_{lj} is the sum of contribution from the radiation pressure in the main duct p_{+rad}, the acoustic pressure inside the cavity p_{cav}, denoted as Z_{+lj}, Z_{clj} respectively.

2.3.2.1 Cavity impedance, Z_{clj}

The acoustic pressure inside a lightly damped cavity can be expressed in terms of "rigid wall" modes of the cavity (Nelson, 1993; Kuttruff, 2000). For the two-dimensional configuration considered here, the normalized pressure inside the cavity can be written as,

$$p_{cav}(x,y) = \sum_{r,s} \frac{-i\omega\psi_{rs}(x,y)}{Lh_c(\kappa_{rs}^2 - k_0^2 + 2i\zeta_{rs}\kappa_{rs}k_0)} \int_0^1 V(x',0)\psi_{rs}(x',0)dx' \quad , \tag{2.29}$$

where $V(x',0)$ is the normal velocity over the flexible panel, ζ_{rs} is the damping ratio of the $(r, s)^{th}$ acoustic mode $\psi_{rs}(x,y)$, L is the length of the cavity, h_c is the height of the cavity, and κ_{rs} is the corresponding acoustic wave-number of the acoustic mode $\psi_{rs}(x,y)$, with $\psi_{rs}(x,y)$ and ζ_{rs} given as,

$$\psi_{rs}(x,y) = \sqrt{(2-\delta_{0r})(2-\delta_{0s})}\cos(\frac{r\pi x}{L})\cos(\frac{s\pi y}{h_c}) \quad , \tag{2.30}$$

$$\kappa_{rs}^2 = \left(\frac{r\pi}{L}\right)^2 + \left(\frac{s\pi}{h_c}\right)^2 . \tag{2.31}$$

Therefore, the cavity pressure caused by the jth modal vibration of unit amplitude, $\varphi_j = \sin(j\pi\xi)$, is given as,

$$p_{cav,j}(x,y) = \sum_{r,s} \frac{-i\omega\psi_{rs}(x,y)}{h_c(\kappa_{rs}^2 - k_0^2 + 2i\xi_{rs}\kappa_{rs}k_0)} \int_L \sin(j\pi\xi')\psi_{rs}(x',0)d\xi'$$

$$= \sum_{r,s} \frac{-ik(2-\delta_{0r})(2-\delta_{0s})\cos(r\pi x/L)\cos(s\pi y/h_c)}{h_c(\kappa_{rs}^2 - k_0^2 + 2i\xi_{rs}\kappa_{rs}k_0} \int_0^1 \sin(j\pi\xi')\cos(r\pi\xi')d\xi'. \qquad (2.32)$$

According to Eq. (2.28), the component Z_{cjl} of the modal impedance that contributes from the acoustic pressure inside the cavity is given as,

$$Z_{clj} = \int_0^1 2\sin(l\pi\xi)\, p_{cav,j}(x,0)d\xi$$

$$= \sum_{r,s} \frac{-i2k_0(2-\delta_{04})(2-\delta_{0s})}{h_c(\kappa_{rs}^2 - k^2 + 2i\xi_{rs}\kappa_{rs}k_0)} \int_0^1 \left[\int_0^1 \sin(j\pi\xi')\cos(r\pi\xi')\cos(r\pi\xi)d\xi' \right] \sin(l\pi\xi)d\xi$$

$$= \sum_{r,s} \frac{-i2k_0(2-\delta_{0r})(2-\delta_{0s})}{h_c(\kappa_{rs}^2 - k_0^2 + 2i\xi_{rs}\kappa_{rs}k_0)} I_{c,jl}. \qquad (2.33)$$

In Eq. (2.33), $I_{c,jl}$ is the result of double integration over the panel surface,

$$I_{c,jl} = \int_0^1 \left[\int_0^1 \sin(j\pi\xi')\cos(r\pi\xi')\cos(r\pi\xi)d\xi' \right] \sin(l\pi\xi)d\xi, \qquad (2.34)$$

when $j,l \neq r$, $I_{c,jl}$ is given as,

$$I_{c,jl} = \frac{jl[1-\cos(j+r)\pi)]\cdot[1-\cos(l+r)\pi]}{\pi^2(j^2-r^2)(l^2-r^2)}. \qquad (2.35)$$

When $j,l = r$, the above double integration is zero. Here, one observation can be made that the subscript *j* and *l* are interchangeable, or,

$$Z_{cjl} = Z_{clj}. \qquad (2.36)$$

2.3.2.2 Radiation impedance in the main duct, Z_{+lj}

In order to find the radiation impedance in the main duct, Z_{+lj}, the radiation pressure in the main duct with flow must be obtained first. Theoretical formula for radiation pressure of a distributed source in a hard-walled rectangular duct with non-reflecting terminations and mean flow has been found in Eq. (2.18). For the two-dimensional plate silencer studied here, the radiation pressure in the main duct can be written as,

$$p_{+rad} = i\frac{L}{2}\sum_{r=0}^{\infty}\frac{\psi_r(y)}{\sqrt{(1-M^2)(r\pi)^2-k_0^2}}\int_0^1\Big[H(x-x')(k_0-M\mathrm{K}_r^+)e^{-i\mathrm{K}_r^+(x-x')}$$

$$+H(x'-x)(k_0+M\mathrm{K}_r^-)e^{i\mathrm{K}_r^-(x-x')}\Big]\psi_r^*(y')(V-i\frac{M}{\omega}\frac{\partial V}{\partial x'})d\xi\,, \tag{2.37}$$

where H( ) is the Heaviside function and

$$\psi_r(y)=\sqrt{2-\delta_{0r}}\cos(r\pi y)\,, \tag{2.38}$$

$$\mathrm{K}_r^{\pm}=\frac{\mp k_0M-i\sqrt{(1-M^2)(r\pi)^2-k_0^2}}{1-M^2}\,. \tag{2.39}$$

It is noted that the normal component of the fluid velocity at the flexible plate is divided into two parts: one is the local velocity $Ve^{i\omega t}$ which corresponds to the normal velocity of the plate; the other one is the convective term due to the mean flow, ($-i\frac{M}{\omega}\frac{\partial V}{\partial x'}e^{i\omega t}$). For the modal vibration of unit amplitude $V=\sin(j\pi\xi')$, the convective term then becomes $-i\frac{M\cdot j\pi}{L\omega}\cos(j\pi\xi)e^{i\omega t}$. Hence, according to Eq.

(2.28), the component Z_{+lj} of the modal impedance that contributes from the radiation pressure in the main duct is,

$$Z_{+lj} = \int_0^1 2\sin(l\pi\xi)\, p_{+rad,j}(x,0)d\xi$$

$$= iL\sum_{r=0}^{\infty}\frac{(2-\delta_{0r})}{\sqrt{(1-M^2)(r\pi)^2-k_0^2}}\left(I_2(r,j,l) - i\frac{M\cdot j\pi}{L\omega}I_{2conv}(r,j,l)\right). \qquad (2.40)$$

Here, $I_2(r,j,l)$ and $I_{2conv}(r,j,l)$ are the double integrations defined as below:

$$I_2(r,j,l) = \int_0^1\left[\int_0^1 I(\xi,\xi')d\xi'\right]\sin(l\pi\xi)d\xi\,, \qquad (2.41)$$

$$I_{2conv}(r,j,l) = \int_0^1\left[\int_0^1 I_{conv}(\xi,\xi')d\xi'\right]\sin(l\pi\xi)d\xi\,, \qquad (2.42)$$

whrer, $I(\xi,\xi')$ and $I_{conv}(\xi,\xi')$ are defined as,

$$I(\xi,\xi') = [H(\xi-\xi')(k_0 - M\mathrm{K}_r^+)e^{-i\mathrm{K}_r^+L(\xi-\xi')} +$$

$$H(\xi'-\xi)(k_0 + M\mathrm{K}_r^-)e^{i\mathrm{K}_r^-L(\xi-\xi')}]\sin(j\pi\xi')\,, \qquad (2.43)$$

$$I_{conv}(\xi,\xi') = [H(\xi-\xi')(k_0 - M\mathrm{K}_r^+)e^{-i\mathrm{K}_r^+L(\xi-\xi')} +$$

$$H(\xi'-\xi)(k_0 + M\mathrm{K}_r^-)e^{i\mathrm{K}_r^-L(\xi-\xi')}]\cos(j\pi\xi')\,, \qquad (2.44)$$

The result of the double integration $I_2(r,j,l)$ is,

$$I_2(r,j,l) = \frac{j\pi l\pi(k_0 + M\mathrm{K}_r^-)\cos(j\pi)[\cos(l\pi) - e^{-i\mathrm{K}_r^-L}]}{[(j\pi)^2 - (\mathrm{K}_r^-L)^2][(l\pi)^2 - (\mathrm{K}_r^-L)^2]}$$

$$+\frac{j\pi l\pi(k_0 - M\mathrm{K}_r^+)[1-\cos(l\pi)e^{-i\mathrm{K}_r^+L}]}{[(j\pi)^2 - (\mathrm{K}_r^+L)^2][(l\pi)^2 - (\mathrm{K}_r^+L)^2]}$$

$$+\frac{1}{2}\left[\frac{(k_0 - M\mathrm{K}_r^+)(i\mathrm{K}_r^+L)}{(j\pi)^2 - (\mathrm{K}_r^+L)^2} + \frac{(k_0 + M\mathrm{K}_r^-)(i\mathrm{K}_r^-L)}{(j\pi)^2 - (\mathrm{K}_r^-L)^2}\right], \quad \text{for } j=l \qquad (2.45)$$

and,

$$I_2(r,j,l)=\frac{j\pi l\pi(k_0+M\mathrm{K}_r^-)\cos(j\pi)[\cos(l\pi)-e^{-i\mathrm{K}_r^-L}]}{[(j\pi)^2-(\mathrm{K}_r^-L)^2][(l\pi)^2-(\mathrm{K}_r^-L)^2]}$$

$$+\frac{j\pi l\pi(k_0-M\mathrm{K}_r^+)[1-\cos(l\pi)e^{-i\mathrm{K}_r^+L}]}{[(j\pi)^2-(\mathrm{K}_r^+L)^2][(l\pi)^2-(\mathrm{K}_r^+L)^2]}-\frac{jl(k_0-M\mathrm{K}_r^+)[1-\cos(j+l)\pi]}{(l^2-j^2)[(j\pi)^2-(\mathrm{K}_r^+L)^2]}$$

$$+\frac{jl(k_0+M\mathrm{K}_r^-)[1-\cos(j+l)\pi]}{(l^2-j^2)[(j\pi)^2-(\mathrm{K}_r^-L)^2]}\ ,\qquad \text{for } j\neq l. \tag{2.46}$$

Note that there are chances that $(j\pi)$ and/or $(l\pi)\to\mathrm{K}_r^+L$ or K_r^-L when r=0. In such case, some items in Eqs. (2.45) and (2.46) become $\frac{0}{0}$ or $\infty-\infty$ type, all of which can be shown to be finite (see the Appendix). For example, when $(l\pi)\to\mathrm{K}_r^+L$ ($j\neq l$), the double integration $I_2(r,j,l)$ becomes,

$$I_2(r,j,l)=-\frac{i(k_0-M\mathrm{K}_0^+)j\pi}{2[(j\pi)^2-(\mathrm{K}_0^+L)^2]}+\frac{j\pi l\pi(k_0+M\mathrm{K}_0^-)\cos(j\pi)[\cos(l\pi)-e^{-i\mathrm{K}_0^-L}]}{[(j\pi)^2-(\mathrm{K}_0^-L)^2][(l\pi)^2-(\mathrm{K}_0^-L)^2]}$$

$$-\frac{jl(k_0-M\mathrm{K}_0^+)[1-\cos(j+l)\pi]}{(l^2-j^2)[(j\pi)^2-(\mathrm{K}_0^+L)^2]}+\frac{jl(k_0+M\mathrm{K}_0^-)[1-\cos(j+l)\pi]}{(l^2-j^2)[(j\pi)^2-(\mathrm{K}_0^-L)^2]}, \tag{2.47}$$

Similarly, the result of the double integration $I_{2conv}(r,j,l)$ can be found as,

$$I_{2conv}(r,j,l)=-\frac{l\pi(-i\mathrm{K}_r^+L)(k_0-M\mathrm{K}_r^+)[1-\cos(l\pi)e^{-i\mathrm{K}_r^+L}]}{[(j\pi)^2-(\mathrm{K}_r^+L)^2][(l\pi)^2-(\mathrm{K}_r^+L)^2]}$$

$$-\frac{l\pi(i\mathrm{K}_r^-L)(k_0+M\mathrm{K}_r^-)\cos(j\pi)[e^{-i\mathrm{K}_r^-L}-\cos(l\pi)]}{[(j\pi)^2-(\mathrm{K}_r^-L)^2][(l\pi)^2-(\mathrm{K}_r^-L)^2]}$$

$$+\frac{1}{2}\left[\frac{j\pi(k_0-M\mathrm{K}_r^+)}{(j\pi)^2-(\mathrm{K}_r^+L)^2}-\frac{j\pi(k_0+M\mathrm{K}_r^-)}{(j\pi)^2-(\mathrm{K}_r^-L)^2}\right],\qquad \text{for } j=l, \tag{2.48}$$

and,

$$I_{2conv}(r,j,l)=-\frac{l\pi(-i\mathrm{K}_r^+L)(k_0-M\mathrm{K}_r^+)[1-\cos(l\pi)e^{-i\mathrm{K}_r^+L}]}{[(j\pi)^2-(\mathrm{K}_r^+L)^2][(l\pi)^2-(\mathrm{K}_r^+L)^2]}$$

$$-\frac{l\pi(i\mathrm{K}_r^- L)(k_0 + M\mathrm{K}_r^-)\cos(j\pi)[e^{-i\mathrm{K}_r^- L} - \cos(l\pi)]}{[(j\pi)^2 - (\mathrm{K}_r^- L)^2][(l\pi)^2 - (\mathrm{K}_r^- L)^2]}$$

$$+\frac{l(k_0 - M\mathrm{K}_r^+)(i\mathrm{K}_r^+ L)[1-\cos(j+l)\pi]}{\pi(l^2 - j^2)[(j\pi)^2 - (\mathrm{K}_r^+ L)^2]}$$

$$+\frac{l(k_0 + M\mathrm{K}_r^-)(i\mathrm{K}_r^- L)[1-\cos(j+l)\pi]}{\pi(l^2 - j^2)[(j\pi)^2 - (\mathrm{K}_r^- L)^2]}, \qquad \text{for } j \neq l. \tag{2.49}$$

When $(j\pi)$ and/or $(l\pi) \to \mathrm{K}_r^+ L$ or $\mathrm{K}_r^- L$ at r=0, the double integration $I_{2conv}(r, j, l)$ can also be shown to be finite (see Appendix). Note that we assume that $\mathrm{K}_0^+ L$ and $\mathrm{K}_0^- L$ do not coincide with $j\pi$ or $l\pi$ at the same time in the above formulation. This assumption is true only when $(\mathrm{K}_0^- L - \mathrm{K}_0^+ L)$ is less than π, that is,

$$\left(\frac{1}{1-M} - \frac{1}{1+M}\right) k_0 L < \pi \,. \tag{2.50}$$

Assuming L and $k_0 = 2\pi f$ are given, the non-equality Eq.(2.50) leads to

$$M < \sqrt{(2fL)^2 + 1} - 2fL \,. \tag{2.51}$$

For a typical plate silencer design of cavity length $L = 5$, and assuming $f_{\max} = 0.25$, the non-equality equation (2.51) requires M<0.19 (or U^* <66*m/s*), which is much higher than the flow speed in a common ventilation system. Also note that, the radiation impedance matrix $[Z_{+lj}]$ is not symmetrical unless in the case of M=0.

2.3.3 Transmission loss, TL

With the modal radiation and cavity reflection impedances found, the dynamics Eq. (2.24) can be cast as a truncated set of linear equations for the modal vibration amplitudes, V_j, $j = 1,2,3,\ldots,N$,

$$\begin{bmatrix} Z_{11}+L_1 & Z_{12} & \cdots & Z_{1N} \\ Z_{21} & Z_{22}+L_2 & \cdots & Z_{2N} \\ \cdots & \cdots & \cdots & \cdots \\ Z_{N1} & Z_{N2} & \cdots & Z_{NN}+L_N \end{bmatrix} \begin{bmatrix} V_1 \\ V_2 \\ \vdots \\ V_N \end{bmatrix} + \begin{bmatrix} \mathrm{I}_1 \\ \mathrm{I}_2 \\ \vdots \\ \mathrm{I}_N \end{bmatrix} = 0\,, \tag{2.52}$$

where,

$$Z_{lj} = Z_{+lj} + Z_{clj}\,, \tag{2.53}$$

and the modal coefficient of the incident wave, I_j, is found as,

$$\mathrm{I}_j = \int_0^1 p_i\, 2\sin(j\pi\xi)d\xi$$

$$= 2j\pi e^{i\mathrm{K}_0^+ L/2}\left[\frac{1-e^{i(-\mathrm{K}_0^+ L + j\pi)}}{(j\pi)^2 - (\mathrm{K}_0^+ L)^2}\right]\,, \tag{2.54}$$

with,

$$\lim_{\mathrm{K}_0^+ L \to j\pi} \frac{1-e^{i(-\mathrm{K}_0^+ L + j\pi)}}{(j\pi)^2 - (\mathrm{K}_0^+ L)^2} = -\frac{i}{2\mathrm{K}_0^+ L}\,. \tag{2.55}$$

Equation (2.52) can be solved via the inversion of matrix. In the actual calculation, modal truncation is necessary. The plate modes are truncated to *N*=25. For instance, the subscripts of *j* and *l* in Eqs. (2.33), and (2.40) range from 1 to 25, and the final impedance matrix $[Z_{jl}]$ is then of the size 25×25. For the duct acoustic mode ψ_r in Eq. (2.37) and cavity acoustic mode ψ_{rs} in Eq. (2.29), *r* and *s* are from 0

to 50. Numerical results show that the number of modes is normally enough as further increase in the number does not make significant difference for the purpose of this study. One such example can be seen in Figure 2.3 in which the TL spectra with different vibration modal truncation (N=25, 50 and 100) are compared.

The total sound pressure transmitted to the downstream is found by adding the incident wave p_i to the far-field radiation wave p_{+rad}, which can be found with the help of Eq. (2.37) by taking only the plane wave mode with n=0 for x>L/2:

$$p_t = p_{+rad}\big|_{r=0,x\to+\infty} + p_i \,, \tag{2.56}$$

and,

$$\frac{p_{+rad}\big|_{r=0,x\to+\infty}}{p_i} = \frac{L}{2(1+M)}\sum_{j=1}^{\infty} V_j \int_0^1 \left[\sin(j\pi\xi') - i\frac{Mj\pi}{L\omega}\cos(j\pi\xi')\right] e^{i\mathrm{K}_0^+ L(\xi'-\frac{1}{2})} d\xi' ,$$

$$= \sum_{j=1}^{\infty} V_j T_j \,, \tag{2.57}$$

$$T_j = \frac{j\pi L}{2(1+M)} \cdot \frac{[1-e^{i(j\pi+\mathrm{K}_0^+ L)}]}{(j\pi)^2 - (\mathrm{K}_0^+ L)^2}\left(1 - \frac{M\mathrm{K}_0^+ L}{L\omega}\right) e^{-i\mathrm{K}_0^+ L/2)} \,. \tag{2.58}$$

Hence, for an incident wave of unit amplitude, the transmission loss of the plate silencer can be calculated as,

$$TL = -20\log_{10}|p_t| \,. \tag{2.59}$$

Denoting the reflected sound as $p_r e^{i\mathrm{K}_0^- x}$, the coefficients of sound power reflected and absorbed, if there is damping in the system, are calculated as,

$$\beta = |p_r|^2 \,, \qquad \alpha = 1 - |p_r|^2 - |p_t|^2 \,. \tag{2.60}$$

The complex amplitude of the reflected sound p_r is the sum of contributions made by all individual plate vibration modes, which is found as,

$$p_r = \frac{L}{2(1-M)} \sum_{j=1}^{\infty} V_j \int_0^1 \left[\sin(j\pi\xi') - i\frac{Mj\pi}{L\omega}\cos(j\pi\xi') \right] e^{i\bar{\mathrm{K}}_0 L(\frac{1}{2}-\xi')} d\xi'$$

$$= \sum_{j=1}^{\infty} V_j R_j \,, \tag{2.61}$$

where R_j is the complex amplitude of the reflected sound by the induced vibration of the jth mode with unite amplitude,

$$R_j = \frac{j\pi L}{2(1-M)} \cdot \frac{[1-e^{i(j\pi-\bar{\mathrm{K}}_0 L)}]}{(j\pi)^2 - (\bar{\mathrm{K}}_0 L)^2} \left(1 + \frac{M\bar{\mathrm{K}}_0 L}{L\omega} \right) e^{i\bar{\mathrm{K}}_0 L/2} \,, \tag{2.62}$$

as $\bar{\mathrm{K}}_0 L \to j\pi$, $\dfrac{[1-e^{i(j\pi-\bar{\mathrm{K}}_0 L)}]}{(j\pi)^2 - (\bar{\mathrm{K}}_0 L)^2} \to -\dfrac{i}{2\bar{\mathrm{K}}_0 L}$.

Note that only the vibration of the lower plate is considered in the above modelling process from Eq. (2.20) to Eq. (2.62), and the upper plate is assumed to be rigid. For the two plate-cavity system shown in Figure 2.1, the two plates can be shown to respond in an identical manner. The pressure loading on the upper side of the of the lower plate p_{+rad}, must account for that caused by the opposite plate, which is the same as the reciprocal pressure on y=1 caused by the lower plate. The latter can be calculated by setting y=1 in $\psi_r(y)$ in Eq. (2.37). Also, the contributions from the vibration of the opposite plate should be taken into account in the calculation of the transmitted sound p_t and the reflected sound p_r.

2.3.4 Conservation of acoustic energy

For a hard-walled duct with mean flow, the acoustic intensity can be written as (Blokhintsev, 1946),

$$I = (\frac{p}{\rho_0} + Mu)(\rho_0 u + \frac{pM}{c_0^2}), \tag{2.63}$$

where M is the Mach number of the mean flow. In view that only plane wave accounts for the transmitted and reflected sound, the total incident acoustic energy flux W_{in}, the total transmitted acoustic energy flux W_t and the total reflected acoustic energy flux W_r can be written as,

$$W_{in} = \int_S I_{in} dS = \frac{S}{\rho_0 c_0}(1+M)^2 p_i^2, \tag{2.64}$$

$$W_t = \int_S I_t dS = \frac{S}{\rho_0 c_0}(1+M)^2 p_t^2, \tag{2.65}$$

$$W_r = \int_S I_r dS = \frac{S}{\rho_0 c_0}(1-M)^2 p_r^2. \tag{2.66}$$

Following the law of conservation of energy, if damping effect is neglected, the total reflected acoustic energy flux and transmitted acoustic energy flux should be equal to the total incident acoustic energy flux, that is,

$$|W_{in}| = |W_t| + |W_r|. \tag{2.67}$$

Hence, for an incident wave of unit amplitude, the conservation of energy can be examined via the normalized error,

$$\delta_E = 1 - \frac{|W_t|}{|W_{in}|} - \frac{|W_r|}{|W_{in}|} = 1 - |p_t|^2 - \frac{(1-M)^2}{(1+M)^2}|p_r|^2. \tag{2.68}$$

2.4 Performance analysis without mean flow effect

2.4.1 Transmission loss spectrum

The overall goal of this study is to develop a broadband silencer which works effectively in the low frequency range. The stopband of the proposed plate silencer is defined as a continuous frequency band $f \in [f_1, f_2]$, in which the transmission loss is above a certain criterion level TL_{cr}. The criterion value may be chosen as the peak TL for an expansion chamber with the added volume which is three times the actual added volume used by the plate silencer (Huang, 2004). For a silencer with two cavities of depth *h*, as in the case investigated below, the criterion level can be calculated and rounded up to TL_{cr} =10 dB. As a preliminary step toward the understanding of the functioning mechanism of the plate silencer, the performance of a plate silencer without mean flow (*M*=0) is studied with the following set of parameters:

$$L=5h, \quad h_c=h, \quad m=1, \quad B_{opt}=0.129, \tag{2.69}$$

where B_{opt} is the optimal bending stiffness which guarantees the widest stopband with the other parameters fixed (Huang, 2006). Note that the silencing performance of the plate silencer is subject to several parameters, for example, the cavity shape and the plate property. Effects of these design parameters will be addressed in the next chapter.

Figure 2.3 shows the TL spectrum for the simply-supported plate silencer (solid line) specified in (2.69) together with the performance of the expansion chamber of the same geometrical configuration (dashed line). The TL of the simply-supported

plate silencer is calculated with different numbers of vibration modes. As shown in Figure 2.3, no noticeable difference can be observed as we increase the number of modes from N=25 to N=50 and 100. So, N=25 can be regarded as sufficient enough for the purpose of this study, and the vibration modes higher than N=25 is truncated in the following calculation. For the plate silencer, a stopband of $f \in [0.0353, 0.149]$ is observed with TL_{cr} =10 dB. Noting that the peak TL of the expansion chamber is below 5 dB, the plate silencer outperforms the expansion chamber obviously. Meanwhile, four spectral peaks can be observed at, f = 0.0375, 0.095, 0.124, and 0.205 in the TL curve of the plate silencer, which contrasts the smooth TL curve of the expansion chamber. The TL at the four peaks tends to infinity as the frequency resolution increases, indicating that complete sound reflection occurs at these frequencies.

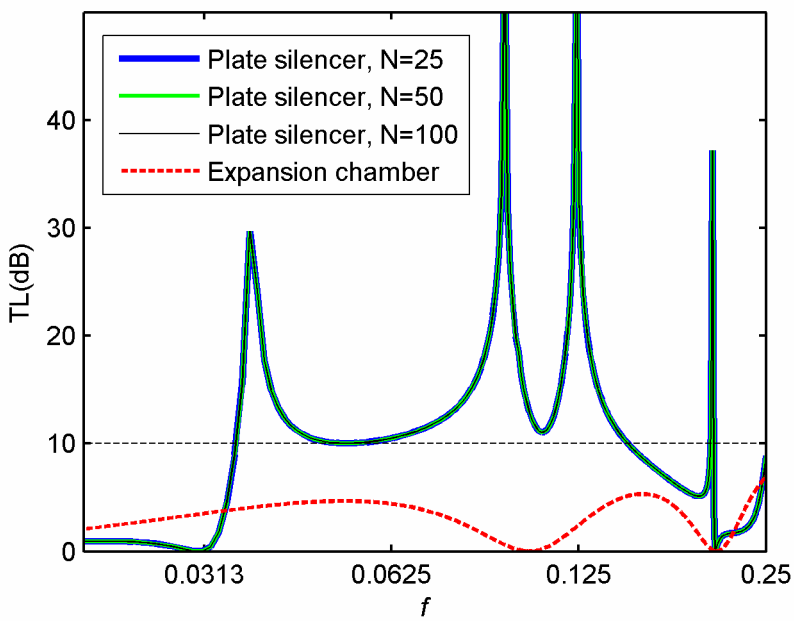

Figure 2.3: TL comparison of the simply supported plate silencer (solid line) with the expansion chamber of the same cavity geometry of L=5h, h_c=h. The plate has a mass ratio m=1 and optimal bending stiffness B_{opt} =0.129. The TL of the plate silencer is calculated with different numbers of vibration modes N.

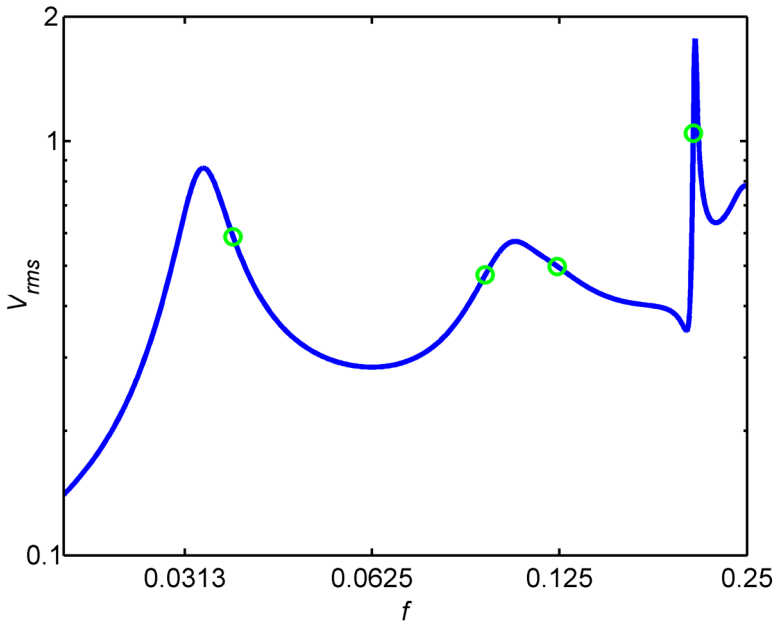

Figure 2.4: Root-mean-square (rms) level of the plate vibration. The open circles indicate the corresponding TL peaks of the plate silencer.

Attempts are made to explain the formation mechanism for the spectral peaks in the TL spectrum. One would suspect that the occurrence of the spectral peaks is related to some kind of resonances in the plate silencer, just as the peak of a Helmholtz resonator appears at its resonance frequency. Because the sound reflection is solely caused by plate vibration, one direct guess might be that the spectral peaks are generated by the resonances of the plate vibration. Figure 2.4 shows the root-mean-square level of the plate response calculated by,

$$V_{rms} = \left(\sum \left|V_j\right|^2 / 2\right)^{1/2}, \tag{2.70}$$

where V_j is the amplitude of the jth *in vacuo* vibration mode as defined in Eq. (2.23). The four spectral peaks shown in Figure 2.3 are marked by open circles in Figure 2.4

for easy identification. Obviously, the TL peaks do not correspond to the peaks of the magnitude level of the plate vibration and such a guess is wrong. In other words, the effectiveness of the plate to reflect sound does not solely depend on the amplitude of the induced plate vibration. As the vibration of the plate is coupled strongly with the backing cavity, the free vibration of the coupled plate is investigated in the following with a view to reveal the relationship between the plate vibration and the TL peaks.

2.4.2 Free vibration of a simply supported plate backed by rigid cavity

The free vibration of the lower plate shown in Figure 2.1 is studied by neglecting the radiation impedance of the fluid inside the duct. Basically, there are two different ways to conduct the modal analysis of the coupled plate in such a plate-cavity system. One approach is to do a full modal analysis of the sound-structure interaction problems, as reported by Bokil and Shirahatti (1994). As the coupling matrix for the plate-cavity system is skew-symmetric, complicated mathematical manipulation is necessary for the eigenvalue extraction routines. Alternatively, the plate vibration can be studied separately, with the effect of the backing cavity included as acoustic stiffness (Pretlove, 1965) in the stiffness matrix of the plate. Because the cross acoustic stiffness is a function of frequency, iterative eigenvalue techniques can be adopted for finding eigenvalues and eigenvectors. In this study, the free vibration of the coupled plate is analyzed following the procedure given by Pretlove (1965).

Table 2.1 lists the natural frequencies of the plate (beam) in vacuum, the rigid cavity (channel) and the plate-cavity coupling system. Due to the strong interaction between the plate and the backing cavity, the natural frequencies of the coupled plate-cavity system differ greatly from those of the uncoupled systems. Recall that

the first four resonant frequencies of the plate silencer found in Section 2.4.1 are f = 0.0375, 0.095, 0.125 and 0.205. Because the radiation impedance of the external fluid is assumed to be negligible in the modal analysis of the beam-cavity system, no coincidence is expected between the resonant frequency of the plate silencer and the natural frequencies of the beam-cavity system.

Table 2.1 Natural frequencies of the beam in vacuum, the rigid cavity and the beam-cavity coupling system.

Mode Number	1	2	3	4	5	6
Beam in vacuum	0.0226	0.0903	0.2031	0.3611	-	-
Rigid cavity	0.1	0.2	0.3	0.4	-	-
Beam-cavity coupling system	0.0467	0.1057	0.1586	0.1629	0.2499	0.2702

The first three vibration modes of the coupled plate (beam) are shown in Figures 2.5, 2.6 and 2.7 in solid lines, together with the vibration response of the plate at the corresponding TL peaks for comparison (in dashed lines). When the frequency is extremely low, the cavity is compact and very stiff to the volume-displacing mode. As a result, the first coupled mode shape shown in Figure 2.5 looks rather like the second *in vacuo* mode which is almost not affected by the incompressibility of the air in the cavity. The second coupled mode is controlled by the first cavity resonance. Figure 2.6 shows that the second coupled mode is mainly a combination of the first and third *in vacuo* modes. As the first cavity mode is symmetrical while the second *in vacuo* vibration mode is anti-symmetrical, the second *in vacuo* vibration mode is almost prohibited. The third coupled mode shown in Figure 2.7 looks almost the

same as the first coupled mode. On the whole, Figures 2.5-2.7 demonstrate remarkable similarity between the vibration modes of the plate-cavity system and the plate vibration responses at the TL peaks, which suggests that the occurrence of the spectral peak of the plate silencer is closely related to the resonances of the beam-cavity system. However, since the radiation impedance in the main duct is neglected, it is insufficient to draw a definite conclusion that the TL peaks is caused by the resonances of the plate-cavity system.

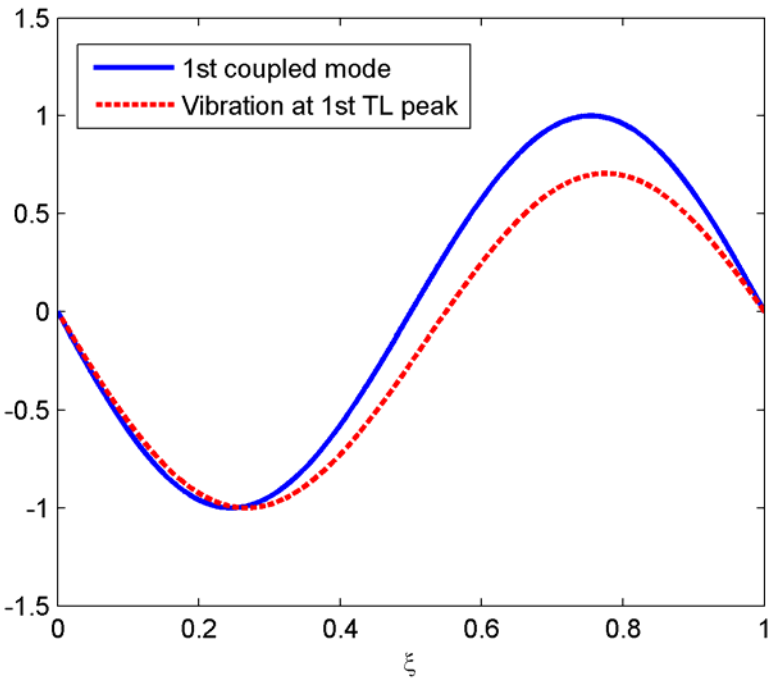

Figuer 2.5: Comparison of the first vibration mode of the beam-cavity system and the plate response of the plate silencer at the first TL spectral peak.

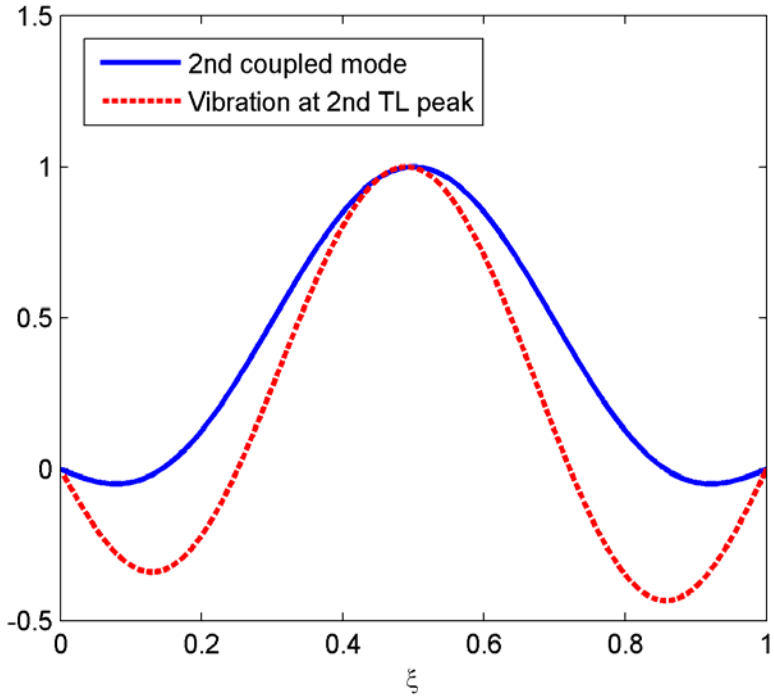

Figuer 2.6: Comparison of the second vibration mode of the beam-cavity system and the plate response of the plate silencer at the second TL spectral peak.

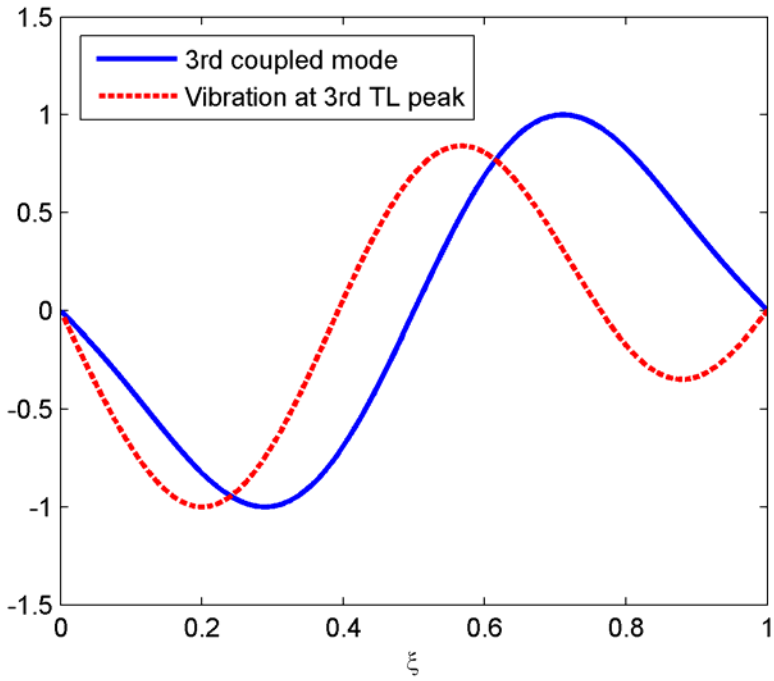

Figuer 2.7: Comparison of the third vibration mode of the beam-cavity system and the plate response of the plate silencer at the third TL spectral peak.

2.5 Effect of mean flow

In practice, the duct is almost always used to carry some kind of fluid, for instance, air in the ventilation system. The major concern about the effect of flow on the plate silencer can be divided into two parts. The first is the capability of the plate to reflect noise due to the mean flow. Since the existence of flow may influence inevitably the fluid-structure coupling and then the silencing performance, its effect on the plate silencer must be examined at the design stage. The second is about the flow-induced vibration of the thin plate. As the flexible plate is exposed to the flow inside the duct, there are chances of flow-induced flexural instability (Ellen, 1973) and the compliant plate may also influence the stability of the flow over it (Yeo and Lim, 1994). The instability grows out of infinitesimal disturbance due to an intrinsic mechanism of energy transfer from the mean flow to the vibration of a finite frequency (Huang, 2001b). If such instability exists, it would only get quenched by nonlinear effects. Fortunately, previous experimental study (Choy and Huang, 2005) has suggested that such kind of flow-induced instability does not happen for the typical flow speed in common ventilation system. Hence, the effect of flow is limited to its influence on the silencing performance, and the flow-induced instability is not covered in the current study.

The effect of mean flow on the capability of the plate to reflect noise is investigated numerically. Figure 2.8 shows the variation of the TL spectra with respect to the Mach number, M, for the simply-supported plate silencer specified in (2.69). The thick solid curve is the reference case of no-flow (M=0). As the flow velocity increases from M=0 to M=0.03, 0.045 and 0.09, the overall TL level decreases gradually, and the spectral peaks are smoothed out. When the flow velocity

increases to M=0.09, the first spectral peak becomes so smooth that it almost disappears. On the other hand, the second and third spectral peaks drift apart, which causes the trough between them, around f =0.11, falls below the 10 dB criterion level for M>0.03. Generally speaking, the effect of mean flow on the silencing performance of the plate silencer is negative. The existence of mean flow inside the duct will smooth out and shift the TL peaks and make the overall TL level of the silencer deteriorate.

Analysis of the modal impedance reveals some insights into the reasons behind the performance deterioration for M > 0. When M = 0, the total modal impedance

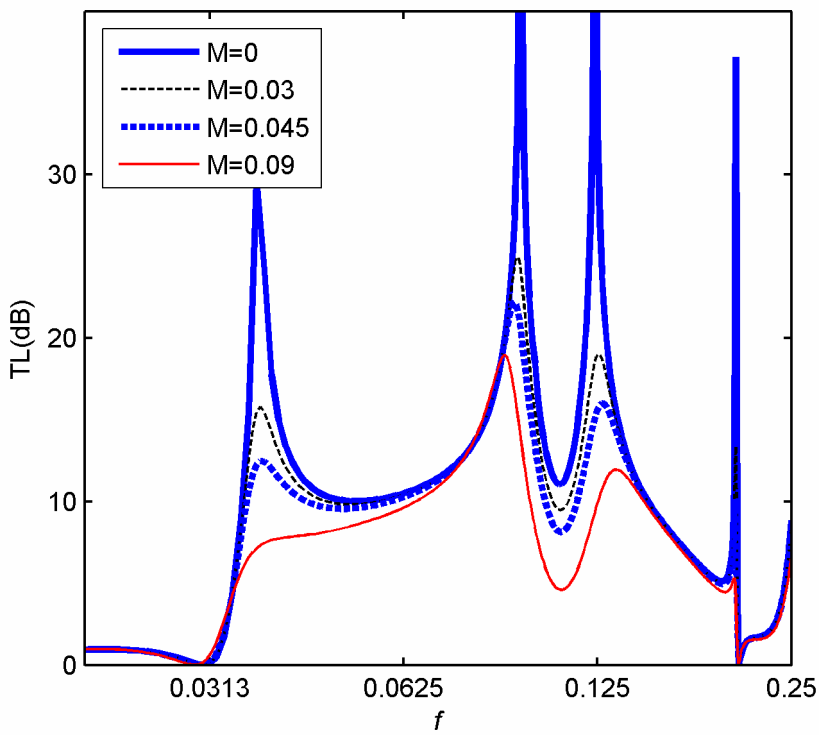

Figure 2.8: Variation of TL spectrum with respect to the Mach number, M, for the simply-supported plate silencer with L =5, h_c =1, m =1 and B=0.129.

matrix $[Z_{jl}]$ is symmetric and the odd-even modes are decoupled. However, when there is a mean flow (M $\neq$ 0), cross-modal interaction is found in the radiation impedance matrix in the main duct, Z_{+jl}, which corresponds to the radiation by all modes coupled to each other. Take the frequency, *f*=0.011, for example. When M=0, the radiation impedance in the main duct by the first four modes is found as,

$$[Z_{+jl}]=\begin{bmatrix} 2.249-2.361i & 0 & -0.182-1.148i & 0 \\ 0 & 2.032+1.044i & 0 & 0.767-0.121i \\ -0.182-1.148i & 0 & 0.0147+0.649i & 0 \\ 0 & 0.767-0.121i & 0 & 0.289+0.294i \end{bmatrix}. \qquad (2.71)$$

Elements such as Z_{+12}, Z_{+14}, Z_{+21}, and Z_{+23} in (2.71) are zero, which indicates that the radiations by odd and even modes are completely decoupled to each other. When M=0.045, the corresponding radiation impedance is calculated as,

$$[Z_{+jl}]=\begin{bmatrix} 2.246-2.371i & 0.069+0.190i & -0.193-1.147i & 0.061+0.046i \\ -0.069-0.190i & 2.056+1.041i & -0.208+0.109i & 0.770-0.132i \\ -0.193-1.148i & 0.208-0.109i & 0.021+0.671i & -0.077-0.039i \\ -0.061-0.046i & 0.770-0.132i & 0.077+0.039i & 0.289+0.303i \end{bmatrix}. \qquad (2.72)$$

Unlike in (2.71), the values for odd-even cross-modal elements are no longer zero for M=0.045, and the whole matrix becomes asymmetric. The cross-modal interaction is caused by several reasons, among which the extra term $I_{2conv}(r, j, l)$ due to the convective velocity in Eq. (2.40) contributes most. It is deemed that the cross-modal interaction for $M \neq 0$ is closely related to the performance degradation of the plate silencer, however, further effort is needed to find out the specific reasons.

As a remedy to the performance deterioration, plate with higher bending stiffness than that necessary for the no-flow condition can be employed to overcome the effect of mean flow. Theoretical study shows that the spectral movement with

respect to the increasing Mach number is similar to the reduction of plate bending stiffness. Hence, a proper increase of bending stiffness will improve the silencing performance when there is a flow. Figure 2.9 compares the TL spectrum for different bending stiffness under the same flow speed, M=0.045. As the bending stiffness increases from B=0.129 (solid line) to B=0.14 (dashed line), the trough between the second and third peaks is lifted above the criterion level TL_{cr} =10 dB, although the overall stopband shrinks a little. .

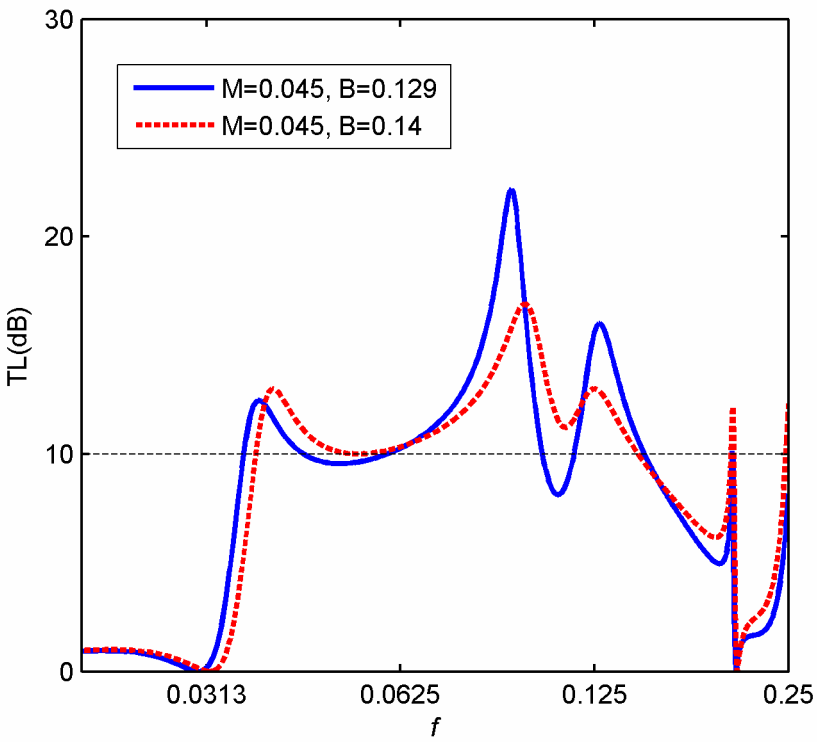

Figure 2.9: Predicted TL spectra of a plate silencer in a flow duct with different bending stiffness (solid line: B=0.129; dashed line: B=0.14). The Mach number of the mean flow is, M=0.045. The cavity is of L =5 and h_c =1. The mass ratio of the plate is m =1.

2.6 Summary

A two-dimensional theoretical model has been established for the simply supported plate silencer in a flow duct. Theoretical study reveals that:

1) A properly designed plate silencer can function effectively as a low-frequency wave reflector over a broad frequency band. When the mean flow effect is excluded, distinct peaks can be observed in the TL spectrum. The free vibration of the plate covering the rigid cavity is studied by neglecting the air in the duct. Comparison between the coupled plate modes and the plate response shows that the occurrence of the spectral peaks is closely related to the resonances of the plate-cavity coupling system.
2) When the effect of mean flow is considered, the peaks of the TL spectrum are smoothed out and the overall performance decreases. However, the degradation of performance is not serious for the flow speed common in a ventilation system (e.g., M=0.045). In addition, plate with a higher bending stiffness can be adopted to overcome the effect of mean flow partially.

Chapter 3

THEORETICAL STUDY ON DESIGN PARAMETERS

3.1 Introduction

In Chapter 2, a two-dimensional theoretical model has been established for a plate silencer which consists of an expansion chamber with two side-branch cavities each covered by a simply supported plate. The performance of such a device is also investigated without and with mean flow for a given design configuration. Although numerical results in Chapter 2 show that the proposed plate silencer really can function as a low frequency wave reflector, a thorough study on various design parameters is a necessary step towards a practical silencer design for reasons stated below.

One of the most important design parameters that need further study is the boundary condition of the plate. The simply supported plate described in Chapter 2, though simple to handle theoretically, is difficult to implement in practice, especially in the duct system like the one investigated in this study. It is known that the elements in the acoustic system are usually light in mass while the corresponding acoustic excitation is much weaker than the general mechanical excitation. Therefore, methods to implement the simply-supported ends in a real device often cannot guarantee that the plate can rotate freely at the simply-supported ends due to friction and other factors. In this regard, fixed ends are much easier to implement in

comparison with the simply supported ones. Hence, one step-forward is to replace the ideal simply supported boundaries by clamped ends, leading to a fixed-end plate silencer, or clamped plate silencer. Besides the boundary condition of the plate, effects of other crucial design parameters are also to be investigated. This will provide design guidelines required in the prototype development stage.

During the course of this study, it is found that when the bending stiffness and mass distribution of the clamped plate are constant along the length of the plate (a uniform plate, hereinafter), the stopband of the plate silencer turns out to be narrower than that of a simply-supported one. One qualitative explanation is that the clamped-clamped boundary condition reduces the effective radiation length of the plate when it vibrates in response to the incident sound. To release the additional restrictions caused by the clamped ends, it is proposed to use a plate with variable bending stiffness and mass distribution along the length of the plate, namely, a nonuniform plate. The problem of sound scattering of similar structures has been studied before. For example, Fernyhough and Evans (1996) compared a step approximation to an exact solution of acoustic scattering in an acoustic waveguide with non-uniform wall impedance; Grant and Lawrie (2000) studied the acoustic scattering by a duct in which the bending stiffness varies smoothly with distance along the plate. Huang (2001a) also presented a two-dimensional theoretical analysis of a membrane of varying compliance in the passive control of duct noise. As far as the current study is concerned, the employment of the nonuniform plate is mainly motivated by reducing the restrictions due to the clamped ends and thus increasing the radiation length of the plate. Hence, a non-uniform plate with two softer ends is preferred.

In what follows, the analytical formation is first extended to clamped plate silencer with uniform plate in Section 3.2. The basic procedure is the same as that for the simply supported plate silencer in Chapter 2. However, since the *in vacuo* modes of a clamped plate (a clamped beam in the two-dimensional model) are quite different from a simply-supported one, some essential expressions have to be re-formulated. The transmission loss of the clamped plate silencer with uniform plate is first examined and optimized in Sections 3.3 and 3.4. It shows that the performance of such a plate silencer is a little better than that of the drumlike silencer of the same geometric configuration but not as good as that of the simply supported plate silencer. In Section 3.5, the optimization of the nonuniform plate is conducted. Theoretical results show that, with a proper distribution of bending stiffness along the plate, the clamped nonuniform plate performs better than the simply supported plate.

3.2 Theoretical formulation

The coupled dynamics of the sound-plate interaction can be solved using the procedure described in Chapter 2. In order to avoid unnecessary duplication, the whole procedure is presented briefly, and only parts that differ from those of a simply-supported model are addressed in detail.

3.2.1 *In vacuo* mode of the clamped plate

As in the case of the simply supported plate silencer, the governing equation of the lower plate (beam) in the clamped plate silencer is,

$$B\frac{\partial^4\eta}{\partial x^4}+m\frac{\partial^2\eta}{\partial t^2}+(p_+-p_-)=0 \quad , \tag{3.1}$$

At the clamped end, the deflection and slope of the deflection curve should be zero:

$$\eta(x,t) = 0, \quad \frac{\partial \eta(x,t)}{\partial x} = 0 . \tag{3.2}$$

The general solution of a free vibration problem described by Eq. (3.1) is,

$$\eta(x) = A\sin(\beta x) + B\cos(\beta x) + C\sinh(\beta x) + D\cosh(\beta x) . \tag{3.3}$$

By invoking the boundary conditions in Eq. (3.2), the four unknown coefficients, A, B, C and D, can be determined. The solutions are available in textbooks such as (Inman, 2001), hence, only the final result is presented:

$$\varphi_j(x) = \cosh(\beta_j x) - \cos(\beta_j x) - \sigma_j[\sinh(\beta_j x) - \sin(\beta_j x)] , \tag{3.4}$$

where σ_j and β_j are given by the relationships:

$$\sigma_j = \frac{\cosh(\beta_j L) - \cos(\beta_j L)}{\sinh(\beta_j L) - \sin(\beta_j L)} ; \quad \cos(\beta_j L) \cdot \cosh(\beta_j L) = 1 . \tag{3.5}$$

In order to facilitate the formulation, the vibration mode shape defined in Eq. (3.4) is rewritten using the local dimensionless variable $\xi = (x/L + 1/2)$,

$$\varphi_j(\xi) = A_{1,j} e^{\beta_j \xi} + A_{2,j} e^{-\beta_j \xi} + A_{3,j} \sin(\beta_j \xi) + A_{4,j} \cos(\beta_j \xi) \tag{3.6}$$

where,

$$A_{1,j} = \frac{1}{2}(1 - \sigma_j) , \quad A_{2,j} = \frac{1}{2}(1 + \sigma_j) , \quad A_{3,j} = \sigma_j , \quad A_{4,j} = -1 ,$$

$$\sigma_j = \frac{\cosh(\beta_j) - \cos(\beta_j)}{\sinh(\beta_j) - \sin(\beta_j)} , \quad \cos(\beta_j) \cdot \cosh(\beta_j) = 1 . \tag{3.7}$$

Note that the mode shape functions defined in Eq. (3.6) instead of those in Eq. (3.4) are used throughout the following formulation.

3.2.2 Modal dynamics of the sound-plate interaction

To apply the standard Galerkin procedure to solve the coupled dynamics equation (3.1), the normal vibration velocity $V = i\omega\eta$ is expanded as a series of *in vacuo* modes $\varphi_j(\xi)$ with modal amplitudes V_j,

$$V = \sum_{j=1}^{\infty} V_j \varphi_j(\xi)$$

$$= \sum_{j=1}^{\infty} V_j [A_{1,j} e^{\beta_j \xi} + A_{2,j} e^{-\beta_j \xi} + A_{3,j} \sin(\beta_j \xi) + A_{4,j} \cos(\beta_j \xi)] \tag{3.8}$$

Following a similar procedure described in Chapter 2, Eq. (3.1) is transformed as,

$$L_j V_j + \int_0^1 (p_+ - p_-) \varphi_j(\xi) d\xi = 0\,, \tag{3.9}$$

where the structural operator L_j is defined as,

$$L_j = mi\omega + \frac{B}{i\omega}\left(\frac{\beta_j}{L}\right)^4,\ j=1,2,3,\ldots\,. \tag{3.10}$$

Comparing Eq. (3.9) with Eqs. (2.21) and (2.28) shows that the change of boundary conditions only changes the expressions for modal impedance Z_{lj}, including cavity impedance Z_{clj} and radiation impedance Z_{+lj}.

3.2.2.1 Cavity impedance

The cavity impedance Z_{clj} is the component of the modal impedance that contributes from the acoustic pressure inside the cavity. Following the procedure described in section 2.3.2, the component Z_{clj} is found as,

$$Z_{clj} = -\int_0^1 \varphi_l(\xi)\, p_{cav,j}(x,0)d\xi$$

$$= \sum_{r=0}^{\infty}\sum_{s=0}^{\infty} \frac{ik_0(2-\delta_{0r})(2-\delta_{0s})}{h_c(\kappa_{rs}^2 - k_0^2 + 2i\zeta_{rs}\kappa_{rs}k_0)} \int_0^1 \left[\int_0^1 \varphi_j(\xi')\cos(r\pi\xi')d\xi'\right]\cos(r\pi\xi)\varphi_l(\xi)d\xi$$

$$= \sum_{r=0}^{\infty}\sum_{s=0}^{\infty} \frac{ik_0(2-\delta_{0r})(2-\delta_{0s})}{h_c(\kappa_{rs}^2 - k_0^2 + 2i\zeta_{rs}\kappa_{rs}k_0)} I_{c,jl} \tag{3.11}$$

The double integration $I_{c,jl}$ is defined as,

$$I_{c,jl} = \int_0^1 [A_{1,j}e^{\beta_j\xi'} + A_{2,j}e^{-\beta_j\xi'} + A_{3,j}\sin(\beta_j\xi') + A_{4,j}\cos(\beta_j\xi')]\cos(r\pi\xi')d\xi'$$

$$\times \int_0^1 [A_{1,l}e^{\beta_l\xi} + A_{2,l}e^{-\beta_l\xi} + A_{3,l}\sin(\beta_l\xi) + A_{4,l}\cos(\beta_l\xi)]\cos(r\pi\xi)d\xi$$

$$= \left(\sum_{p=1}^{4} A_{p,j} I_{cj,p} \sum_{q=1}^{4} A_{q,l} I_{cl,q}\right), \tag{3.12}$$

where, the coefficients $I_{cj,p}$ ($I_{cj,1} \sim I_{cj,4}$) and $I_{cl,q}$ ($I_{cl,1} \sim I_{cl,4}$) are given in the Appendix.

3.2.2.2 Radiation impedance in the main duct

The radiation impedance matrix, $[Z_{+jl}]$, relates the plate vibration velocity to the radiation pressure in the main duct. For the jth modal vibration of unit amplitude, the radiation pressure $p_{+rad,j}$ is (see Eq. (2.37)),

$$p_{+rad,j} = i\frac{L}{2}\sum_{r=0}^{\infty} \frac{\psi_r(y)}{\sqrt{(1-M^2)(r\pi)^2 - k_0^2}} \int_0^1 \Big[H(x-x')(k_0 - M\mathrm{K}_r^+)e^{-i\mathrm{K}_r^+(x-x')}$$

$$+ H(x'-x)(k_0 + M\mathrm{K}_r^-)e^{i\mathrm{K}_r^-(x-x')}]\psi_r^*(y')F_j(\xi)d\xi \tag{3.13}$$

The velocity term $F_j(\xi)$ including the jth modal vibration of unit amplitude and the corresponding convective velocity due to mean flow:

$$F_j(\xi) = \varphi_j(\xi) - i\frac{M}{\omega}\frac{\partial \varphi_j(\xi)}{\partial x'}$$

$$= B_{1,j}e^{\beta_j \xi} + B_{2,j}e^{-\beta_j \xi} + B_{3,j}\sin(\beta_j \xi) + B_{4,j}\cos(\beta_j \xi) \tag{3.14}$$

where, $B_{1,j} \sim B_{4,j}$ are defined as,

$$B_{1,j} = \frac{1}{2}(1-\sigma_j)(1-i\frac{M\beta_j}{L\omega}), \qquad B_{2,j} = \frac{1}{2}(1+\sigma_j)(1+i\frac{M\beta_j}{L\omega}),$$

$$B_{3,j} = \sigma_j - i\frac{M\beta_j}{L\omega}, \qquad B_{4,j} = -1 - i\frac{M\beta_j\sigma_j}{L\omega}. \tag{3.15}$$

Therefore, the modal impedance Z_{+lj} that contributes from the radiation pressure in the maid duct is,

$$Z_{+lj} = \int_0^1 \varphi_l(\xi) p_{+rad,j}(x,0) d\xi \tag{3.16}$$

Substituting Eq. (3.13) into Eq. (3.16) gives,

$$Z_{+lj} = i\frac{L}{2}\sum_{r=0}^{\infty}\frac{(2-\delta_{0r})}{\sqrt{(1-M^2)(r\pi)_2 - k_0^2}} \cdot \sum_{p=1}^{4}\sum_{q=1}^{4} A_{p,l} \cdot B_{q,j} \cdot \Pi_{p,q} \tag{3.17}$$

where, $A_{1,l} \sim A_{4,l}$ and $B_{1,j} \sim B_{4,j}$ are coefficients defined in Eqs. (3.7) and (3.15); the results for the double integrations, $\Pi_{1,1} \sim \Pi_{4,4}$ are also given in the Appendix.

With the modal impedance due to p_{+rad} and p_{cav} found, the dynamics Eq. (3.1) is again cast as a truncated set of linear equations for the vibration amplitude V_j, as

shown in Eq. (2.52), which is then solved via matrix inversion. Note that the modal coefficient of the incident wave I_j is now defined as,

$$\mathrm{I}_j = \int_0^1 p_i \varphi_j(\xi) d\xi = e^{i\mathrm{K}_0^+ L/2} \sum_{p=1}^{4} A_{p,j} \cdot I_{in,p}, \tag{3.18}$$

which is different from that for the simply supported plate in Eq. (2.54). The integration results for $I_{in,1} \sim I_{in,4}$ can be found in the Appendix. The reflected sound wave, transmitted sound wave, as well as the transmission loss of the plate silencer can be found in a similar way as shown from Eq. (2.56) to Eq. (2.62) so that the detailed process is not repeated.

3.3 Performance analysis

The silencing performance of the clamped plate silencer is optimized and compared with the simply-supported plate silencer as well as the drumlike silencer (Huang, 2002). For given geometric configuration and mass ratio, the so-called optimization is realized by searching for the optimal bending stiffness B_{opt} that would yield a *TL* higher than a certain criterion value over the widest possible continuous frequency band $f \in [f_1, f_2]$. The ratio f_2 / f_1, which can be considered as the logarithmic bandwidth of the silencer, is chosen as the objective function to be maximized in the optimization exercise. The motivation behind using such a bandwidth definition is the desire to put due emphasis on the low-frequency performance. The criterion value TL_{cr} is chosen as the peak TL for an expansion chamber with the added volume which is three times the actual volume used by the plate silencer. For a total cavity volume of Λ=10, this value can be calculated and

rounded up to 10 dB. The default cavity shape is chosen as $L = 5$ and $h_c = 1$, which is the same as the simply supported plate silencer in Chapter 2. Following the above optimization procedure, the following parameters are obtained for *m*=1:

$$B_{opt} = 0.07, \quad f_1 = 0.0445, \quad f_2 = 0.125. \tag{3.19}$$

The corresponding silencing performance is compared with the drumlike silencer and simply supported plate silencer in Figures 3.1 and 3.2. Since the performances of all the three silencers are optimized following the same procedure, the comparisons among them are meaningful.

Figure.3.1 compares the TL spectrum of the clamped plate silencer (solid line) with the drumlike silencer (dashed line) of the same cavity configuration and mass ratio. The lower and upper bandwidth limits of the plate silencer are $f_1 = 0.0445$, and $f_2 = 0.125$, with the ratio being $f_2 / f_1 = 2.8$. For the drumlike silencer, the lower, upper bandwidth limits and bandwidth are $f_1 = 0.054$, $f_2 = 0.141$, and $f_2 / f_1 = 2.6$. Clearly, with the same configuration, the optimal performance of the clamped plate silencer is better than that of the drumlike silencer in terms of both the lower band limit and the achievable bandwidth. Figure 3.2 compares the TL spectrum of the clamped plate silencer and the simply supported silencer. As the boundary condition of the plate changes from “simply-supported” to “clamped”, the stopband of the plate silencer shrinks and the lower limit is pushed to higher frequency. This change is undesirable for the clamped plate silencer because good performance is expected in relatively low frequency region.

The performance degradation of the clamped plate silencer may be attributed to the clamped boundary conditions applied to the leading and trailing edges of the plate.

Such a boundary condition brings additional restrictions to portions of the plate near the ends, which in turn prevents the plate from vibrating and radiating reflection sound effectively. Therefore, a nonuniform plate with softer ends may be adopted to further increase the stopband and reduce the lower band limit, as studied in Section 3.5.

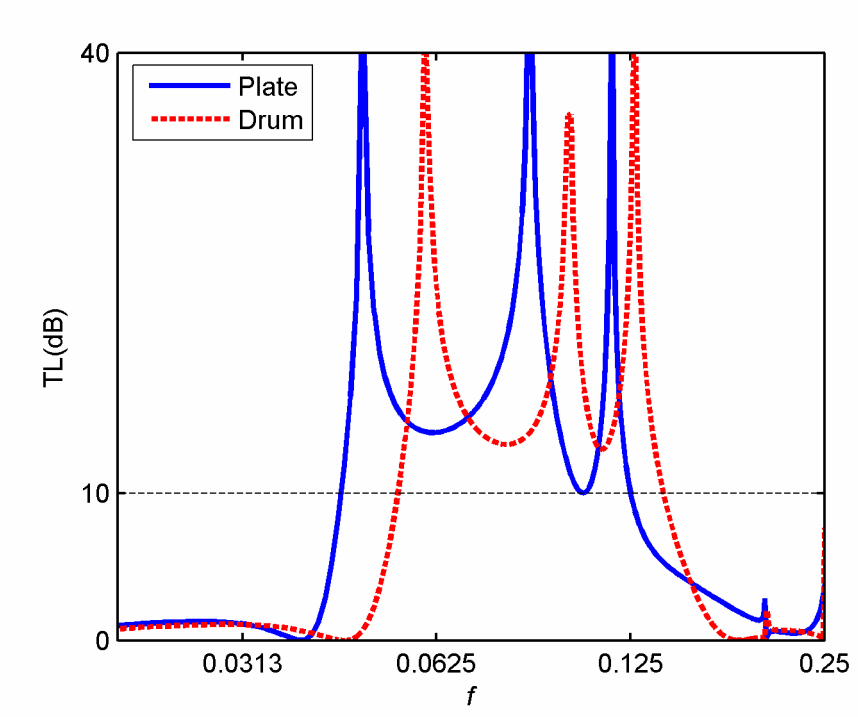

Figure 3.1: TL comparison of the clamped plate silencer (solid line, with B=0.07) with drumlike silencer (dashed line, with T=0.475) with the same cavity geometry of L=5h, h_c=h, and the same mass ratio of m=1.

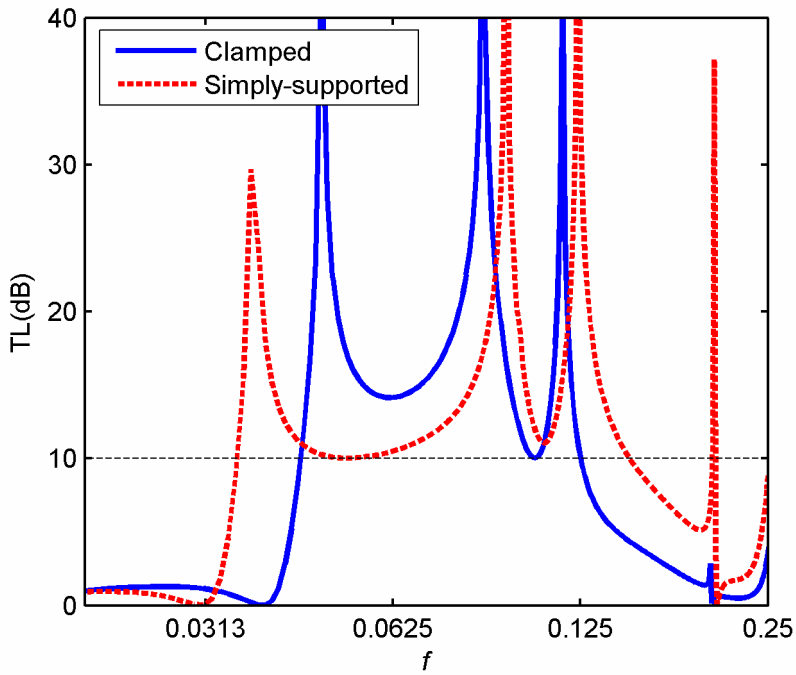

Figure 3.2: TL comparison of the clamped plate silencer (solid line, with B=0.07) with the simply supported silencer (dashed line, with B=0.129) with the same cavity geometry of L=5h, h_c=h, and the same mass ratio of m=1.

3.4 Effect of various design parameters

Although the plate silencer can be a very simple device for construction, it does have a lot of variables which affect its silencing performance greatly, for instance, the cavity shape, the plate properties, and so on. As guidelines for the plate silencer design, the effect of various design parameters are identified with other design parameters fixed.

3.4.1 Cavity shape

The hard-walled cavity serves to prevent the break-out noise. Meanwhile, it also introduces cavity air stiffness to the system which may reduce the plate silencer effectiveness, especially at relatively low frequency. Aiming for the widest stopband with a given volume of $\Lambda = Lh_c$, an optimization study of the cavity parameters has been carried out for the drumlike silencer design (Huang, 2004). For the similarity of configurations between the drumlike silencer and the plate silencer, most of the findings for the drumlike silencer also apply to the plate silencer. Briefly, for given cavity volume, shallower cavity with longer plate has wider TL spectrum. The frequency interval between spectral peaks increase and, as a result, the dip between adjacent peaks falls down. On the other hand, deeper and shorter cavity works in a narrow frequency band with better minimal TL. By choosing the criterion level TL_{cr} =10 dB and cost function as f_2 / f_1, the optimal cavity shape for the specific volume of $Lh_c = 5h^2$ was found to be $L_{opt} = 5h$ (Huang, 2006) for a simply supported plate silencer. If the boundary condition is changed from simply supported to clamped, the optimal shape changes slightly but the overall observations remain the same.

3.4.2 Plate mass

The effect of plate mass is investigated by varying the plate-to-air mass ratio *m* while the geometry is fixed as $L = 5h$ and $h_c = h$. For each mass ratio given, bending stiffness is varied to search for the optimal bandwidth f_2 / f_1. Figures 3.3(a) and 3.3(b) show the optimal bandwidth f_2 / f_1 and the optimal bending stiffness B_{opt} as

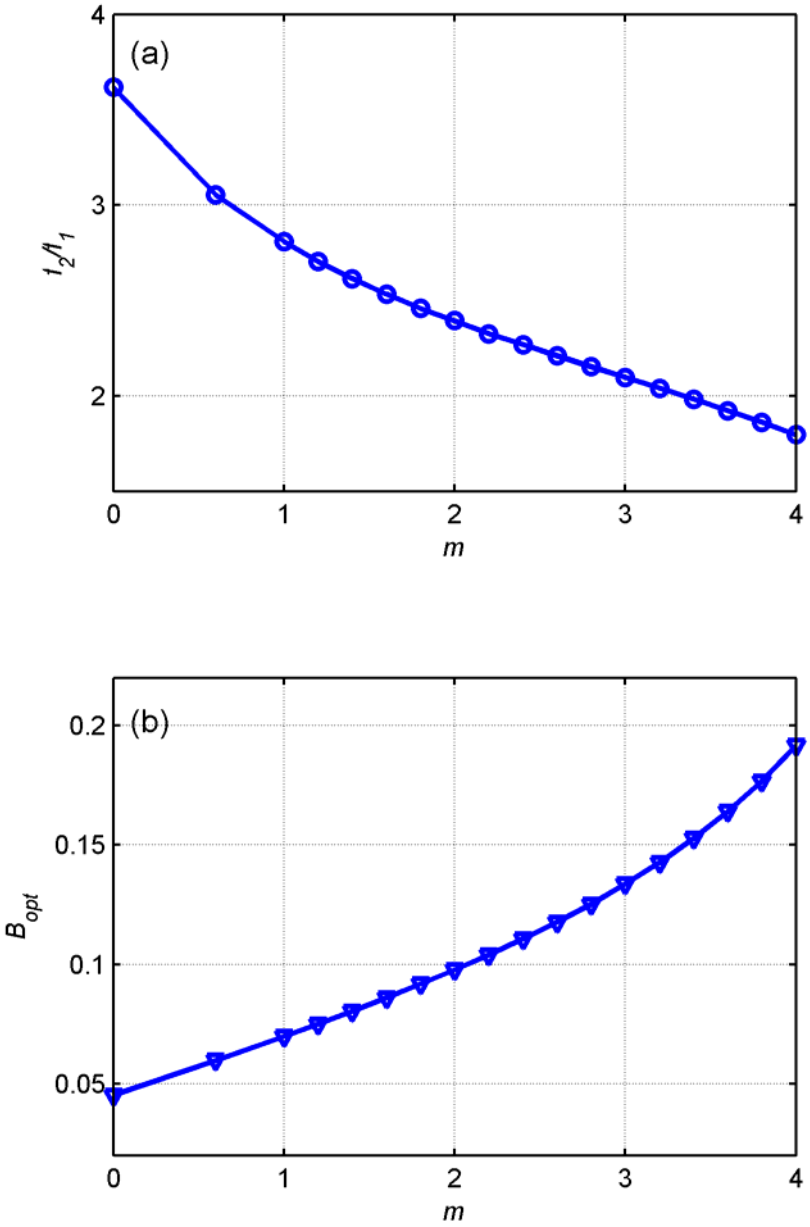

Figure 3.3: Variation of the optimal performance of the clamped plate silencer with respect to the mass ratio *m*. (a) Bandwidth f_2/f_1. (b) Required optimal bending stiffness. The cavity geometry is $L=5h$ and $h_c=h$.

functions of mass ratio *m*. As shown in Figure 3.3(a), as the plate mass increases, the maximum achievable bandwidth f_2 / f_1 decreases gradually. This effect is undesirable since our goal is to develop a broadband low frequency silencer. Nevertheless, when the mass ratio *m* reaches 3, the maximum bandwidth is 2.1, which is still larger than one octave. As the plate mass increases, the optimal bending stiffness increases too, as shown in Figure 3.3(b). This effect is also undesirable because it is usually difficult to satisfy the requirement for plate bending stiffness in the silencer design, as studied in Chapter 4. As a summary, the effect of plate mass is generally counterproductive. As the mass ratio *m* increases, the maximum achievable bandwidth decreases, while the required bending stiffness increase.

3.4.3 Plate bending stiffness

Figure 3.4 shows the variation of TL spectrum with respect to five different values of *B*. The mass ratio is fixed at m =1, and the cavity geometry is L =5 and h_c =1. Three spectral peaks can be observed for all the five cases in the frequency range of interest. However, when the bending stiffness is insufficient, dips between the spectral peaks are so pronounced that the silencer works effectively only at the discrete resonant frequencies, as shown in Figure 3.4(a). With the bending stiffness increases, the trough between the first and second spectral peaks is first lifted above the criterion level 10 dB, and then the trough between the second and third peaks is also lifted up, which warrants good performance of the silencer over a broad frequency range instead of only at the spectral peaks. Hence, the bending stiffness should be high enough in order to achieve a broad stopband.

Figure 3.4(d) shows the optimal TL spectrum with the optimal bending stiffness B_{opt} =0.07. Generally speaking, a three-peak stopband shown in Figure 3.4(d) is wider than a two-peak stopband in Figure 3.4(c). However, since the low frequency noise (say, f <0.08) is of the most interest, the two-peak stopband spectrum shown

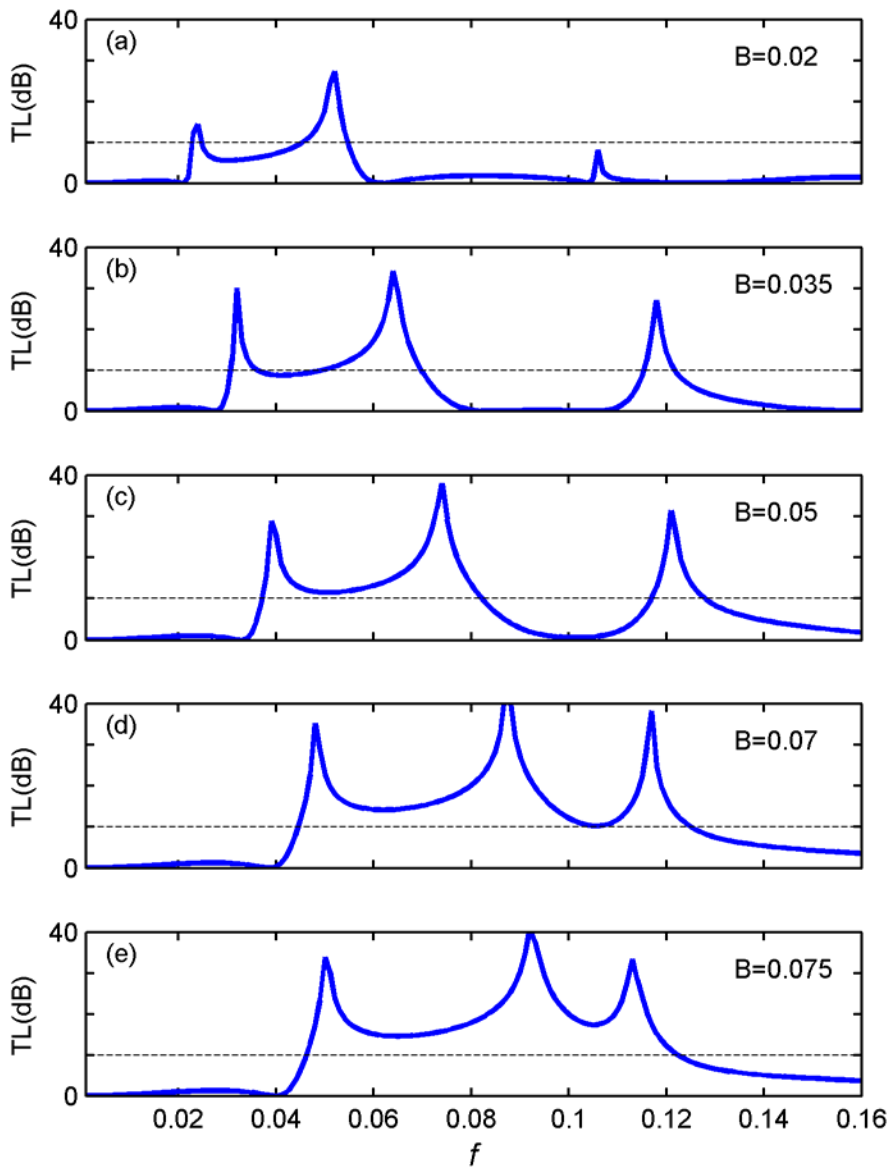

Figure 3.4: Variation of TL spectrum with respect to the plate bending stiffness B. The mass ratio is fixed at m =1, and the cavity geometry is L =5 and h_c =h.

in Figure 3.4(c) may also be chosen as a practical silencer design. Higher bending stiffness may further increase the TL between the spectral peaks, however, because of the shift of the resonant frequencies, the whole stopband shifts towards higher frequencies and the bandwidth shrinks, as shown in Figure 3.4(e).

Combining Figures 3.3 and 3.4, we can conclude that a good plate silencer requires light but extremely stiff plate. However, such a requirement is usually out of the reach of existing homogenous materials. Take three typical engineering materials for example. The first material is the aluminium alloy with density ρ_s^*=2700 kg/m^3, and Young's modulus E^*=70 GPa. The second material is PVC foam with density ρ_s^*=60 kg/m^3, and Young's modulus E^*=100 MPa. The third material is balsawood with density ρ_s^*=150 kg/m^3, and Young's modulus E^*=3 GPa. The density and Young's modulus data for the three materials are a set of moderate values taken from Chart 1 of Ashby and Johnson (2002). Assuming three homogeneous plates of rectangular cross section are made of the three materials respectively, their dimensionless bending stiffness can be calculated as:

$$B = \frac{m^3 E}{12\rho_s^3}, \tag{3.20}$$

where m is the mass ratio; E is the dimensionless Young's modulus and ρ_s is the dimensionless density. The results for m=1 and 3 are shown in Table 3.1. As the required optimal bending stiffness is B=0.07 and 0.133 for the two mass ratios (see Figure 3.3(b)), all of the three materials are far below the requirement of the plate silencer. At the same time, Eq. (3.20) implies that the achievable bending stiffness solely depends on the plate-to-air mass ratio provided that material property is given.

Therefore, an effective way of constructing weight-saving materials must be taken to realize a broadband plate silencer experimentally, and this issue is addressed in Chapter 4.

Table 3.1 Dimensionless bending stiffness for plates made of different materials

Material	Aluminium		PVC Foam		Balsawood	
Mass ratio, *m*	1	3	1	3	1	3
Bending stiffness, *B*	3.8×10^{-6}	1.0×10^{-4}	5.0×10^{-4}	0.014	9.6×10^{-4}	0.026

3.4.4 Acoustic leakage

In the two-dimensional theoretical model established, the plate, the duct and the cavity are assumed to be of the same width *D*, while the plate covers the backing cavity completely. In real application, however, a small gap is necessary between the lateral edges of the plate and the duct walls so that the two lateral edges of the plate can move freely, as shown in Figure 3.5. The gap may lead to acoustic leakage from the duct to the backing cavity almost inevitably. As the acoustic leakage changes the acoustic loading across the plate, it tends to decrease the plate vibration level and to reduce the sound reflection capability of the plate silencer. In the worst case, the acoustic leakage may render the plate silencer totally ineffective and the whole device just functions as an expansion chamber.

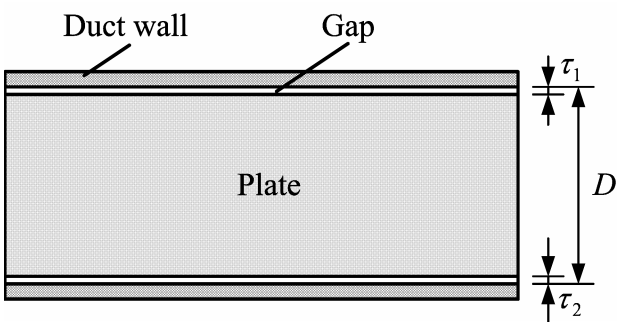

Figure 3.5: Schematic of the gaps between the plate and the duct walls. The width of the duct is D, and the gaps are τ_1 and τ_2, respectively.

To investigate the effect of the gaps shown in Figure 3.5 on the silencing performance of the plate silencer, a three-dimensional finite element model based on Femlab® can be employed. Features on the software package Femlab® and details on the modelling procedure will be given in Chapter 5. Here, only the simulation results are presented. To simplify the investigation, the width of the duct is assumed to be unity and the widths of the two gaps are assumed to be equal, that is, D=1, $\tau_1 = \tau_2 = \tau$. Other parameters for the plate silencer are given as below:

$$L=5,\ \ h_c=1,\ \ m=1,\ \ B=0.07. \tag{3.21}$$

The variation of the TL spectrum of the plate silencer with respect to the gap width τ is shown in Figure 3.6. It can be observed that the effect of noise leakage is negligible as long as the gap is narrower than a certain level, for example, $\tau \leq 0.005$. As the gap increases to τ =0.01 or wider, the TL spectrum of the plate silencer changes obviously, indicating significant acoustic leakage from the duct to the backing cavity. The validation experiment in Chapter 4 confirms that a plate silencer with $\tau \leq 0.005$ matches the two-dimensional theoretical modelling well.

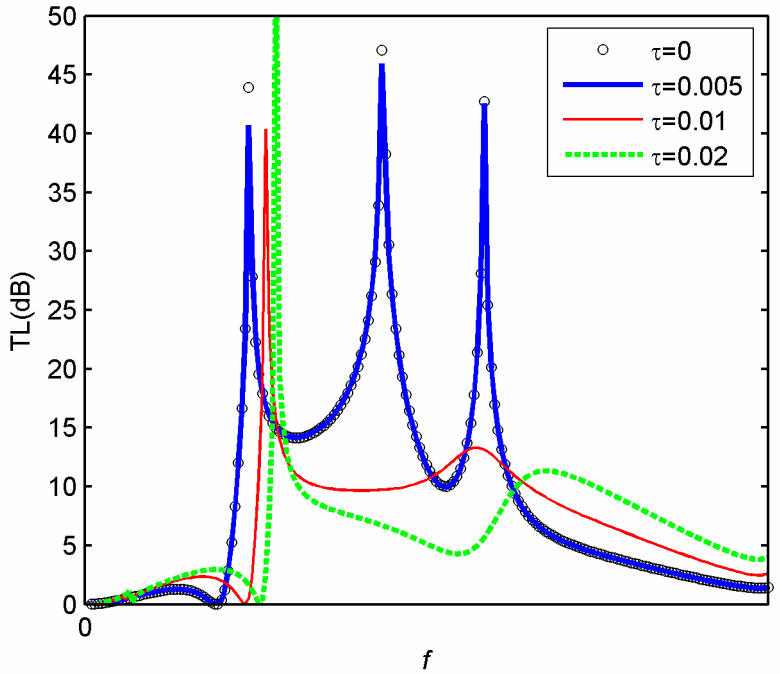

Figure 3.6: Variation of TL spectra with respect to the gap width τ .

3.5 Nonuniform plate

3.5.1 Method of solution

For the nonuniform plate, the bending stiffness *B* and mass ratio *m* are functions of the coordinate along the plate, that is, *x*. Therefore, the dynamic Eq. (3.1) for the uniform plate is rewritten as,

$$\frac{\partial^2}{\partial x^2}\left(B(x)\frac{\partial^2 \eta}{\partial x^2}\right) + m(x)\cdot\frac{\partial^2 \eta}{\partial t^2} + (p_+ - p_-) = 0\,. \tag{3.22}$$

For harmonic vibration, by introducing the plate normal vibration velocity $V = \partial\eta/\partial t = i\omega\eta$, Eq. (3.22) becomes,

$$\frac{1}{i\omega}\left[\frac{\partial^2}{\partial x^2}\left(B(x)\cdot\frac{\partial^2 V}{\partial x^2}\right)\right]+m(x)i\omega\cdot V+(p_+-p_-)=0 \tag{3.23}$$

The above equation can also be solved using the standard Galerkin procedure similar to that employed to Eq. (3.1). The difference is that the structural operator $\{L_j\}$ defined in Eq. (3.10) is now replaced by a dynamic matrix $[L_{jl}]$. The normal velocity V is also expanded as a series of *in vacuo* modes $\varphi_j(\xi)$ which are defined in Eq. (3.4)

$$V=\sum_{j=1}^{\infty}V_j\varphi_j(\xi) \tag{3.24}$$

Suppose the jth and l^{th} vibration mode shape of the clamped-clamped plate (beam) are $\varphi_j(\xi)$ and $\varphi_l(\xi)$ respectively. Following the procedure described by Eqs. (2.22)-(2.24), the dynamic Eq. (3.23) is transformed to,

$$\sum_{l=1}^{N}V_l(L_{jl}+Z_{jl})=-\mathrm{I}_j\,, \tag{3.25}$$

where Z_{jl} is the acoustic impedance found in Eqs. (3.11) and (3.17).The dynamic matrix $[L_{jl}]$is found as,

$$L_{jl}=\int_0^1\left\{\frac{1}{i\omega}\frac{1}{L^4}\left[B(\xi)\varphi_l^{(4)}(\xi)+2B^{(1)}(\xi)\varphi_l^{(3)}(\xi)+B^{(2)}(\xi)\varphi_l^{(2)}(\xi)\right]\right.$$

$$\left.+i\omega m(\xi)\varphi_l(\xi)\right\}\varphi_j(\xi)d\xi\,. \tag{3.26}$$

With the structural operator $\{L_j\}$ defined in Eq. (3.10) is substituted by the above dynamic matrix $[L_{jl}]$, the dynamic equation (3.23) for the nonuniform plate can be solved, and the TL can be calculated following the same procedure as that for the uniform plate.

3.4.2 Optimization of $B(x)$

The so-called optimization of nonuniform distribution $B(x)$ is realized by choosing one shape from a set of possibilities that can yield the widest stop-band. When constructing $B(x)$, the following two factors are taken into considerations. First, the purpose of introducing the non-uniform plate is to release the restriction near the clamped ends; therefore, the bending stiffness near the two ends should be smaller than that in the middle. Second, the lower vibration modes (especially the first two modes) of the plate are dominant in the reflection of sound. Based on the above two considerations, it is appropriate to construct $B(x)$ as,

$$B(x) = B_0 \cdot d(x)\,, \tag{3.27}$$

where B_0 is a constant ratio to be determined, and $d(x)$ is the shape function of the bending stiffness. One such distribution is shown in Figure 3.7(a) and is described below,

$$d(\xi) = \begin{cases} h_1 + \dfrac{\arctan(\alpha_1\xi_1) + \arctan[\alpha_1(\xi - \xi_1)]}{\arctan(\alpha_1\xi_1) + \arctan[\alpha_1(\xi_0 - \xi_1)]} \cdot (1 - h_1), & 0 < \xi \le \xi_0, \\ h_2 + \dfrac{\arctan[\alpha_2(1-\xi_2)] - \arctan[\alpha_2(\xi - \xi_2)]}{\arctan[\alpha_2(1-\xi_2)] - \arctan[\alpha_2(\xi_0 - \xi_2)]}(1 - h_2), & \xi_0 < \xi < 1, \end{cases} \tag{3.28}$$

where $\xi = (x/L + 1/2)$ is as defined before. There are seven control parameters in the above defined function $d(\xi)$, namely, $\alpha_1, \alpha_2, h_1, h_2, x_0, \xi_1$ and ξ_2, where α_1, α_2 control the slope of the resulting curve; h_1, h_2 control the heights of the curve at the two ends; x_0, x_1 and x_2 control the horizontal positions of the two segments. Since bending stiffness, $B(x)$, plays a more important role in the dynamics of the plate than the mass ratio $m(x)$ does, the distribution of, $m(x)$, is simply taken as,

$$m(x) = m_0 \cdot \sqrt[3]{d(x)} \ . \tag{3.29}$$

The cavity geometry is still assumed to be $h_c = 1$ and $L = 5$. The range of the seven controlling parameters in Eq. (3.28) are, $h_1, h_2 \in [0.0001, 0.2]$, $\alpha_1, \alpha_2 \in [1, 1500]$, $\xi_0 \in [0.3, 0.6]$, $\xi_1 \in [0.05, 0.25]$ and $\xi_2 \in [0.75, 0.95]$. During the optimization, the seven parameters vary step by step within the ranges given above. The TL is calculated for each given set of parameters, and the set of parameters that results in the widest stopband is chosen as the optimal one. The corresponding $B(x)$ is then chosen as the optimal distribution of the bending stiffness. In order to facilitate the comparison of the transmission loss spectrum for each $B(x)$, the total mass along the plate is kept as a constant during the optimization exercise,

$$\int_0^L m(x)dx = \overline{m} \cdot L \, , \tag{3.30}$$

where $\overline{m}$ =1 is chosen in the example given. For the nonuniform plate, $\overline{m}$ is the average mass ratio along the length of the plate. The maximum stopband $f \in [0.0343, 0.2062]$ is found with the following parameters

$$\xi_0 = 0.35, \quad \xi_1 = 0.2, \quad \xi_2 = 0.815, \quad \alpha_1 = 300, \quad \alpha_2 = 100, \quad h_1 = h_2 = 0.01 . \tag{3.31}$$

The constant B_0 is determined as 0.4935. The results of the optimization are shown in Figure 3.7.

Figure 3.7(a) gives the optimal distribution of the bending stiffness along the length of the plate. Parameters h_1 and h_2 represent the relative bending stiffness at the two edges, and both of them equal to 0.01 in this case. As expected, the two ends of the plate are much softer than the portion in the middle and the additional restriction due to the clamped boundary condition is thus released. The length of the thick

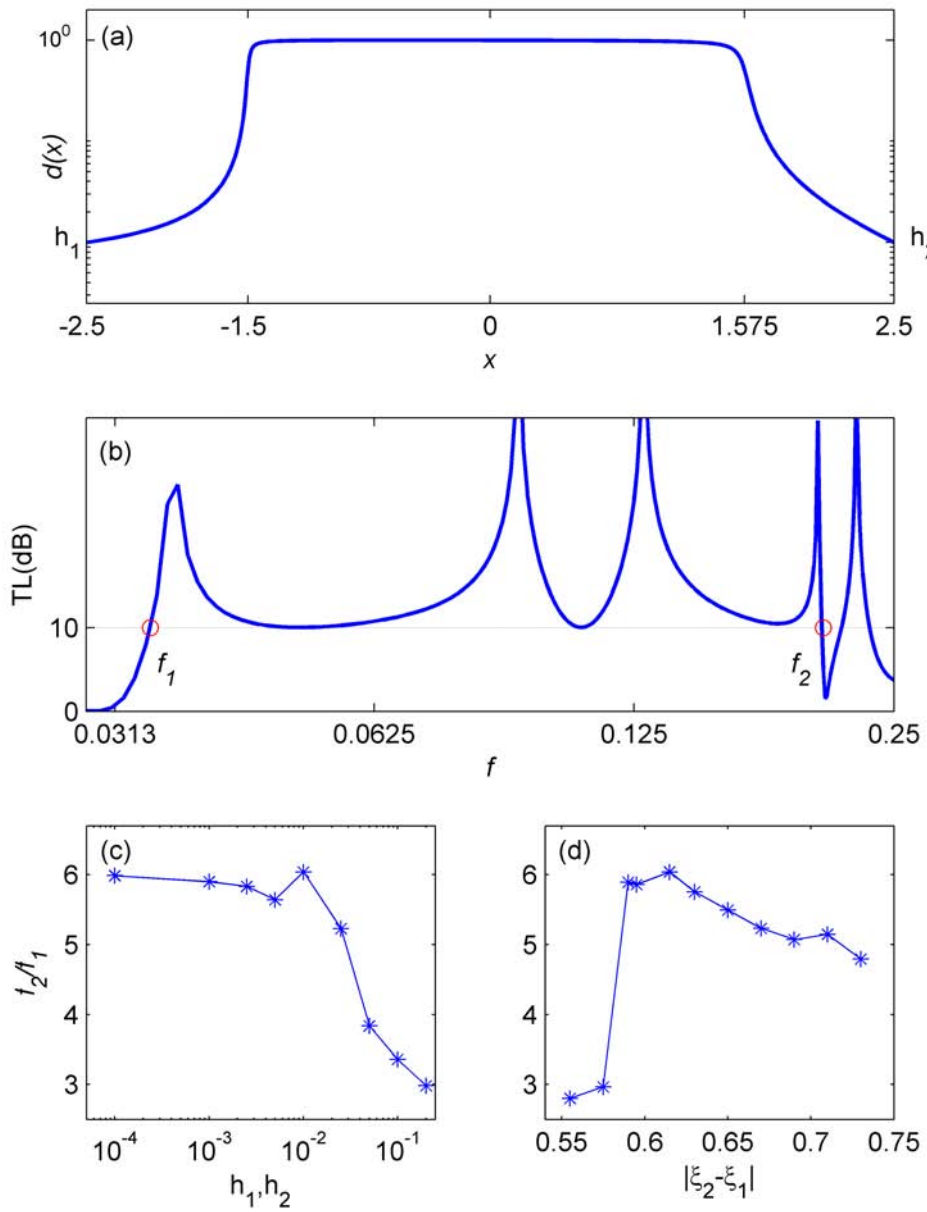

Figure 3.7: Optimization of the non-uniform plate. (a) Optimal distribution of the bending stiffness along the length of the plate. (b) TL. (c) Bandwidth f_2 / f_1 with respect to the relative bending stiffness at the two thin ends. (d) Bandwidth f_2 / f_1 with respect to the length of the thick part of the plate. The cavity geometry is $L = 5h$, $h_c = h$; average mass ratio $\overline{m}$ =1.

portion in the middle can be roughly characterized by the value of $|\xi_2 - \xi_1|$, which is 0.615 in this case. Suppose that the plate material is homogeneous. Such a distribution can be realised approximately by making the thickness of the plate into the shape of $\sqrt[3]{d(x)}$. Figure 3.7(b) shows the overall TL using a logarithmic scale. The stopband begins from f_1=0.0343 and ends at f_2=0.2063, with the bandwidth being f_2 / f_1=6.02. Four peaks can be observed in the stopband. Figure 3.7(c) shows the maximum bandwidth as a function of h_1 and h_2. Here, values of other parameters given in (3.31) are used. A softer end can help reduce the restriction due to the clamped condition. However, it does not follow that the softer the two ends are, the better the performance is. As shown in Figure 3.7(c), when h_1, h_2 =0.01, the bandwidth reaches the maximum of 6.02. Further decrease in h_1 and h_2 does not make any noticeable improvement of the bandwidth. Figure 3.7(d) shows the bandwidth f_2 / f_1 as a function of the length of the thick portion, $|\xi_2 - \xi_1|$, while other parameters are kept as the optimal values given in (3.31). As $|\xi_2 - \xi_1|$ decreases from the optimal point, the performance drops and approaches the behaviour of a uniform plate.

Figure 3.8 compares the vibration velocity distribution $V(x)$ between the clamped non-uniform plate (solid lines) and a simply-supported plate (dashed lines) at f=0.037 (at the first peak) and f=0.2 (near the fourth peak). The real parts are shown in Figures 3.8(a) and 3.8(b). Since the plate vibrations are almost in-phase over the entire length, the imaginary parts of $V(x)$ shown in Figures 3.8(c) and 3.8(d) are nearly zero. As expected, the clamped plate with softer ends responds in a similar way to the simply-supported plate, but the peaks and troughs are much closer to the

clamped ends. The effect of this difference is as follows. The plate vibration is dominated by a mode shape which is close to a dipole-like pattern of sound radiation. Much of the sound radiated by the leading edge portion of the plate with $V(x)>0$, cf. Figure 3.8(a), is cancelled by that from the trailing edge portion where $V(x)<0$. When $f \to 0$, this cancellation would be rather complete since the plate length is negligible compared with the wavelength of sound in air. The length between the peaks and troughs in Figures 3.8(a) and 3.8(b) thus determines the radiation

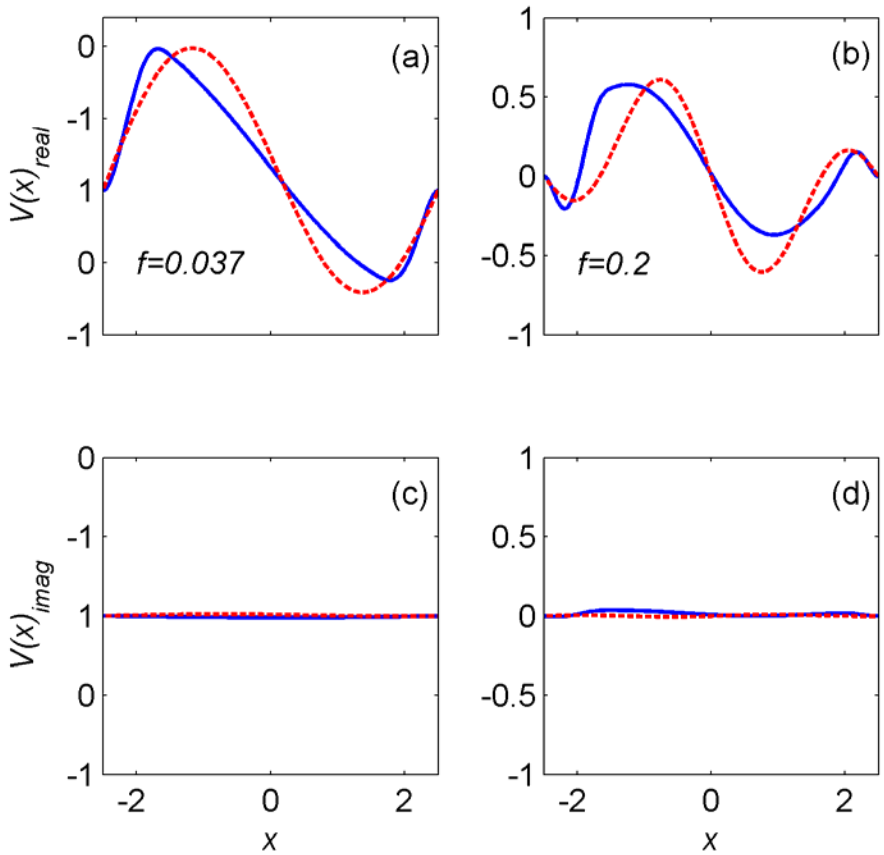

Figure 3.8: Comparison of the vibration velocity distribution $V(x)$ between the clamped nonuniform plate (solid lines) and the simply supported plate (dashed lines). (a) $f = 0.037$, real parts. (b) $f = 0.2$, real parts. (c) $f = 0.037$, imaginary pars. (d) $f = 0.2$, imaginary parts.

efficiency of the plate for a finite frequency. In other words, a clamped plate with much of the length behaving like a rigid plate has a higher capability to reflect sound, in a dipole-like mode which is not prohibited by the cavity stiffness.

The performance of the nonuniform clamped plate silencer with that of the simply supported plate silencer is compared and shown in Figure 3.9. The cavity geometry and the mass ratio of the two silencers are the same, namely, $L = 5$, h_c =1,and $\overline{m}$ =1. The optimal bending stiffness B_{opt} for the simply supported plate is 0.129 (see Chapter 2). The results for the nonuniform plate silencer are shown in solid lines and those for the simply-supported plate silencer are shown in dashed lines. Figure 3.9(1a) compares the TL spectra of the two silencers. P1 through P4 correspond the four peak positions of the nonuniform clamped plate silencer. As shown in Figure 3.9(1a), the performance of the clamped nonuniform plate silencer can be even better than the simply supported uniform plates. The difference mainly comes from the relatively high frequency region, namely, from P3 to P4. Figures 3.9(2a) and 3.9(3a) compare the decomposition of the reflected sound, cf. Eq. (2.61) into the summation over odd *in vacuo* modes, *j*=1,3,5,… and that over the even *in vacuo* modes, *j*=2,4,6,….Denoting the phase angle between the reflected sound wave from the odd modes and that from the even modes by θ, an odd-even modal interference index can be defined as $\cos\theta$, which varies from the lowest extreme of complete cancellation ($\cos\theta = -1$)to complete addition ($\cos\theta = 1$). From P1 to P3, the reflected sound and the odd-even modal interference indexes of the two types of silencers are almost identical, resulting in similar TL spectra. From P3 to P4, the reflected sound waves for the clamped nonuniform plate are slightly stronger than those for the simply supported plate. At the same time, the clamped nonuniform plate

silencer has a higher odd-even interference index, which indicates that less sound wave cancellation occurs at this frequency region. As a result, the clamped nonuniform plate silencer demonstrates higher TL than the simply supported plate silencer from P3 to P4.

The second and third columns of Figure 3.9 compare the modal amplitude, $|V_j|$, modal reflection coefficient, $|R_j|$, the single mode reflection $|V_j R_j|$ and the modal contribution γ_j of the first two modes. Here, R_j is the complex amplitude of the reflected sound by the induced vibration of the jth vibration mode with unit amplitude. To facilitate the comparison, the vibration mode of a simply-supported plate, $\sin(j\pi\xi)$, is used for both silencers. Hence, the expression for R_j given in Eq. (2.62) applies. The γ_j represents the contribution of each single mode, denoted as $V_j R_j$, towards the total reflected sound p_r.When non-uniform plate is used, both the contribution γ_1 and γ_2 near the first peak point P1 are pushed to further lower frequency, which results in a smaller lower bound f_1 . The high TL between the third peak point P3 and the upper bound f_2 are mainly due to the increased modal amplitude $|V_2|$, the modal reflection $|V_2 R_2|$ and the corresponding modal reflection contribution γ_2, as shown in Figures 3.9(4b)-(4c). Therefore, compared with the uniform plate, a properly designed non-uniform plate can greatly enhance the performance of the clamped plate silencer.

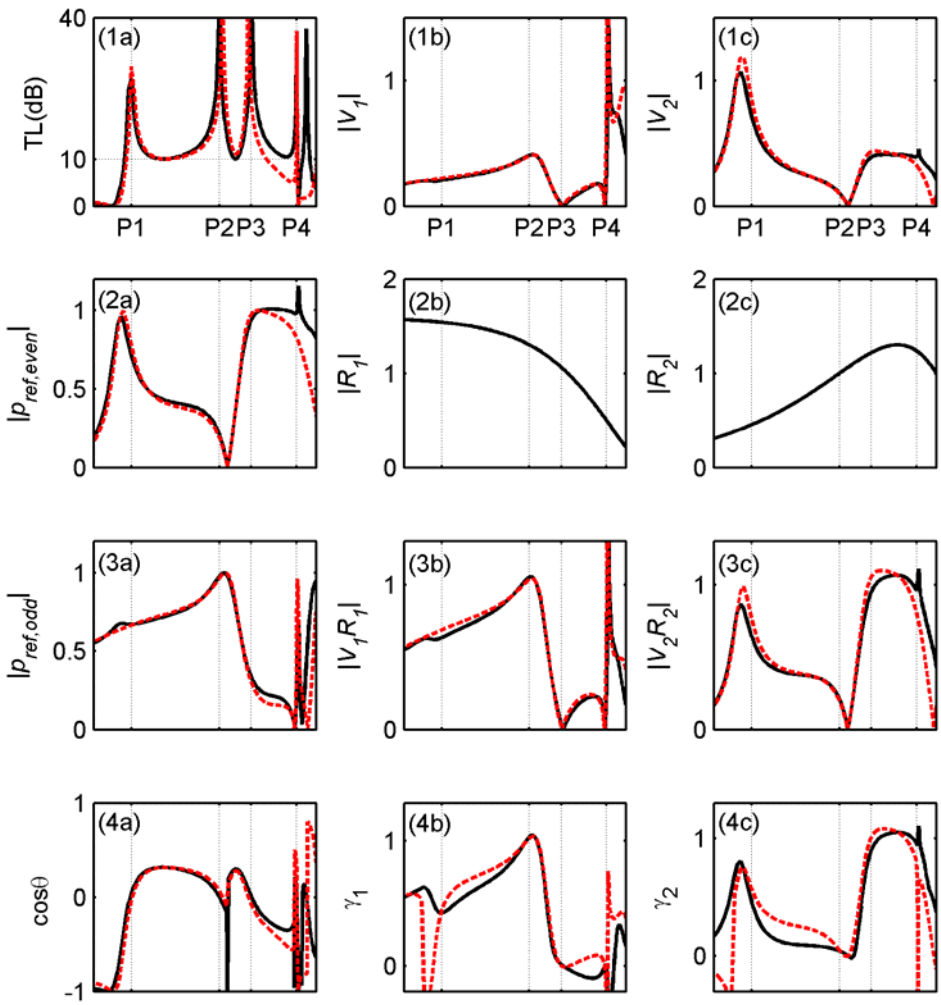

Figure 3.9: Comparison of the clamped nonuniform plate (solid lines) with the simply supported uniform plate (dashed lines). The cavity geometry is of $L = 5h$, $h_c = h$, and $\overline{m}$ =1. (1a) TL. (2a) Sound reflected by the even modes. (3a) Sound reflected by the odd modes. (4a) Odd-even modal interference index. The second and third columns compare the modal amplitude, $|V_j|$, the modal reflection coefficient, $|R_j|$, the single mode reflection, $|V_j R_j|$, and the modal contribution γ_j of the two plate silencers. The four peak positions are identified in all the subfigures.

3.6 Summary

Theoretical formulation is extended to the boundary condition of clamped plate, which is easier to implement than the simply supported one in practice. Theoretical study reveals that such a device can also function as a low frequency wave reflector over a broad frequency band. The silencing performance of the plate silencer is subject to various design parameters, especially the plate properties such as the plate mass and the bending stiffness. It is found that a good plate silencer design requires a light but extremely stiff plate, which is usually hard to satisfy with existing homogeneous materials.

Compared with the simply supported plate silencer, the optimal stopband shrinks and the lower band limit increases with the plate clamped at the leading and trailing edges. One qualitative explanation is that the clamped boundary condition reduces the effective radiation length of the plate when it vibrates in response to the incident sound. Further numerical study shows that the performance of the clamped plate silencer can be enhanced by adopting nonuniform plates with softer ends. Optimization study shows that, with a proper distribution of the bending stiffness along the plate, the widest stopand of the clamed plate silencer may be up to f_2/f_1 =6.0 for a mass ratio of m=1, which is even wider than that of a simply supported plate silencer.

The mechanism for the performance improvement by adopting nonuniform plates is explored. When excited by the incident wave, the clamped nonuniform plate responds in a similar way to the simply-supported plate, but the displacement peaks and troughs are much closer to the clamped ends. The extended length between the peaks and troughs makes the nonuniform plate more capable of reflecting sound in a

dipole-like mode, which is not prohibited by the cavity stiffness. Comparison of the modal reflections between the clamped nonuniform plate and the simply-supported plate shows that the second *in vacuo* plate vibration mode contributes most to the expansion of stopband of the nonuniform plate silencer, especially in the high frequency region, which, to some extent, conforms to the above explanation.

Chapter 4

EXPERIMENTAL VALIDATION AND PERFORMANCE ASSESMENT OF PROTOTYPE SILENCER

4.1 Introduction

One purpose of the experimental study is to validate the two-dimensional theoretical model established in Chapters 2 and 3. In doing so, the silencing performance of a prototype clamped plate silencer is tested experimentally using balsawood plates. To facilitate the validation, a number of issues that might complicate the task are put aside at this stage. One of these issues is the modelling of the dynamics of a plate of non-uniform bending stiffness and the actual preparation of such bending stiffness distribution for a thin plate. Therefore, the validation experiment is limited to the test of a uniform plate with homogeneous materials. The issue of structural damping is another difficult one, but it cannot be avoided altogether. An attempt is made to simulate the damping effect towards the end of the validation experiment.

Theoretical studies show that a good plate silencer requires very light but extremely stiff plates, irrespective of the plate boundaries. Such a condition is generally difficult to satisfy with existing homogeneous plate. Although the balsawood used in the validation experiment is one of the best materials for this purpose according to Chart 1 given in (Ashby and Johnson, 2002), it is still too heavy and soft for the plate silencer. Hence, the prototype device using balsawood only

works in a relatively narrow frequency range with the overall stopband shifted to higher frequencies. As a step forward to a broadband plate silencer, we explored the feasibility of using sandwich construction to satisfy the requirement for the plate properties.

The sandwich plate combines high bending stiffness with low weight, making it a preferable choice for the design of plate silencer. However, the sandwich construction also makes the theoretical modelling more complex. Therefore, whilst pursuing of objective of realizing the said silencer using sandwich plates, we also explored the possibility of providing simplified simulation model to guide the practical design of the silencers. This study shows that, as far as low frequency is concerned, it is possible to predict the silencing performance of the sandwich plate silencer based on a simplified homogeneous plate model. Experimental results and theoretical prediction are found to be in fair agreement.

4.2 Experimental rig

The TL of the plate silencer is measured through a four-microphone, two-load method similar to the one described by Munjal and Doige (1990), as shown in Figure 4.1. The incident noise is provided by a loudspeaker connected to the duct through a contraction cone. The output signal from the DA converter (NI. PCI-M10-16E-1) is passed to the loudspeaker via a B&K power amplifier (LAB gruppen 300). Two pairs of 1/2 inch, phase-matched microphones (B&K type 4187), labelled as M1 through M4, are used together with a conditioning amplifier (B&K Nexus 2691). The separation distance between the microphones and their exact locations are indicated in Figure 4.1. Signals from the four microphones are acquired via the AD converter

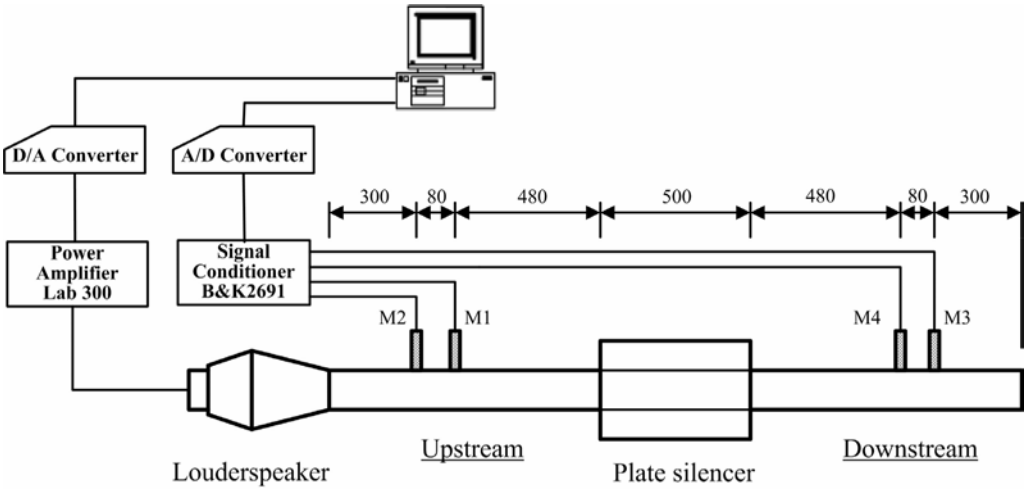

Figure 4.1: Schematic of the four-microphone, two-load measurement system. (dimensions in *mm*)

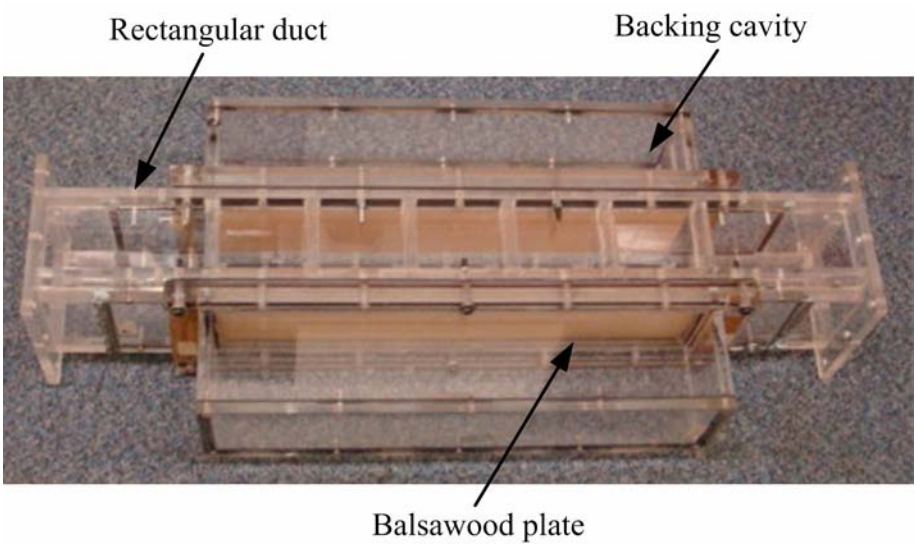

Figure 4.2: Photo of a prototype plate silencer using balsawood plates.

(NI. PCI-4452). Both A/D and D/A processes are controlled by an NI Labview program and the test is run by a loop of discrete frequencies from 40 Hz to 800 Hz with a increment of 10 Hz (coarse sampling) or 5 Hz (fine sampling). Two independent experiments under different downstream loading conditions are conducted to determine the TL of the tested silencer. In the current study, the first downstream boundary condition is a simple "rigid ending." The other one is "absorbing ending," which is implemented by connecting the downstream end of the duct to an absorptive chamber.

Figure 4.2 shows a photo of the prototype plate silencer using balsawood. The duct wall is made of 15-mm-thick acrylic so that it can be considered to be acoustically rigid. The cross-section of the duct is 100 mm×100 mm. The two cavities also have a cross section of 100 mm×100 mm and the length is 500 mm. With the geometry given, the first cut-on frequency in the rigid duct is around 1700 Hz, which is much higher than the upper limit of the measurement frequency range. The leading and trailing edges of the plates are clamped, and the final effective length of plates is 500 mm. The two lateral edges of the plates are inserted into a thin gap between the two constituent plates of the cavity walls. The clearance between the lateral edges of the plates and the cavity walls is less than 0.5 mm. Such a configuration is adopted to make sure that the plates can vibrate freely in the normal direction to the plate surface and simulate the two-dimensional behaviour of a beam while the leakage of noise from the main duct to the cavities via the gap is minimised.

Before measuring the TL of the plate silencer, the TL of the whole measurement system without the clamped plates is first measured. This measurement serves two purposes. One is to calibrate the measurement system, and the other is to check the

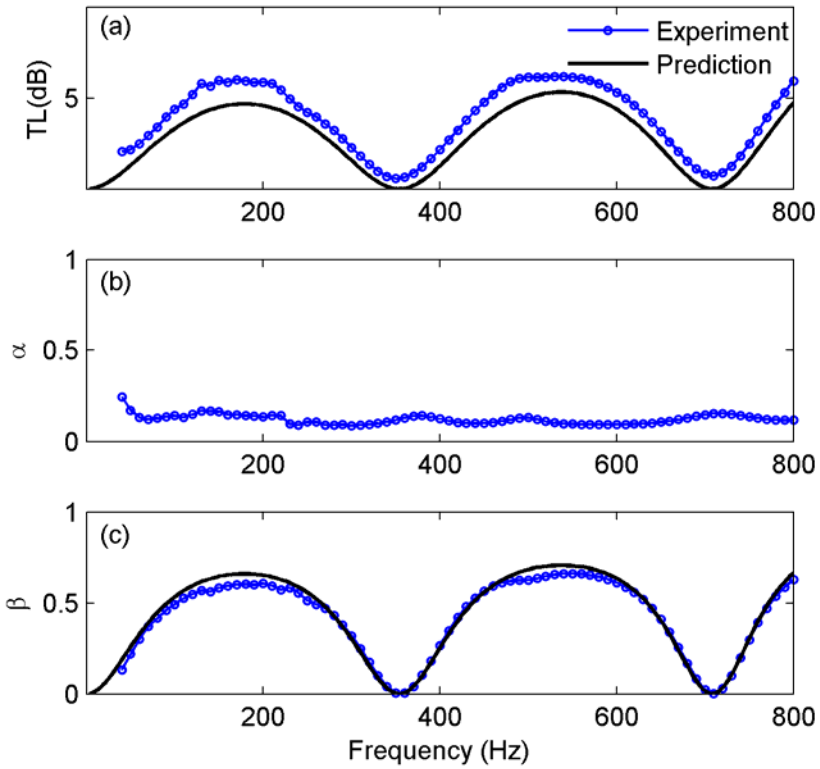

Figure 4.3: Comparison of the measured data (with open circles) with theoretical predictions (without open circles) for the expansion chamber. (a) TL. (b) The absorption coefficient α. (c) The reflection coefficient β.

damping level of the duct and the cavity. The TL spectrum, the absorption coefficient α, and the reflection coefficient β are measured and compared with the theoretical predictions in Figure 4.3. With the plate absent, the plate silencer becomes a rectangular expansion chamber. The theoretical results are calculated by assuming both the mass ratio and bending stiffness to be zero. Figure 4.3(a) indicates that the measured TL (line with open circles) compares with the theoretical solution well on the whole, except that the measured TL spectrum is about 0.5 dB higher than the predicted TL spectrum. It is argued here that the discrepancy is mainly due to the energy dissipation mechanisms which are necessarily present in the rig but excluded in the theory. As shown in Figure 4.3(b), the overall absorption coefficient of the

expansion chamber is around 0.1. The possible damping mechanisms include the cavity damping, wall vibration, etc. Since the absorption coefficient is small and sound reflection dominates, the damping effect of the experimental rig can be neglected when the balsawood plates are absent.

4.3 Validation experiment

4.3.1 Mechanical properties of the balsawood plate

In this experiment, two pieces of balsawood plates are installed flush with the duct wall. The plates are 517 mm long, 102 mm wide, and 2 mm thick. The physical and mechanical properties of balsawood vary greatly depending on its origin and growth conditions. According to Chart 1 given in (Ashby and Johnson, 2002), the density of balsawood ranges from 100 kg/m^3 to 220 kg/m^3, and the Young's modulus ranges from 2 GPa to 5 GPa. Since the bending stiffness of the plate is one of the most crucial design parameters, a three-point bending test is done to determine it experimentally. Figure 4.4(a) shows the schematic of the three-point bending test. The sample plate is of the size 90 mm × 32 mm × 2 mm, and the support span L is 50 mm. An axial static testing machine is used to apply the load gradually. The relationship between the applied load and the deflection at the middle point of the plate is shown in Figure 4.4(b). The response of the plate is rather linear as the deflection increases from 0 to 1.5 *mm*. Hence, the measured data within this region are used to find the Young's modulus. For a simply-supported beam given in this test, the deflection at the middle point and the applied load should satisfy the following relationship,

$$y = \frac{FL^3}{48EI}, \tag{4.1}$$

where, y is the deflection, F is the load applied, E is the Young's modulus, and I is the second moment of inertia. According to Figure 4.4(b), the Young's modulus E can be estimated as 2.6 GPa. The measured density of the balsa wood plate is 208 kg/m^3. According to the normalisation scheme described in Chapter 2, the dimensionless bending stiffness and mass ratio of the plate in the silencer can be calculated as B=0.0123 and m=3.4.

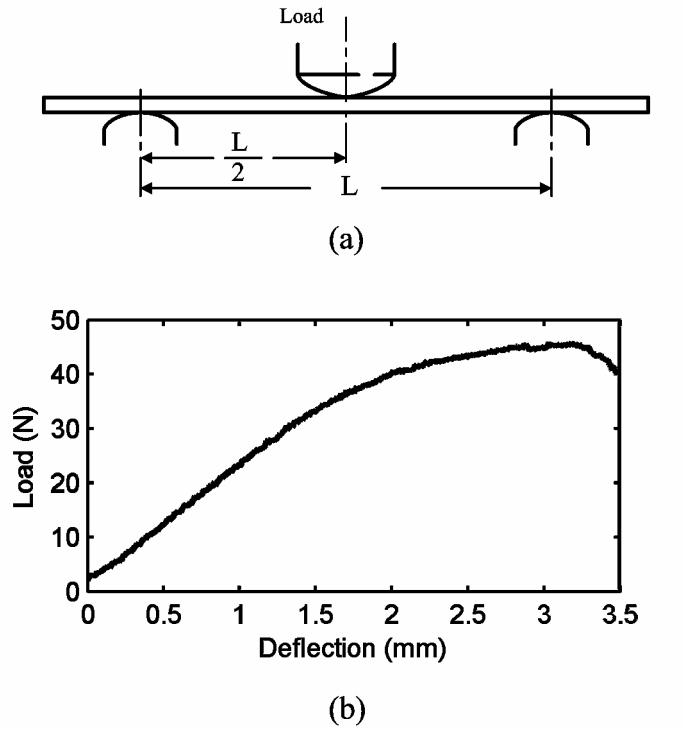

Figure 4.4: Three-point bending test of the balsawood plate. (a) Schematic of the bending test. (b) Load versus deflection at the middle point.

4.3.2 Results analysis

Figure 4.5 compares the experimental results (solid lines with open circles) and the theoretical predictions (solid lines without open circles) of the tested plate silencer. The theoretical results are calculated using the parameters found in Section 4.3.1 (B=0.0123, m=3.4). Since the damping effect is not considered in the theoretical model, the predicted absorption coefficient is zero. The frequency positions of the six predicted spectral peaks in Figure 4.5(a) are 54 Hz, 109 Hz, 224 Hz, 306 Hz, 415 Hz, and 727 Hz. Because the bending stiffness of the plate used is much smaller than the optimal one (B_{opt}=0.153 at m=3.4, see Figure 3.3 (b)), the TL between the first and second peaks is so low that the maximum stopband begins from 218 Hz and ends at 318 Hz, consisting of the third and fourth peaks. Note that the frequency ratio f_2 / f_1=1.46 is not as high as the optimal one, and the performance of the prototype plate silencer may be unsatisfactory in the real application, but it suffices to serve the objective of model validation. Note also that the balsawood used here is relatively heavy and soft in the whole range of balsawood available. For better performance of the plate silencer, a lighter and stiffer balsawood may be used.

Figure 4.5(a) compares the measured TL spectrum with the theoretical prediction. Evidently, the spectral peaks and the overall spectral shape of the measured TL match those of the theoretical results, which means that the basic theoretical model is correct for the experimental rig. However, the predicted TL curve has sharp peaks while that from the experiment is quite smooth. This, again, implies significant energy dissipation mechanisms in the experimental rig, which are excluded in the theoretical model. As shown in Figure 4.5(b), the measured

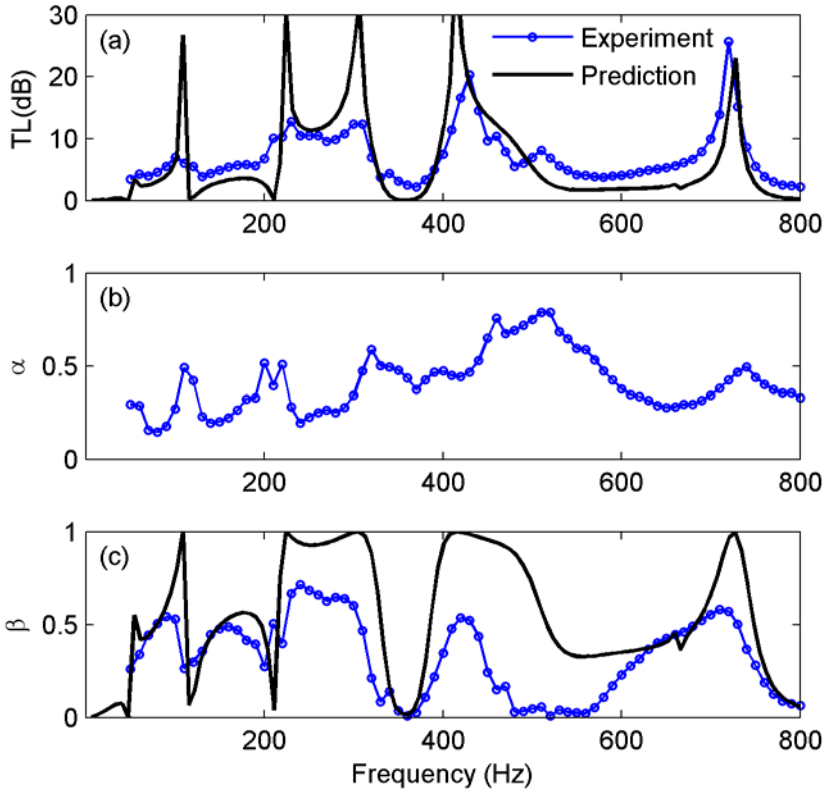

Figure 4.5: Comparison of experimental data (with open circles) with theoretical predictions (without open circles). (a) TL, (b) The absorption coefficient α . (c) The reflection coefficient β . The plate properties are measured as: bending stiffness *B*=0.0123; mass ratio *m*=3.4.

absorption coefficient α ranges from 0.15 to 0.5 in the low frequency region (say, below 400Hz) and from 0.3 to 0.8 in the relative high frequency region (above 400 Hz). Note that the overall sound absorption coefficient is only around 0.1 when the balsawood plates are absent. It is reasonable to assume that the main energy dissipation mechanism in the plate silencer is the structural damping in the plate. Figure 4.5(c) compares the predicted reflection coefficient β . Obviously, the level of the measured reflection coefficient is lower than that of the prediction. One explanation for this phenomenon is that the structural damping reduces the vibration level of the balsawood plates, which in turn results in a lower level of sound

reflection. On the other hand, the existence of sound absorption also lowers the chances of the incident noise being reflected. Nevertheless, comparison between Figures 4.5(b) and 4.5(c) shows that the mechanism of sound reflection still dominates over the sound absorption in the low frequency range. To summarize, the experimental results are in agreement with the theoretical prediction, but the damping effect, which is excluded previously, should be considered in the theoretical model to better represent the real physics behind the plate silencer.

The damping effect is considered in the theoretical model by adopting a Rayleigh damping model, and the coupled dynamics of the plate (beam) becomes, for harmonic vibration of time dependence $e^{i\omega t}$,

$$\frac{\partial^2}{\partial x^2}\left(B(x)\cdot\frac{\partial^2\eta}{\partial x^2}\right)(1+i\sigma_s)+m(x)\cdot\frac{\partial^2\eta}{\partial t^2}\cdot(1-i\sigma_m)+(p_+-p_-)=0\,, \tag{4.2}$$

where σ_s and σ_m are, respectively, the stiffness and mass damping coefficients. Two cases with different damping coefficients are investigated. In the first case, σ_m=0.15, σ_s=0. The TL, absorption coefficient, and reflection coefficient are shown in Figures 4.6(1a)−4.6(1c), respectively. It can be observed that the experimental data are in good agreement with the theoretical results when the frequency is below 360 Hz. However, the absorption coefficient is underestimated in relative high frequency. In the other case, the damping coefficients are chosen as σ_m= σ_s=0.05, and the results are shown in Figures 4.6(2a)−4.6(2c). With such a combination of σ_m and σ_s, the measured TL, absorption coefficient, and reflection coefficient are all in agreement with the theoretical results on the whole. But in the frequency range, from 240 Hz to 300 Hz, the reflection coefficient is overestimated slightly. The two case studies

suggest that the damping effect can be modelled roughly with a proper combination of mass and stiffness damping coefficients, although the two sets of damping coefficients are chosen somewhat arbitrarily.

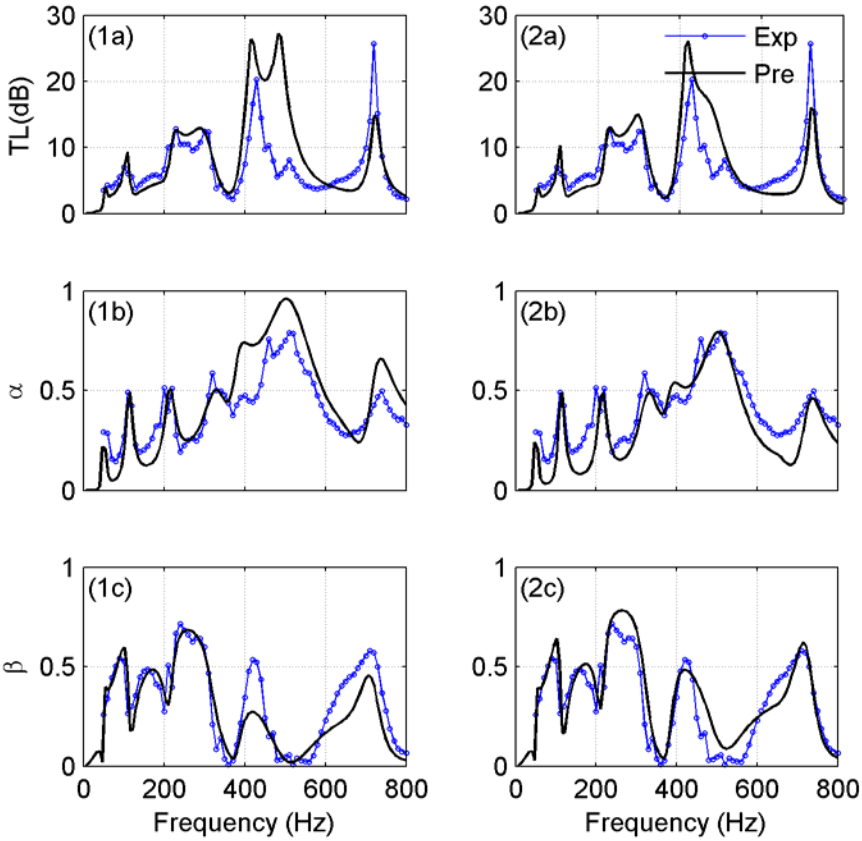

Figure 4.6: Modelling of plate damping mechanisms with two set of damping factors. (1a),(1b), and (1c) show the results with $\sigma_m = 0.15, \sigma_s = 0$. (2a), (2b), and (2c) show the results with $\sigma_m = 0.05, \sigma_s = 0.05$.

4.4 Plate silencer using sandwich plate

4.4.1 Sandwich construction

The sandwich plate consists of two thin aluminium sheets each of thickness h_t, separated by a thick core of thickness h_0, as shown in Figure 4.7. The Young's modulus E_t and density ρ_t for the aluminium sheet are 4.87×10^5 (69GPa) and 2204 (2700 kg/m^3), respectively. The values shown in the brackets are the corresponding dimensional values, which are calculated with air density ρ_0^* =1.225 kg/m^3 and speed of sound c_0^*=340 *m*/*s*. The core material is Rohacell ® IG-31 (Rohacell, 1987) with the density, $\rho_{Rohacell}$, and Young's modulus, $E_{Rohacell}$ being 26 (32 kg/m^3) and 254 (36 MPa), respectively. Rohacell ® is a polymethacrylimide- (PMI-) hard foam, that is usually used as a core material for sandwich constructions. In comparison to all other foams it offers the best ratio of weight and mechanical properties (Rohacell, 1987). For such a three-layer sandwich construction, the effective bending stiffness per unit width of the beam is found as (Allen, 1969),

$$B = \frac{1}{6}E_t h_t^3 + \frac{1}{2}E_t h_t (h_t + h_0)^2 + \frac{1}{12}E_{Rohacell} h_0^3 . \tag{4.3}$$

The three terms on the right-hand side of the above expression represent, respectively, the bending of the skins about their centroidal axis, bending of the skins about the centroid of the whole beam, and bending of the core itself. The effect of shear deflection is negligible compared with the bending deflection; hence, it is neglected in calculating the flexural rigidity of the sandwich beams. By assuming the sandwich beam as a homogeneous one, the equivalent Young's modulus is estimated as,

$$E = B / I \,, \tag{4.4}$$

with,

$$I = \frac{(h_0 + 2h_t)^3}{12} \,. \tag{4.5}$$

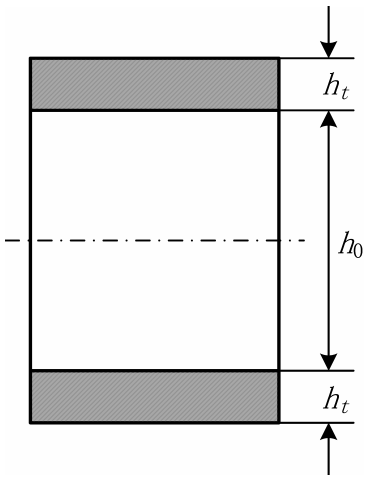

Figure 4.7: Cross sectional view of the sandwich plate consisting of two thin skin sheets each of thickness, h_t, and a thick core of thickness , h_0.

For a homogeneous plate of rectangular cross section, the dimensionless bending stiffness is found to be,

$$B = \frac{m^3 E}{12\rho_s^3} \,, \tag{4.6}$$

where m is the mass ratio; E is the dimensionless Young's modulus and ρ_s is the dimensionless density. Equation (4.6) shows that, for a given set of m and B to be satisfied, the only crucial material property is E/ρ_s^3 . Hence, an optimal design of the sandwich plate is the one that has the highest ratio of E/ρ_s^3 , which is determined by the ratio between the thicknesses of the thin facing sheet ,h_t, and the core, h_0. As shown in Figure 4.8(a), E/ρ_s^3 varies as a function of h_t / h_0, and the maximum value,

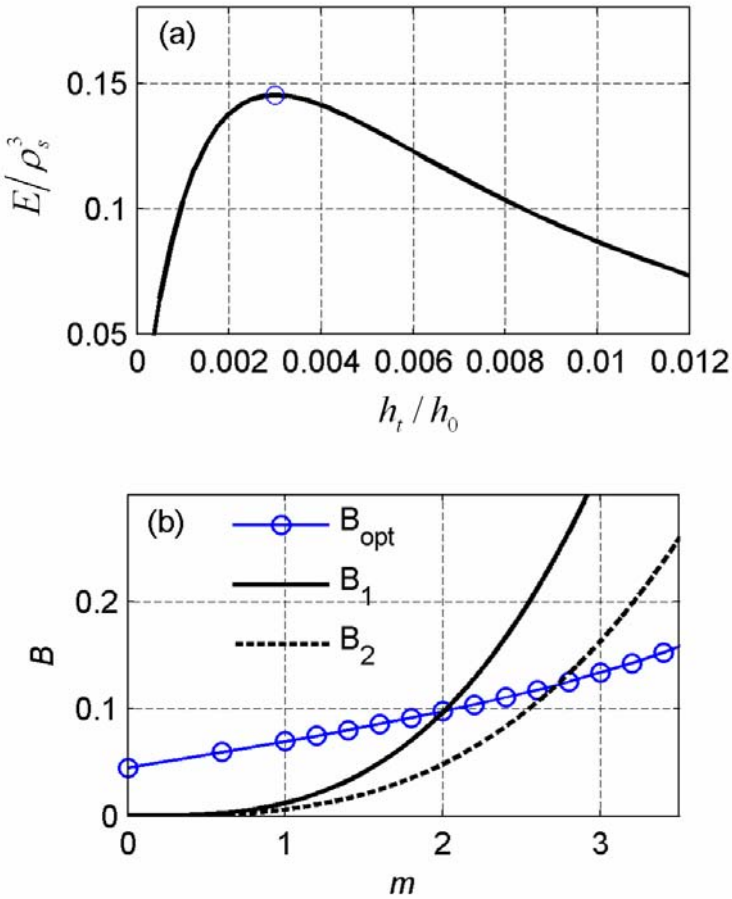

Figure 4.8: Optimal design of the sandwich construction with given core material (Rohacell IG-31) and skin sheet (aluminium). (a) Variation of E/ρ_s^3 with respect to the ratio of h_t / h_0. (b) Comparison between the achievable maximum bending stiffness, B_1, and the required optimal bending stiffness B_{opt}. The curve for B_2 shows the situation where 50% loss of bending stiffness occurs during the sandwich construction.

E/ρ_s^3 =0.1453, is reached when h_t / h_0 =0.003. Keeping h_t / h_0 at the optimal value of 0.003, Eq. (4.6) gives the achievable maximum bending stiffness, B_1, of the sandwich plate for a given mass ratio *m*. The feasibility of using the proposed sandwich beam to realize the low frequency plate silencer is investigated below. Note that the optimal bending stiffness B_{opt} for a plate silencer to function with the widest the bandwidth also varies with *m*. Figure 4.8(b) compares the maximum bending

stiffness of the sandwich plate, B_1 (solid line), with the required optimal bending stiffness B_{opt} (solid line with open circles) as functions of the *m*. As shown in Figure 4.8(b), the proposed sandwich plate design would satisfy the optimal bending stiffness condition when the mass ratio is around $m = 2$. In practice, a loss of bending stiffness may occur due to disbanding or other reasons (Lingaiah and Suryanarayana, 1991; Lim, et al., 1995; Kim and Hwang, 2001), and the predicted bending stiffness for the sandwich construction can not be fully reached. Assuming only 50% of the predicted bending stiffness can be obtained, the corresponding bending stiffness B_2 is shown in Figure 4.8(b) in dashed line. In this case, a sandwich plate with mass ratio m=2.7 would become stiff enough for the optimal design of the plate silencer.

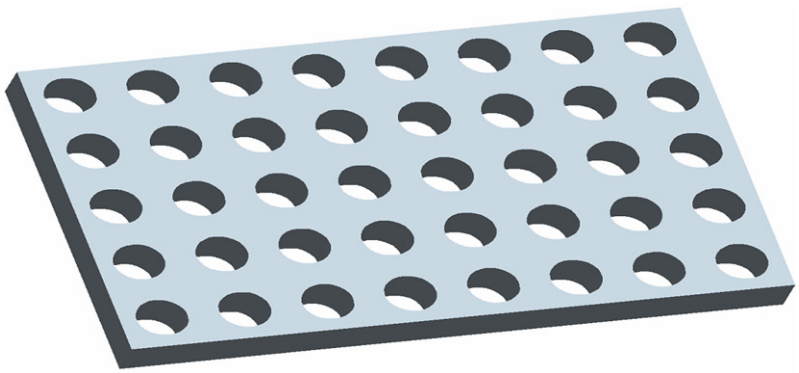

Figure 4.9: Schematic for the perforated foam core used in the sandwich construction. Perforation diameter: 5 mm.

For comparison purposes, three types of sandwich plates with different mechanical properties are manufactured by bonding two aluminium sheets of the thickness 0.025 *mm* to different Rohacell® foam cores using epoxy resin. For the first type (designated as type I), the core thickness is 4 *mm*, and a series of holes (diameter: 5 *mm*) are drilled on the core with a perforation rate of about 35%, as shown in

Figure 4.9. The perforation can reduce the weight of the final sandwich plate while the bending stiffness remains nearly unchanged. For types II and III, the core thickness is 4 *mm* and 3 *mm*, respectively, without any perforation. The final surface density of the three sandwich plates are, 0.3 kg/m^2, 0.337 kg/m^2, and 0.3 kg/m^2, respectively. The equivalent Young's modulus E is measured through three-point bending test as, 1.61 GPa, 1.61 GPa, and 2.32 GPa. In the following experimental study, the cross section of the rigid rectangular duct is of the size $100\,mm \times 100\,mm$. Therefore, the dimensionless bending stiffness and mass ratio for the three plates can be calculated using the normalization scheme described in Chapter 2, as listed in Table 4.1.

Table 4.1. Properties of the sandwich plates.

Type	Core thickness (mm)	plate-to-air mass ratio, *m*	Equivalent dimensionless *B*	Perforation ratio of core
I	4	2.4	0.061	35%
II	4	2.75	0.061	n/a
III	3	2.4	0.037	n/a

4.4.2 Experimental results on sandwich plates I, II & III

The performances of three plate silencers with different sandwich construction are studied experimentally. Depending on the types of the sandwich plate used, the three silencers are designated as silencer I, silencer II, and silencer III, respectively. Since the sandwich plate type I has the best mechanical properties (highest bending stiffness; lowest mass ratio) out of the three sandwich constructions, it is expected to perform better than the other two.

A. Benchmark results for silencer I

The measured data for silencer I are shown in Figure 4.10. The TL spectrum is shown in Figure 4.10(a) in thin solid curve with open circles, together with the predicted performance of the expansion chamber of the same cavity geometry (dashed curve) for comparison. Three spectral peaks are observed in the measured TL curve of the plate silencer at frequencies: 140 Hz, 250 Hz and 420 Hz. The first two peaks and the trough between them form a continuous frequency band within which good noise reduction level is obtained. With a criterion level TL_{cr} =10 dB, a wide stopband, $f \in$ [133 Hz, 274 Hz], or in the dimensionless form, $f \in [0.039, 0.08]$, can be observed. The logarithmic bandwidth for silencer I is f_2 / f_1=2.1, which is slightly larger than one octave. According to Huang (2004), a dimensionless frequency of 0.077 can be chosen as a demarcation line for the 'medium' frequency below which the porous duct lining may be considered ineffective. Following this specification of 'medium' frequency, the stopband for silencer I, $f \in [0.039, 0.08]$, falls almost completely into the low frequency region. The silencing performance between the second and third peaks, say, from 275 Hz to 400 Hz, is unsatisfactory with low TL level. It can be shown by simulation that this phenomenon is caused by insufficient bending stiffness of the plate. The TL level can be lifted, for example, to above the criterion level, TL_{cr}, by adopting a stiffer plate, and a wider stopband is then expected. However, the trade-off is that the whole stopband will shift to higher frequency region if the plate-to-air mass ratio remains the same or increases, as investigated in Section 3.4.3.

Figures 4.10(b) and 4.10(c) show the measured sound energy absorption coefficient and reflection coefficient, respectively. At the stopband where the plate silencer functions effectively, the reflection coefficient dominates with an overall level of around 0.7, while the absorption coefficient is at a level of around 0.2 to 0.25. It confirms that main mechanism of sound reduction in the plate silencer is reflection, which conforms to the theoretical assumption of the plate silencer design. As frequency increases, the absorption coefficient becomes significant, reaching a level of around 0.5 at the relative high frequency.

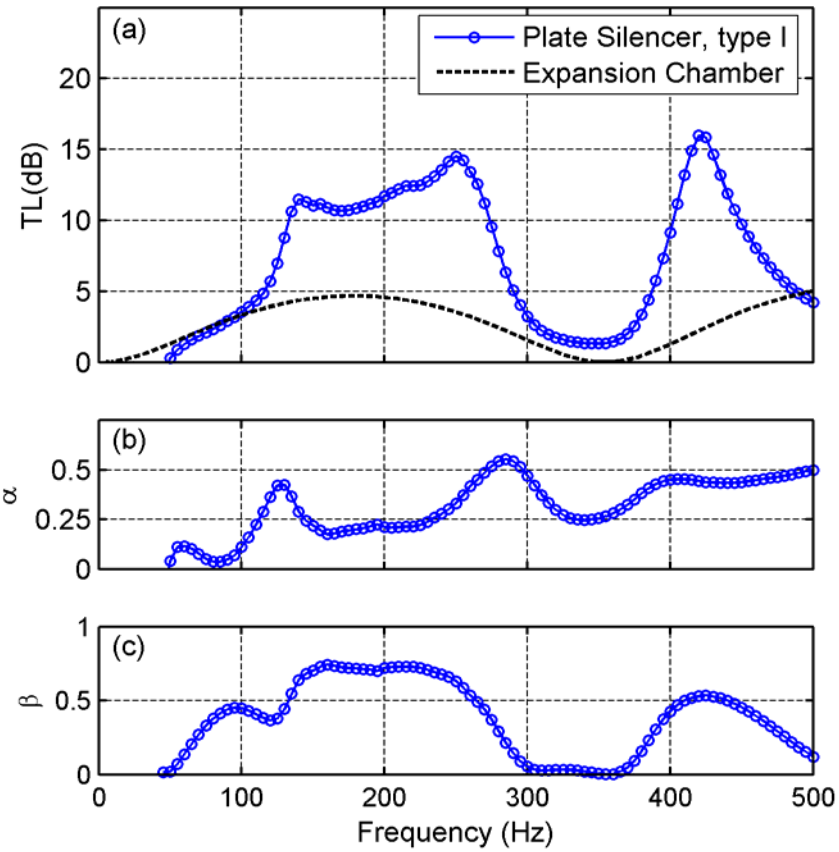

Figure 4.10: Measured data for plate silencer I. (a) TL. The predicted TL for an expansion chamber of the same cavity geometry is also given in dashed line for comparison. (b) Absorption coefficient. (c) Reflection coefficient.

B Comparison with theoretical predictions

The theoretical predictions for the plate silencers with sandwich plates require for a proper mathematical modelling of the dynamics of the sandwich plate. Generally speaking, it is appropriate to represent a thin plate of homogeneous material with an Euler-Bernoulli beam in a two-dimensional model as described by Eqs. (3.1) or (4.2). For such an ideal model, deflection of the beam is caused by bending only, and there is no shear effect involved. But for a sandwich beam to be investigated in this study, its deflection is caused not only by bending but also by shear and rotation in the core (Platema, 1966). Hence, strictly speaking, the coupled dynamic equation for a sandwich beam is different from Eqs. (3.1) or (4.2) that is based on a homogeneous beam. However, for the plate silencer design, the sandwich beam functions in a very low frequency range. In this frequency range, the flexural motion of a sandwich beam is mainly determined by pure bending of the beam (Nilsson, 2002), so that the shear effects can be neglected. Hence, it is argued that it is reasonable to predict the performance of a sandwich plate silencer with a model based on homogeneous plate. In other words, the sandwich plate may be treated as homogeneous in the plate silencer design. This argument is validated in the following experimental study.

A comparative study is conducted between the experimental results and the theoretical predictions, as shown in Figure 4.11. The solid curves with open circles show the measured data of silencer I. The corresponding predicted data are calculated using the mechanical properties listed in Table 4.1. An ideal design of a plate silencer assumes that there is no energy dissipation in the system and the noise reduction is purely caused by sound reflection due to the plate vibration. This extreme situation is

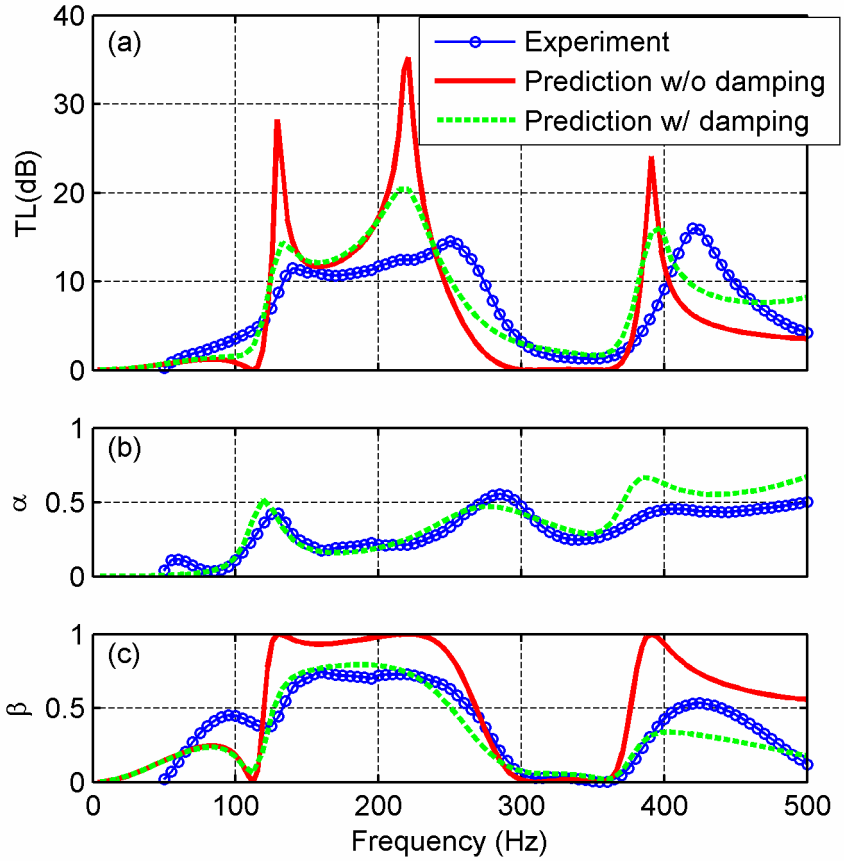

Figure 4.11: Comparison of experimental data (solid curves with open circles) with theoretical predictions (solid curves: without structural damping; dashed curves: with structural damping: σ_m =0.15 and σ_s =0.05.) for plate silencer I. (a) TL. (b) Absorption coefficient. (c) Reflection coefficient.

simulated by taking $\sigma_m = \sigma_s = 0$ in the theoretical model (see Eq. (4.2)), and the predicted data are shown in solid curves. However, several energy dissipation mechanisms exist in the real experimental rig, just as in the validation experiment where balsawood is used. Again, a Rayleigh damping model is adopted to characterise the sound absorption in the rig roughly. When the plate damping is included in the theoretical model, the corresponding predicted results are shown in dashed curves in Figure 4.11. The damping ratio for the sandwich plate is measured

using the free decay method. In doing so, the decay rate for the free vibration of a cantilever sandwich beam (size: 190mm×20mm ×4 mm) is measured using a laser vibrometer (Polytec type with controller FV-3001 and sensor head OFV-303), and the damping ratio for the cantilever beam is found to be 0.09. The mass and stiffness damping coefficients used in the Rayleigh damping model are,

$$\sigma_m = 0.15,\ \sigma_s = 0.05, \tag{4.7}$$

which correspond to an equivalent damping ratio of 0.1. Considering that the plate damping is not the only damping mechanism in the experimental rig, the plate damping ratio used in the theoretical model is slightly larger than the measured value of 0.09.

Figure 4.11(a) compares the TL spectra. When damping effects are excluded, three sharp spectral peaks can be observed in the predicted TL spectrum (solid curve). But the corresponding peaks for the experimental results (solid curve with open circles) are smoothed out and shifted to higher frequencies by 10-20 Hz. When the plate damping is included in the modelling, the predicted spectral peaks are also smoothed out by the structural damping and the overall TL spectra between the prediction (dashed curve) and the experiment (solid curve with open circles) get closer to each other. The stopbands between the predictions and the experimental results are similar. When the plate damping is excluded, the predicted stopband for the tested silencer is $f \in [124, 246]$ Hz, while the experimental result is $f \in [133, 274]$ Hz. The ratio of frequency limits, f_2 / f_1, are 2.0 and 2.1 respectively, which conforms to the theoretical findings by Huang (2006) that a plate silencer with light plate damping has a slightly wider bandwidth than the one without any damping.

Despite the slight discrepancies between the two TL curves, the spectral peaks and overall spectral shape of the measured TL match those of the theoretical prediction.

Figures 4.11(b) and 4.11(c) compare the sound absorption coefficient α and the sound reflection coefficient β, respectively. When the damping effects are excluded, there is no sound absorption in the prediction. Because of the existence of significant energy dissipation mechanism in the experimental rig, the level of the predicted reflection coefficient (solid curve) is higher than the measured one (solid curve with open circles). When the plate damping is considered in the modelling, the predicted sound absorption coefficient and reflection coefficient (dashed curves) better agree with the measured ones (solid curves with open circles), especially in the low frequency range. In summary, it can be concluded that, as far as the low frequency is concerned, it is appropriate to predict the performance of a sandwich plate silencer using a theoretical model based on homogeneous plate. The damping mechanism inside plate silencer can be roughly characterised by the structural damping of the sandwich plate.

C. Effect of mass ratio and bending stiffness

Silencer II and silencer III are also tested and their results are compared with silencer I to show the variation of silencing performance with different plate mass ratio and bending stiffness. Figures 4.12(a) and 4.12(b) compare the measured and predicted TL spectra, respectively. The damping coefficients are chosen as σ_m=0.15 and σ_s=0.05 in the predictions for all the three silencers. The effect of plate mass is generally counterproductive, which is partly verified by the comparison between silencer I and silencer II. The two silencers have almost the same bending stiffness

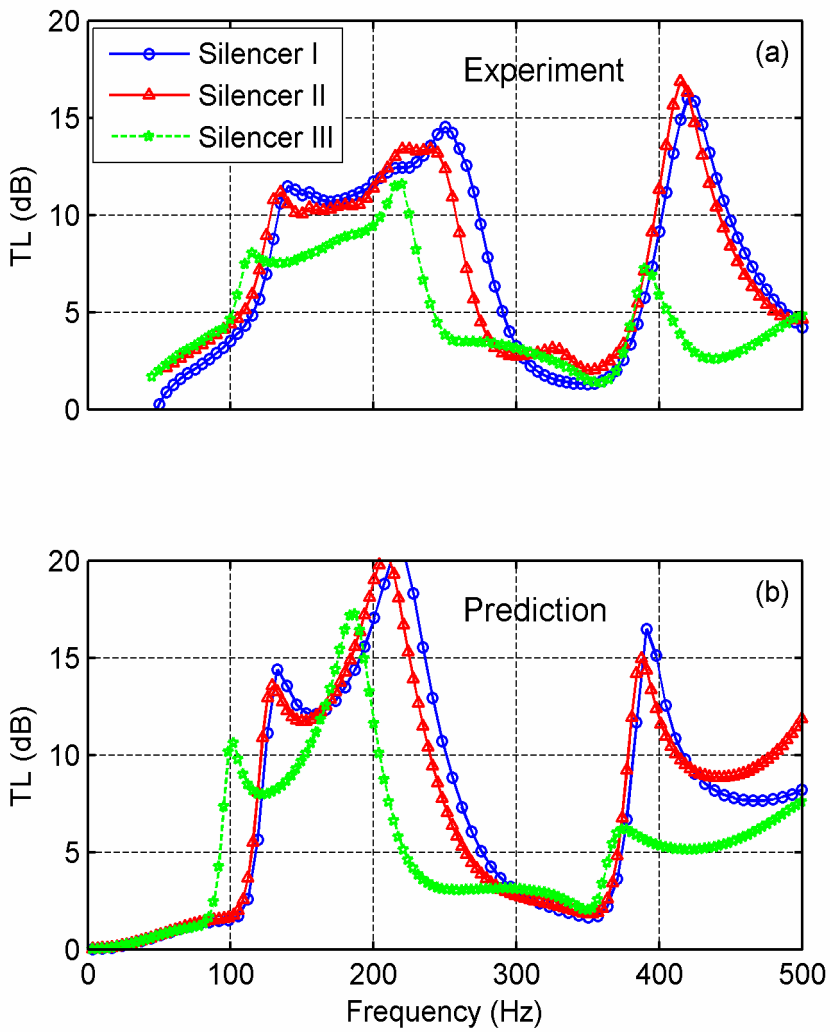

Figure 4.12: TL comparison among three plate silencers with different plate properties (I: m=2.4, B=0.061; II: m=2.75, B=0.061; III: m=2.4, B=0.037). (a) Experimental results. (b) Predictions with the structural damping of the plate modelled as σ_m =0.15 and σ_s =0.05.

but different plate mass ratios. Since the mass ratio for silencer I (m=2.4, B=0.061) is smaller than silencer II (m=2.75, B=0.061), it has a wider bandwidth and higher TL level between the first two spectral peaks, as shown in both Figures 4.12(a) and 4.12(b). Note that the spectral peaks and the whole stopband for silencer I shift a little towards higher frequency. However, it does not necessarily mean that a heavier

plate can achieve better low frequency performance since it has a lower trough between the first and second peaks. The performance comparison between silencer I (m=2.4, B=0.061) and silencer III (m=2.4, B=0.037) shows the importance of bending stiffness in the design of plate silencer. Due to the insufficient bending stiffness, the overall performance of silencer III drops significantly in comparison with silencer I, as shown in Figure 4.12(a). The variation of the measured TL spectra between silencer I and silencer III conforms to the prediction shown in Figure 4.12(b).

4.4.3 Partial sandwich plate

In order to obtain various different bending stiffness with given core material and facing sheet, the sandwich plate can be constructed by adhering rigid aluminium sheets to a portion of the foam cores, hence partial sandwich plate. Figure 4.13 shows such a partial construction with four pieces of aluminium membranes bonded to the core of the width 102 mm, leaving the middle part of the Rohacell core un-reinforced. The aluminium membrane is 0.025mm thick and 30mm wide. The final sandwich plate is of the size 517 mm × 102 mm × 6 mm. The average mass ratio $\overline{m}$ is 2.9, and the bending stiffness of the sandwich plate can also be measured using the three-point bending stiffness test. The advantage of this construction method is that the bending stiffness of the final plate can be easily adjusted through varying the width of the bonding aluminium membranes. Note that the bending stiffness along the width direction is non-uniform. Numerical simulation shows that, as far as the plate silencer is concerned, the vibration velocity in this direction is almost uniform, and the three-dimensional effect due to the nonuniform bending stiffness can be neglected. Attempt also has been made to predict the performance of the partial sandwich plates

using the mathematical model based on homogeneous plate. However, as the dynamics of the partial sandwich plate are more different from the homogeneous plate than the full sandwich plate, the deviation of the experimental results from the prediction is rather obvious even in the low frequency region.

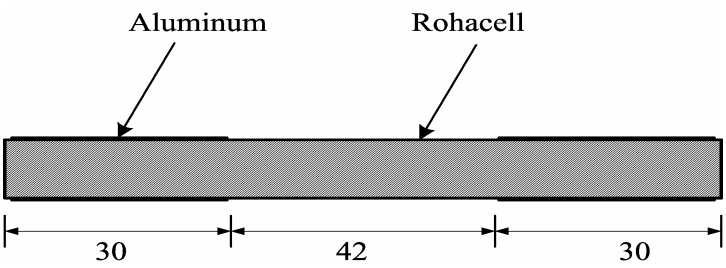

Figure 4.13: Cross section of the partial sandwich plate (dimensions in mm).

The experimental results for the sandwich plate silencer are shown in Figure 4.14. As shown in Figure 4.14(a), if TL_{cr}=10dB is chosen as the criterion level, a wide stopband can be observed from $f_1 = 158$ Hz to $f_2 = 332$ Hz, and the frequency ratio f_2 / f_1 is 2.1 that is a little larger than one octave. The good performance demonstrates again that sandwich structure has a potential advantage in the design of low frequency plate silencer. Good performance can also observed in relative high frequency region, e.g., from 400 Hz to 600 Hz. But at high frequency, the sound reflection contributes less to the total transmission loss, and the sound absorption becomes dominant, as shown in Figures 4.14(b) and 4.14(c).

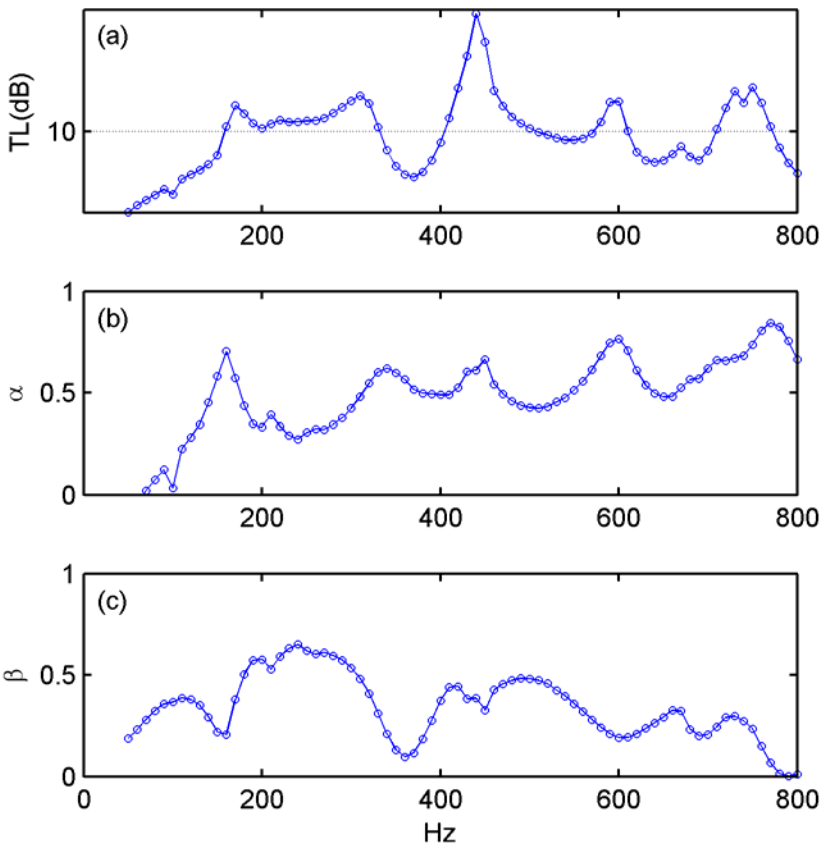

Figure 4.14: Experimental data for the partial sandwich plate. (a) TL. (b) Absorption coefficient. (c) Reflection coefficient.

4.5 Summary

The two-dimensional theoretical model is tested experimentally using balsawood. The spectral peaks and shapes of the measured TL are in agreement with those calculated analytically, which demonstrates that the basic model of the clamped silencer is correct. In the low frequency range, say, below 400 Hz, the sound reflection still dominates over the sound energy dissipation, although significant sound absorption exists in the plate silencer especially at high frequency. The exact

nature of the damping mechanism has not been identified, but the main mechanism is believed to be the plate damping. A Rayleigh damping model is adopted to represent the plate damping in the theoretical model. Results show that with a proper combination of mass and stiffness damping coefficients, the damping effect can be modelled roughly in agreement with the experimental data.

According to the theoretical studies, a good design of the plate silencer requires very light but extremely stiff plates, irrespective of the plate boundaries. Such a condition is generally difficult to satisfy with existing homogeneous plate. Although the balsawood used in the validation experiment is one of the best materials for this purpose, it is too heavy and soft for the plate silencer. Hence, the prototype plate silencer in this experiment only works in a relative narrow frequency range with the overall stopband shifted to higher frequencies.

A broadband low frequency plate silencer is experimentally realized using sandwich plate. The requirement for high bending stiffness and low density of the plate is satisfied with a sandwich construction by adhering two high rigidity thin sheets with a relative thick and light foam core. Three types of sandwich plates with different mechanical properties are tested. The plate having the highest bending stiffness and lowest density results in a measured stopband from 133 Hz to 274 Hz in which the transmission loss is higher than 10 dB over the whole frequency band. Comparisons between the three sandwich plates partly confirm the theoretical findings on the effect of plate properties on the silencer performance. In addition, partial sandwich plates are tested, and good silencing performance is also observed.

As the dynamic characteristics of the sandwich plate is quite different from that of a homogeneous plate, the possibility is explored to provide simplified simulation

model to guide the practical design of the sandwich plate silencer. It is found, as far as low frequency is concerned, the mathematical model based on homogeneous plates can provide satisfactory prediction on the performance of a sandwich plate silencer. Experimental and theoretical results are found to be in fair agreement.

Chapter 5

ANALYSES OF SOUND REFLECTION AND ABSORPTION MECHANISMS IN A THREE-DIMENSIONAL PLATE SILENCER

5.1. Introduction

In all previous studies on drumlike and plate silencers, two rigid cavities are equipped on two opposite sides of a rectangular duct. The plates, which are flush-mounted with the duct walls, cover the cavities completely. Such a configuration is in fact two-dimensional, say on *x*-*y* plane. In this chapter, numerical study is extended to three-dimensional designs to investigate the potential improvement in sound reflection by adopting better geometrical configurations. Also, the extension to three-dimensional design will feed the needs of various practical applications where a three-dimensional configuration is more appropriate (for example, circular ducts).

Four different three-dimensional configurations are investigated and compared with the two-dimensional design. One direct way to construct a three-dimensional plate silencer is to combine two identical two-cavity plate silencers, one on *x*-*y* plane and the other on *x*-*z* plane, in parallel to form a so-called “four-cavity plate silencer”, in which all of the four sides of the rectangular duct are covered by plates. Alternatively, the four cavities can be replaced by a circular chamber and the rectangular duct itself may also be replaced by a quasi circular one. Unlike the two-dimensional plate silencer studied in previous Chapters, both the four-cavity and the

circular designs involve many three-dimensional effects, such as the loading on one plate caused by the vibration of neighbouring plates, as well as the effect of the three-dimensional cavity. Although the method of solution developed for the two-dimensional system in Chapters 2 and 3 may be extended to analyze the current problem, a finite element method is more convenient to model and simulate such a coupled three-dimensional system.

The second type of three-dimensional silencer investigated here is the hybrid silencer combining reactive and dissipative elements in a parallel manner. The motivations for such design are as follows. Like any other reactive silencers, the plate silencer generally has poor performance at high frequencies. On the other hand, dissipative silencers using sound-absorbing materials can attenuate the high-frequency noise easily. But their performance (attenuation) is usually rather poor at low frequencies. Hence, it is expected that a combination of a reactive plate silencers with the dissipative elements can lead to a silencer effective from low to high frequency range. Additionally, the interaction between plate vibration and sound dissipation may improve the silencing performance in low frequency, which is also a desirable property for the low frequency wave reflector itself. One straightforward design of a hybrid silencer is to add sound absorbing materials to the cavity covered by the vibrating plate, as investigated by Huang (2006). Numerical results showed that the use of sound absorbing material in the covered cavity is marginally beneficial for the stop bandwidth since the presence of the sound absorption material in the cavity has the general effect of suppressing the plate response leading to reduced wave reflection capability. Instead of filling the cavity covered by plate with sound absorbing material, the alternative method is to fill neighbouring cavities reserved for

this purpose in a three-dimensional design. For example, in a four-cavity design similar to the cross section view shown in Figure 5.3(a), a pair of two opposing cavities are used for plate silencer, while the other two are filled with sound absorbing material. The result is called a hybrid silencer arranged in parallel occupying a small axial distance. On the other hand, when four plate-covered cavities are all used for sound reflection, it is designated as a four-cavity wave reflector.

In what follows, finite element simulation shows that the three-dimensional configurations perform slightly better than the corresponding two dimensional-design, especially in the relatively high frequency range. Further analysis shows that the three dimensional design gives better plate response at higher axial modes than the simple two dimensional design. By introducing sound absorption mechanism to the plate silencer via additional dissipative chambers, the proposed hybrid silencer is able to achieve a good moderate bandwidth with much reduced total length in comparison with the pure absorption design.

5.2. Theoretical outline

5.2.1 Finite element modelling

The finite element modelling procedure for a four-cavity wave reflector is presented below. For other three-dimensional plate silencers considered in this study, similar procedures can be followed, hence the details are not given. The so-called four-cavity wave reflector can be considered as a parallel combination of two two-cavity plate silencers, in which each module of cavity-backed plate is assumed to be identical to the opposite one. The cross section of the rigid duct is assumed to be

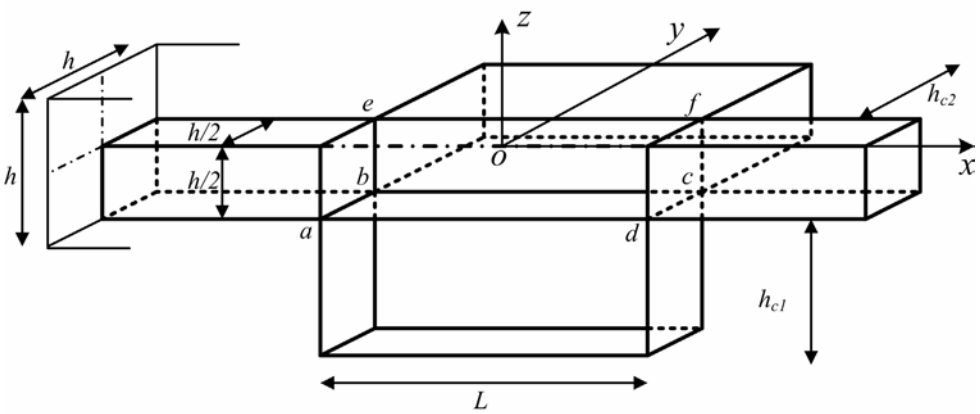

Figure 5.1: The quarter model of a four-cavity wave reflector (or hybrid silencer). The bottom and top (not shown) cavities have a length of *L* and depth h_{c1}; the back and front (not shown) cavities have a length of *L* and depth h_{c2}. In the case of a hybrid silencer, the bottom and top cavities are used to reflect sound and the other two cavities are filled with sound absorption materials. Otherwise, all of the four cavities are for sound reflection.

square and the height is *h*. Only one quarter of the four-cavity wave reflector needs to be modelled because of the symmetry in the system. As shown in Figure 5.1, the bottom cavity of depth h_{c1} is covered by a plate (*a*-*b*-*c*-*d*) of length *L* and width *h*, or half width *h*/2 in the quarter model in Figure 5.1. Similarly, the back cavity of depth h_{c2} is covered by a plate (*b*-*e*-*f*-*c*) of the same size as the plate (*a*-*b*-*c*-*d*). The leading and trailing edges of the plates, that is, *a*-*b*, *c*-*d*, *b*-*e*, and *c*-*f* are simply supported. These edges may also be clamped as in the two-dimensional study in Chapter 3, and similar results can be obtained and are not presented here. The other four edges are set free to allow the plate to respond to incident sound waves with high vibration magnitude. Suppose that a plane incident sound wave comes from the left to the right with unit amplitude,

$$p_i = e^{i(\omega t - k_0 x)}, \tag{5.1}$$

and it induces the plates (*a-b-c-d*) and (*b-e-f-c*) to vibrate with normal displacement of complex amplitude $\eta_1(x, y)$, $\eta_2(x, z)$ with the same time dependence, exp($i\omega t$), which is henceforth omitted. The plate motion radiates sound in both direction of the duct axes, $\pm x$, and imposes a radiation pressure on the plate surface. The problems of acoustics and plate vibration are coupled strongly.

Femlab® is a software package for solving partial differential equations based on Finite Element Method (FEM). Because of its strong multi-physics capability, Femlab® (version 3.1) is chosen to solve the current vibroacoustics coupling problem. The code will be validated by comparing its result for a different configuration for which analytical method has been established in Chapter 2. In the current numerical simulation, there are two types of physical domains. One is the three-dimensional acoustic domain for the fluid (air) in the duct, the bottom and back cavities. The other is the two-dimensional domain for the plates, which is modelled based on the Mindlin plate theory. The duct and cavities are modelled by Helmholtz equation using velocity potential ϕ,

$$\left(\nabla^2 - \frac{1}{c_0^2}\frac{\partial^2}{\partial t^2}\right)\phi = 0 . \tag{5.2}$$

The velocity potential ϕ is related to the pressure p and acoustic particle velocity u as,

$$p = -\rho_0 \frac{\partial \phi}{\partial t}, \quad u = \nabla \phi, \tag{5.3}$$

where c_0 is the speed of sound in air, ρ_0 the density of air. The vibroacoustic coupling between the duct, the plate (*a-b-c-d*) and the bottom cavity is modeled as below. The vibration of plate (*a-b-c-d*) is governed by the following equation:

$$m_1 \frac{\partial^2 \eta_1}{\partial t^2} + B_1 \nabla^4 \eta_1 + \Delta p = 0 \,, \tag{5.4}$$

where B_1 is the bending stiffness of the plate, m_1 is the plate mass per unit area, and Δp is the sound pressure difference across the interface at $z = -h/2$,

$$\Delta p = p\,|_{z=(-h/2)+} - p\,|_{z=(-h/2)-} \,. \tag{5.5}$$

Meanwhile, the motion of the plate is also coupled to the sound wave in the duct and bottom cavity by a kinematic condition on both sides of the plate,

$$\frac{\partial \eta_1}{\partial t} = \left.\frac{\partial \phi}{\partial z}\right|_{z=(-h/2)+} = \left.\frac{\partial \phi}{\partial z}\right|_{z=(-h/2)-} \,. \tag{5.6}$$

Equations (5.4)-(5.6) describe the vibroacoustics interaction between the plate (*a-b-c-d*), the duct, and the bottom cavity completely. The vibroacoustics coupling between the plate (*b-e-f-c*), the duct, and the back cavity can be treated in the same way. For frequencies below the first cut-on frequency of the duct, the inlet and exit boundaries are governed by simple travelling wave relationships:

$$\phi_\pm = A_\pm \exp(i\omega t \mp i k_0 x), \qquad p_\pm = \pm \rho_0 c_0 u \,, \tag{5.7}$$

where the two signs of $\pm$ apply to the right-going and left-going waves, respectively. At the exit, an anechoic boundary condition is assumed so that $p = \rho_0 c_0 u$ or,

$$\frac{\partial \phi}{\partial x} + i k_0 \phi = 0 \tag{5.8}$$

At the inlet, the incident sound wave p_i, is mixed with the unknown reflected wave p_r. Noting that the reflected wave p_r, is a simple left-going plane wave, the total sound wave p, the total acoustic particle velocity u, the incident sound wave p_i, the incident acoustic particle velocity u_+, the reflected wave p_r and the reflected acoustic particle velocity u_- satisfy the following relationship,

$$p_r = p - p_i, \quad u_- = u - u_+, \quad p_r = -\rho_0 c_0 u_- . \tag{5.9}$$

Thus,

$$p - p_i = -\rho_0 c_0 (u - u_+), \tag{5.10}$$

$$p + \rho_0 c_0 u = 2 p_i, \tag{5.11}$$

and the boundary condition at the inlet is given as, assuming p_i=1,

$$\frac{\partial \phi}{\partial x} - i k_0 \phi = \frac{2}{\rho_0 c_0} . \tag{5.12}$$

The wall of the duct and cavities are assumed to be acoustically rigid, so the particle velocity normal to the wall vanishes. The boundary condition on the wall is then,

$$\frac{\partial \phi}{\partial \vec{n}} = 0, \tag{5.13}$$

where $\vec{n}$ is the outward normal direction. Equations (5.2)-(5.13) are solved in Femlab® with the plate surface velocity and pressure coupled across the structural and fluid domains, and the transmission loss of the plate silencer is found as,

$$TL = 10 \log_{10} \left(\frac{\int_{exit} |\phi|^2 \, ds}{\int_{inlet} |\phi_i|^2 \, ds} \right) \tag{5.14}$$

where ϕ_i is the velocity potential of the incident wave, and 'inlet' and 'exit' refer to the inlet and exit cross section, respectively. The energy coefficients of sound absorption coefficient (if applicable), α , and sound reflection coefficient, β , are evaluated as,

$$\alpha = 1 - \frac{\int_{inlet} |\phi - \phi_i|^2 \, ds + \int_{exit} |\phi|^2 \, ds}{\int_{inlet} |\phi_i|^2 \, ds}, \tag{5.15}$$

$$\beta = \frac{\int_{inlet} |\phi - \phi_i|^2 \, ds}{\int_{inlet} |\phi_i|^2 \, ds}. \tag{5.16}$$

The hybrid silencer is constructed by adding two dissipative chambers on the two lateral sides of a two-cavity wave reflector. So, the outlook of such a configuration resembles that of a four-cavity wave reflector, and the configuration of the quarter model in Figure 5.1 can also be used to describe the hybrid silencer. Suppose the back cavity is the dissipative chamber, and the bottom cavity is covered by plate and is employed to reflect the incident sound. The governing equations of the sound in the duct and the bottom cavity, as well as the boundary conditions imposed on the inlet, the exit, the cavity and duct walls, and the plates are the same as those for the four-cavity wave reflector. For the dissipative chamber (the back cavity), the sound absorbing material is treated as an equivalent fluid with complex density and speed of sound. Following Mechel and Vér (1992), the wave equation in the sound absorbing material may be established by combining the mass and momentum conservation laws. Similar to sound wave propagation in lossless fluid, a velocity potential can be introduced and is related to sound pressure and velocity perturbations as follows:

$$u = \nabla\phi\,,\ \ p = -\rho_c \frac{\partial\phi}{\partial t}\,,\ \ \left(\nabla^2 - \frac{1}{c_c^2}\frac{\partial^2}{\partial t^2}\right)\phi = 0\,, \tag{5.17}$$

where ρ_c, u, c_c, are, respectively, the complex density, particle velocity and complex speed of sound. The complex density ρ_c and speed of sound c_c are given by empirical formulas using the data of fiberglass (Mechel and Vér, 1992),

$$\begin{cases} \dfrac{c_0}{c_c} = 0.396\mathrm{E}^{-0.458} + i\left(1 + 0.135\mathrm{E}^{-0.646}\right) & (\mathrm{E} \le 0.025) \\ \dfrac{\rho_c c_c}{\rho_0 c_0} = \left(1 + 0.0668\mathrm{E}^{-0.707}\right) - i \times 0.196\mathrm{E}^{-0.549} & (\mathrm{E} \le 0.025) \\ \dfrac{c_0}{c_c} = 0.179\mathrm{E}^{-0.674} + i\left(1 + 0.102\mathrm{E}^{-0.705}\right) & (\mathrm{E} > 0.025) \\ \dfrac{\rho_c c_c}{\rho_0 c_0} = \left(1 + 0.0235\mathrm{E}^{-0.887}\right) - i \times 0.0875\mathrm{E}^{-0.707} & (\mathrm{E} > 0.025) \end{cases}, \tag{5.18}$$

where E is given as,

$$\mathrm{E} = \rho_0 f / R_{sam}\,, \tag{5.19}$$

and the dimensionless flow resistivity, R_{sam}, is found following the normalisation scheme in Chapter 2 as,

$$R_{sam} = \frac{R_{sam}^* h^*}{\rho_0^* c_0^*}\,, \tag{5.20}$$

5.2.2 Model validation

The accuracy of the finite element simulation depends mostly on the mesh model and the solver. To ensure that the simulation is reliable, it is necessary to verify the finite element analysis against a well established method suitable for a simpler configuration. By assuming the duct wall facing plate (*b-e-f-c*) or plate (*a-b-c-d*) to be acoustically rigid, the hybrid silencer becomes a separate plate silencer or

dissipative chamber accordingly. Figure 5.2(a) compares the TL spectrum of the plate silencer simulated by the FEM model with that from the analytical solution following the usual Galerkin procedure of modal expansion in Chapter 2. The cavity geometry is of L = 5h, h_{c1} =h and the properties of the plate (a-b-c-d) are B_1=0.129 and m_1=1.

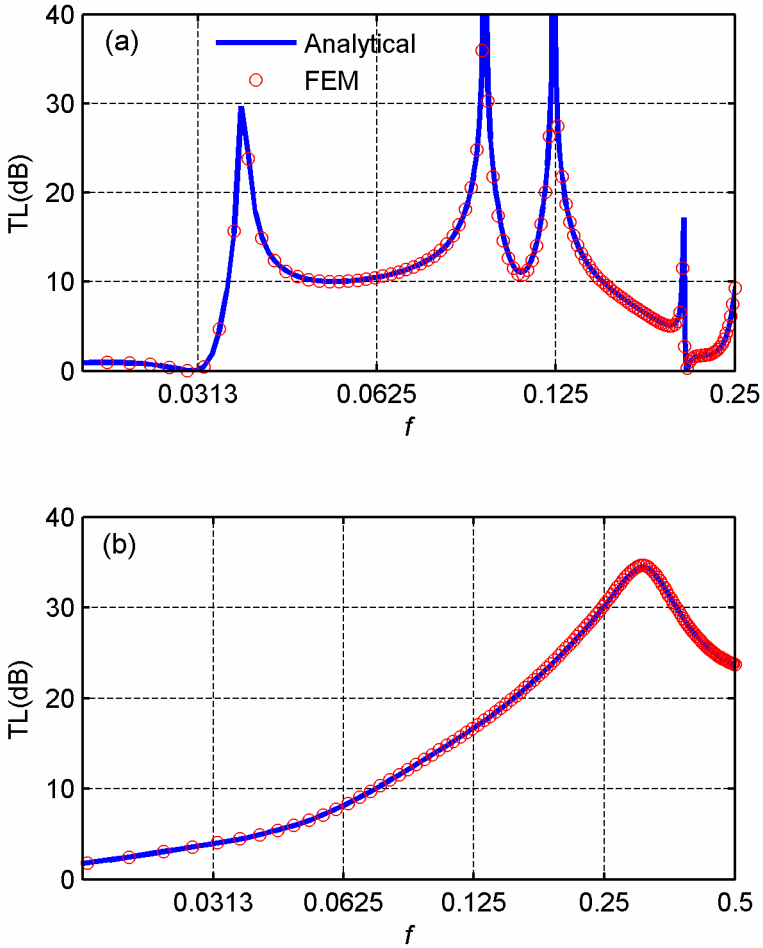

Figure 5.2: Comparison between the FEM simulations (open circles) and the analytical solutions (solid lines). (a) TL spectra of a two-cavity wave reflector. The cavities have a length of L = 5 and depth h_c = 1. The plates with stiffness B=0.129 and mass ratio m=1 are simply-supported at the leading and trailing edges. (b) TL spectra of duct lining filling (flow resistance R_{sam}=1.4) two cavities of depth h_c =1 and length L = 5.

The leading and trailing edges of the plate are simply supported. Figure 5.2(b) compares the simulated spectrum of duct lining filling two cavities of depth $h_{c2} = h$ and $L = 5h$ with that from the analytical solution. The dimensionless flow resistivity is R_{sam}=1.4. The analytical solutions are shown in solid lines, and the FEM simulations are given as open circles. In the FEM simulation, a total of 1792 2nd order Lagrange (isoparametric), hexahedral elements are used for the acoustic domain and 380 2nd order Lagrange, triangular elements are employed for the two dimensional plate, while the number of axial plate modes in the analytical method is 25. As shown in Figures 5.2(a) and 5.2(b), the FEM simulation matches with the analytical results very well, and no visible deviation between the results from the two methods can be observed except at the resonant peaks in Figure 5.2(a). In the design of the plate silencer, the main concern is the stopband in which the *TL* is above a criterion value TL_{cr} over the whole frequency band, and the absolute values at the resonant peaks are of little concern. In light of this, this finite element simulation is regarded as sufficiently accurate for the purpose of this study.

5.3 Three-dimensional wave reflector

5.3.1 Silencing performance

A comparative study is conducted between the three-dimensional and two-dimensional wave reflectors to examine the potential performance improvement by adopting the three-dimensional configuration. To facilitate the comparison, the plate-to-air mass ratio and the total cavity volume are kept equal for all the wave reflectors studied.

Figures 5.3(a), 5.3(b), 5.3(c) and 5.3(d) show the cross sections of four types of three-dimensional wave reflectors, which are designated as plate silencer I, II, III, and IV in the following text, respectively. Plate silencer I is a four-cavity wave reflector and a quarter model for such a configuration has already been given in Figure 1. The four backing cavities are indicated by shadowed area in Figure 5.3(a).

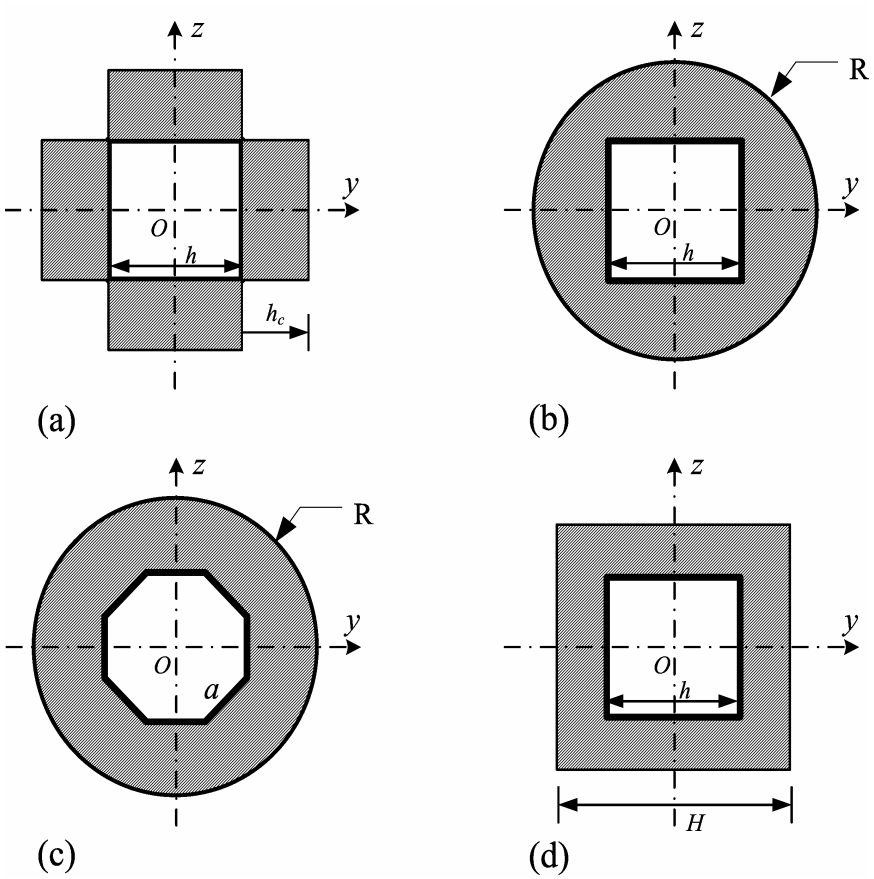

Figure 5.3: Cross sections for the three-dimensional wave reflectors. (a) Four-cavity wave reflector. Four backing cavities with depth h_c are shown in shadowed area. Four plates forming part of the otherwise rigid duct walls are shown in thick solid lines. (b) Rectangular duct with circular chamber of radius *R*. (c) Regular octagon duct with circular chamber of radius *R*. The side length of the octagon *a* satisfies the relationship: $2(1+\sqrt{2})a^2 = h^2$. (d) Rectangular duct with rectangular chamber. The side lengths for the outer and inner square cross sections are *H* and *h*, respectively.

For plate silencer II shown in Figure 5.3(b), the four backing cavities are replaced by a circular chamber of radius *R*, which is also shown in shadowed area. Plate silencer III shown in Figure 5.3(c) is constructed by a regular octagon duct of side length *a* with a circular backing chamber of radius *R*. The last one shown in Figure 5.3(d) is a square duct with a square chamber put outside. For plate silencers I, II, and IV, four plates of width *h* are flush mounted with the duct wall, while for plate silencer III, eight plates of width *a* are required.

The silencing performance of the wave reflectors are affected by several variables related to the backing cavity and plate properties. To simplify the investigation, the following parameters are set as default values,

$$m = 1,\ L = 5,\ \ \Lambda = 10, \tag{5.21}$$

where m is the plate-to-air mass ratio, L is the cavity (or plate) length, and Λ is the total cavity volume, that is, the total added volume occupied by the backing cavities. For instance, assuming the shadowed area in Figure 5.3(a) is S, the total cavity volume Λ of plate silencer I is then defined as,

$$\Lambda = S \cdot L\,. \tag{5.22}$$

The selection for the above default configuration in (5.21) is to facilitate the comparison between the three-dimensional plate silencers and the two-dimensional plate silencer. In Chapter 2, an optimal cavity shape with L=5 and h_c=1 was chosen to investigate the two-cavity plate silencer. So, a total cavity volume $\Lambda = 10$ for the three-dimensional configurations guarantees that the expansion ratios for both the two- and three-dimensional configurations are the same. For each three-dimensional configuration, the bending stiffness of the plate is optimized following the procedure

described in Section 3.3. That is, the optimal bending stiffness yields the widest stopband $f \in [f_1, f_2]$ in which the TL is above a criterion value TL_{cr} over the whole frequency band. As the total cavity volume remains as Λ=10, TL_{cr}=10 dB can still be chosen as the criterion level.

A. Four-cavity wave reflector

Plate silencer I is a four-cavity wave reflector. The properties of the four cavities and plates are assumed to be identical, namely, $h_{c1} = h_{c2} = h_c$, $m_1 = m_2 = m$, and $B_1 = B_2 = B$. For a four-cavity wave reflector with cavity length L and cavity depth h_c, the total cavity volume is,

$$\Lambda = 4Lh_c h, \tag{5.23}$$

where h=1 is the duct height that can be omitted. Such a definition of total cavity volume is equivalent to that for the 2D plate silencer in Huang (2006),

$$\Lambda' = 2L'h_c', \tag{5.24}$$

where, L' and h_c' are the cavity length and depth for the two-cavity configuration. Hence, the two definitions are used equally without further notational distinctions. With m=1, Λ=10, and L=5 given, the following set of optimal results is found:

$$B_{opt}=0.215,\ f_1=0.0341,\ f_2=0.211. \tag{5.25}$$

For the two-cavity configuration, the corresponding maximum stopband found in Chapter 2 is $f \in [0.0353,\ 0.149]$, with the logarithmic bandwidth f_2 / f_1=4.25. Figure 5.4 compares the TL spectra between the four-cavity and two-cavity wave reflectors. As shown in Figure 5.4, the performance improvement of the four-cavity

configuration comes from both higher and lower frequencies, although the difference between the lower frequency limits of the two configurations is very small.

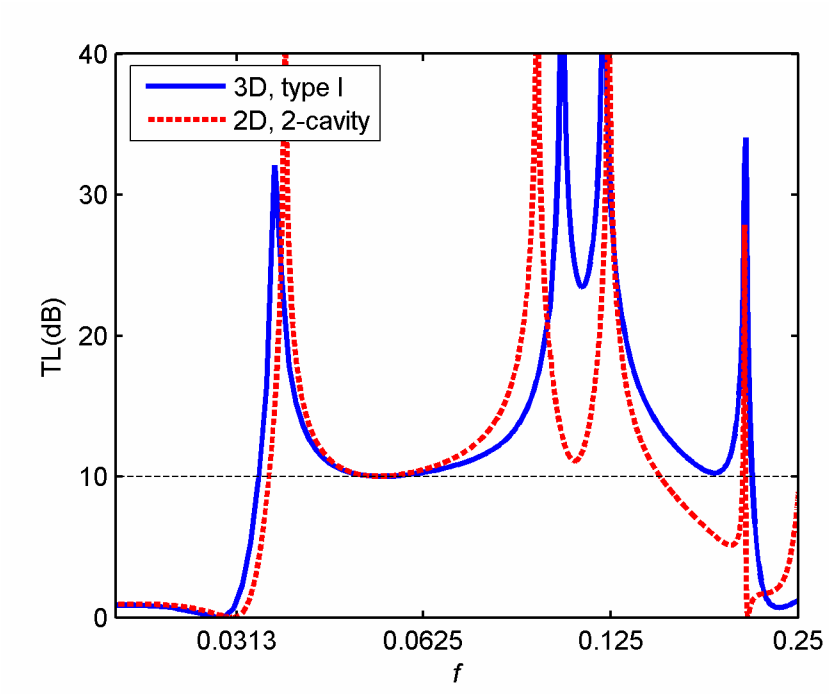

Figure 5.4: TL comparison between the 3D plate silencer I (four-cavity, B_{opt} =0.215) and the 2D design (2-cavity, B_{opt} =0.129). The two configurations have the same cavity volume Λ =10, cavity length L=5, and mass ratio m=1.

As another check for the accuracy of the FEM simulation, the conservation of acoustic energy at the absence of any dissipation mechanism can be examined via Eq. (5.15). In doing so, the absorption coefficient α is regarded as a normalized error, and its absolute value is calculated. As shown in Figure 5.5, the maximum normalized error ($|\alpha|$) is of the order of magnitude of 10^{-8} for the frequency range of interest. A finer mesh may further reduce the normalized error. However, as the error level of the current model is reasonably low enough for the TL calculation, such a mesh refinement is not necessary. The check for the conservation of acoustic

energy is also carried out for Silencers II, III and IV. Similar results are obtained and not repeated here.

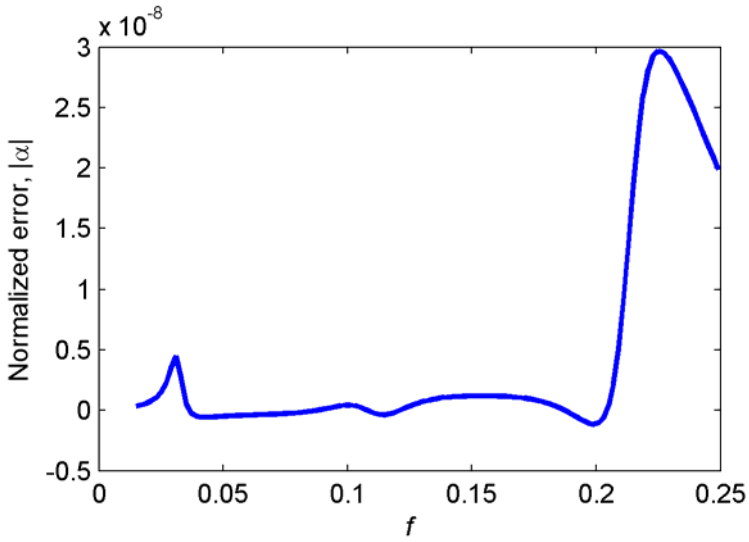

Figure 5.5: Normalized error $|\alpha|$ for the 3D plate silencer I.

B. Rectangular duct with circular chamber

Plate silencer II is constructed by replacing the four rectangular cavities of the four-cavity wave reflector with a circular chamber of radius *R*. The four sides of the rectangular duct are still covered by four plates with leading and trailing edges simply supported. Similar to the four-cavity configuration, a quarter model for the circular design is established for the finite element simulation. The modelling procedure is almost the same as that for plate silencer I except that the four rectangular cavities are replaced by one circular chamber as shown in Figure 5.3(b). The three-dimensional mesh shown in Figure 5.6 is generated by extruding the triangular mesh in one cross section of the chamber along the *x* direction, and a total of 6780 prism (wedge) elements are created for the quarter model. With the cross

section of plate silencer II given in Figure 5.3(b), the total cavity volume of the circular chamber is,

$$\Lambda = (\pi R^2 - h^2)L\,, \tag{5.26}$$

where R and L are the radius and length of the circular chamber, and h=1 is the height of the duct. For the default configuration specified in (5.21), the radius of the circular chamber can be found as $R = \sqrt{\pi/3}$, and the following optimal results are found for plate silencer II:

$$B_{opt} = 0.212,\ \ f_1 = 0.0339,\ \ f_2 = 0.21. \tag{5.27}$$

Figure 5.7 shows the corresponding TL spectrum of plate silencer II (solid line), together with that for the two-cavity design. The optimal stopband for plate silencer II is $f \in$ [0.0339, 0.21] with f_2 / f_1=5.2, which also compares favourably with the stopband $f \in$ [0.0353, 0.149] for the two-cavity design.

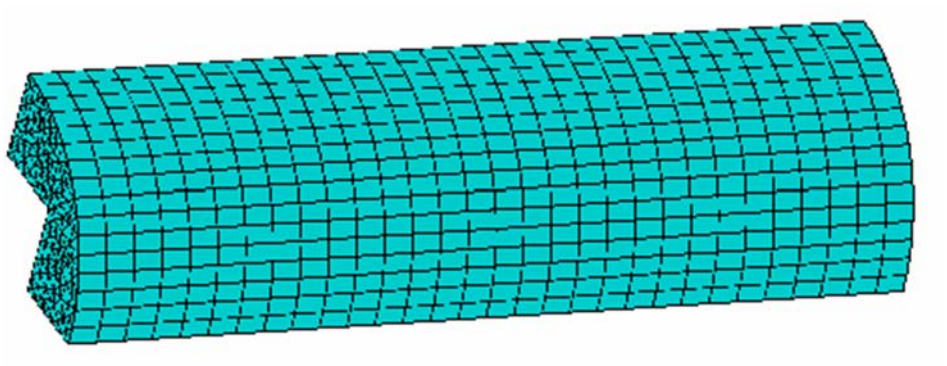

Figure 5.6: Geometry and structured mesh for the circular chamber (quarter model).

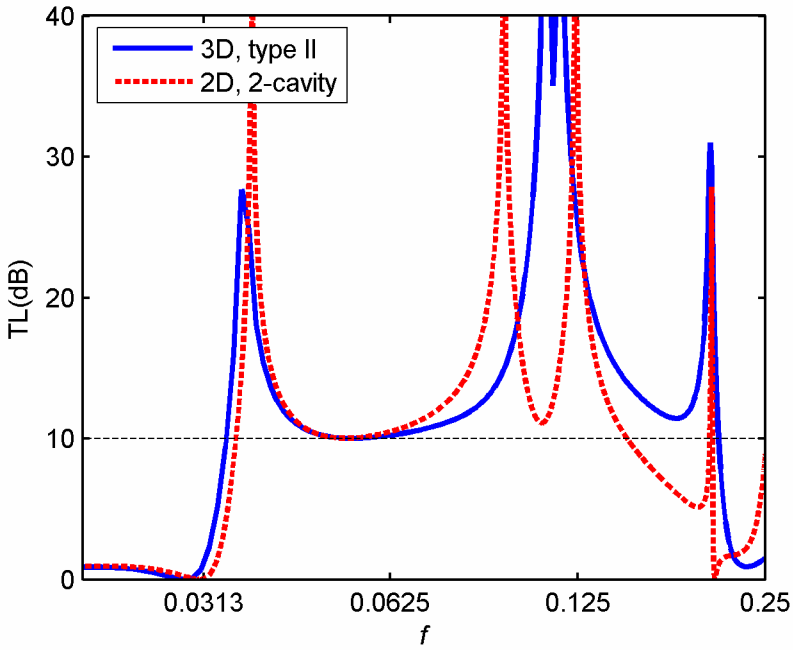

Figure 5.7: TL comparison between the 3D plate silencer II (rectangular duct with circular chamber, B_{opt}=0.212) and the 2D design (2-cavity, B_{opt}=0.129). The two configurations have the same cavity volume Λ=10, cavity length L=5, and mass ratio m=1.

C. Regular octagon duct with circular chamber

Circular ducts are also widely used in industry. Plate silencer III shown in Figure 5.3(c) approximates the circular duct using a regular octagon of side length a. Such a configuration can be simulated in the same way as that for a rectangular duct with circular chamber. The cross section of the octagon duct has the same area A_{oct} as the rectangular duct for plate silencer I and II, that is,

$$A_{oct} = 2\left(1+\sqrt{2}\right)a^2 = h^2 \tag{5.28}$$

where, a is the side length of the regular octagon and h=1 is the height of the rectangular duct. The radius of the circular chamber is also $R=\sqrt{\pi/3}$ so that the

total cavity volume is kept at Λ=10. Following the same optimization procedure, the widest stopband is found with the following set of parameters,

$$B_{opt}=0.188,\quad f_1=0.0335,\quad f_2=0.212. \tag{5.29}$$

The corresponding TL spectrum is shown in Figure 5.8 in solid line.

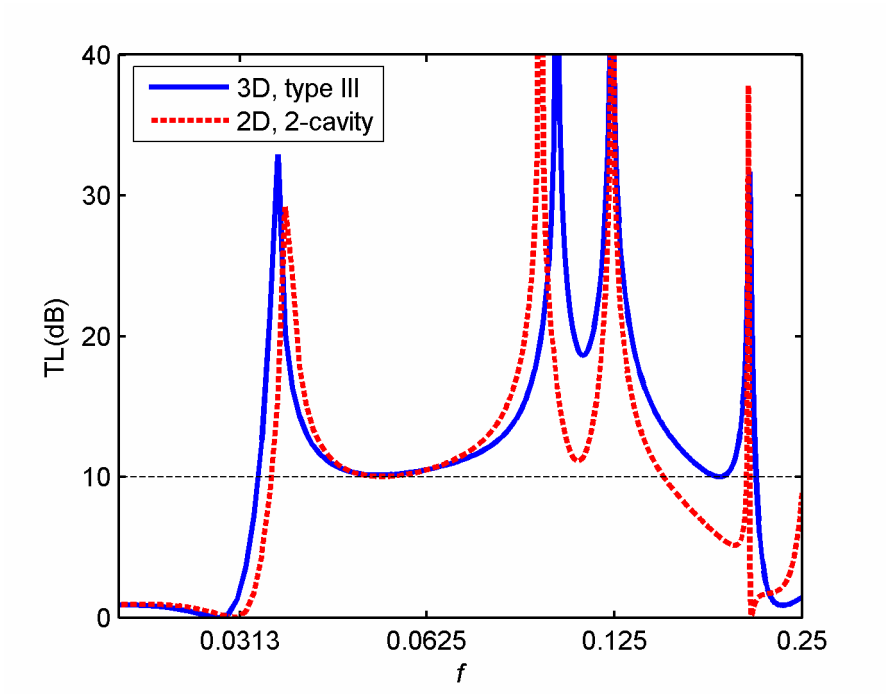

Figure 5.8: TL comparison between the 3D plate silencer III (regular octagon duct with circular chamber, B_{opt}=0.188) and the 2D design (2-cavity, B_{opt}=0.129). The two configurations have the same cavity volume Λ=10, cavity length L=5, and mass ratio m=1.

D. Rectangular duct with rectangular chamber

For plate silencer IV, the four plates covering the square duct are backed by a rectangular chamber of cross section $H \times H$, as shown in Figure 5.3(d). In order to keep the same total cavity volume of the silencer installation, the side length of the

outer rectangular chamber is specified as $H = \sqrt{3}h$. The performance for plate silencer IV is optimized as:

$$B_{opt} = 0.215,\ \ f_1 = 0.0341\ \ f_2 = 0.211, \tag{5.30}$$

and the corresponding TL spectrum is shown in Figure 5.8 in solid line. Unlike in the previous three cases studied, the second and third spectral peaks merge and only three peaks appear in the TL spectrum for plate silencer IV. Nevertheless, plate silencer IV can also achieve a similar wide stopband from 0.0341 to 0.211, as shown in Figure 5.9.

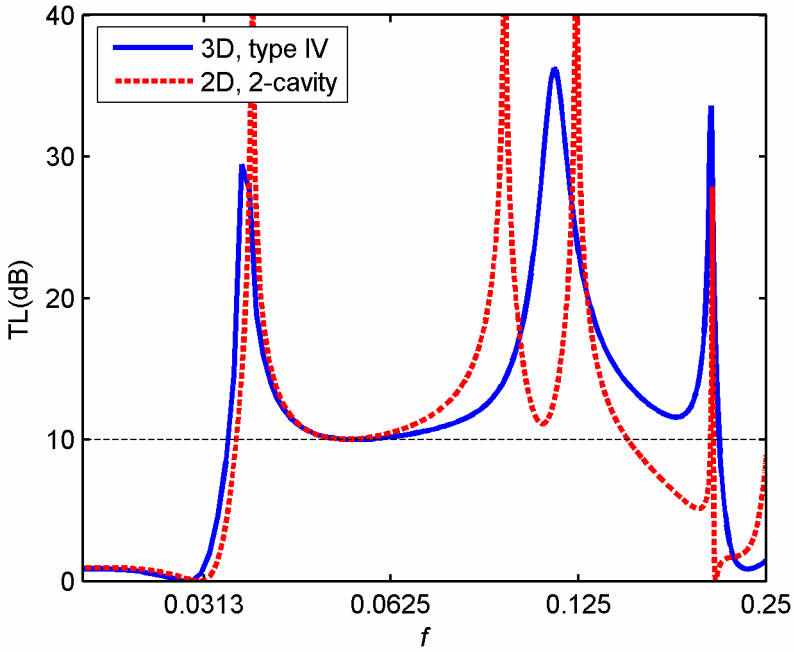

Figure 5.9: TL comparison between the three-dimensional plate silencer II (rectangular duct with rectangular chamber, B_{opt} =0.215) and the two-dimensional design (2-cavity, B_{opt} =0.129). The two configurations have the same cavity volume Λ =10, cavity length L=5, and mass ratio m=1.

So far, four three-dimensional configurations have been simulated. Compared with the two-dimensional design, the three-dimensional configurations have two obvious benefits in common. First, the four three-dimensional silencers have much wider stopbands than the two-dimensional design of the same total cavity volume. Of the four three-dimensional silencers studied, a regular octagon duct with circular chamber (type III) has the highest bandwidth f_2 / f_1=6.33, followed by a rectangular duct with circular chamber (type II, f_2 / f_1=6.20), a four-cavity wave reflector (type I, f_2 / f_1 =6.19), and a rectangular duct with rectangular chamber (type IV, f_2 / f_1 =6.19). Hence, all three-dimensional silencers outperform their two-dimensional counterpart, which gives a maximum bandwidth of f_2 / f_1=4.25. As shown in Figures 5.4, 5.7, 5.8 and 5.9, the three-dimensional design extends the stopband in both lower and higher frequency regions compared with the corresponding two-dimensional design, although the performance improvement in the higher frequency end is more significant than that in the lower frequency region. Second, as the cavity volume is uniformly distributed around the four sides of the duct, the proposed three-dimensional design is more compact in terms of the maximum radial dimension. With the radial dimension reduced, the three-dimensional configuration will fit the situations better where the installation space is limited.

5.3.2. Discussions

Due to the three-dimensional configuration, the sound field inside the duct also becomes complex for plate silencer I to IV. Figure 5.10(a) shows a typical contour of the velocity potential inside the duct at the cross section of x=0 for f=0.05 for plate

silencer I. It is not surprising to see that the velocity potential distribution is no longer uniform along either *y* or *z* direction, and that the near pressure field inside the duct is really three dimensional. However, the plate vibrates in a rather two-dimensional manner, as shown in Figure 5.10(b). The approximate two-dimensional response of the plate allows to investigate the modal vibration contribution to the total sound reflection in a two-dimensional manner in the following vibroacoustics analysis.

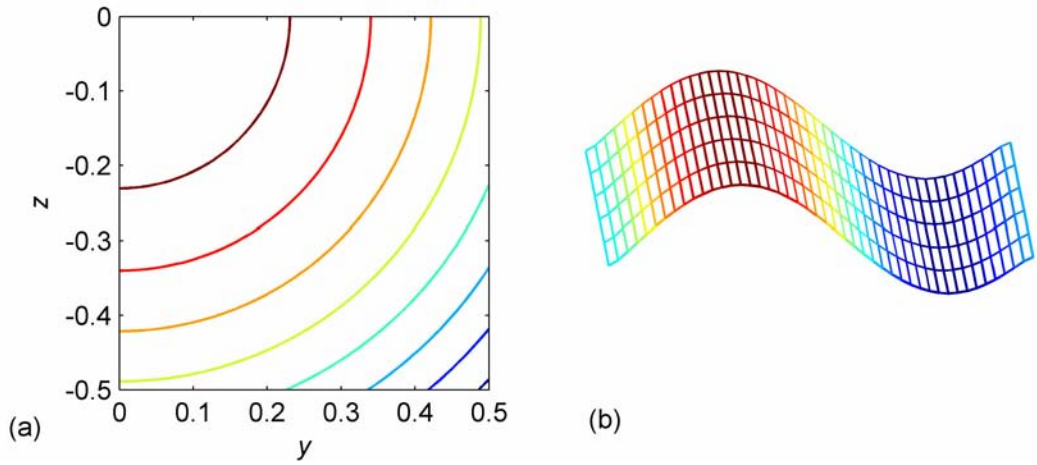

Figure 5.10: Three dimensional effect of the four-cavity wave reflector. (a) Contour of the velocity potential inside the duct at the cross section of *x*=0 for *f*=0.05. (b) Velocity response of the plate at frequency *f*=0.05.

The contributions to sound wave reflections made by different axial modes of the plate are studied. The velocity response of the plate vibration is decomposed into a series of *in vacuo* axial modes $\sin[j\pi(x/L+1/2)]$ with modal amplitude V_j, and the contribution of each single mode towards the total sound reflection p_r is analyzed. In doing so, the plate vibration velocity V is simply averaged over the width of the plate since the plate response is almost two-dimensional, as already

shown in Figure 5.10(b). The contribution of each vibration mode, denoted as $V_j R_j$, towards the total sound reflection p_r is found by projecting the former to the latter. The result is called the modal reflection contribution γ_j, which is defined as below,

$$\gamma_j = \mathrm{Re}\left[V_j R_j \hat{p}_r / |p_r|\right], \tag{5.31}$$

where $\hat{p}_r$ is the conjugate of p_r, and R_j is the complex amplitude of the reflected sound by the induced vibration of the *j*th mode with unit amplitude.

A comparative study is conducted on the vibroacoustic performance between the three-dimensional (regular octagon duct with circular chamber) and two-dimensional (rectangular duct with two opposite cavities) plate silencer designs, as shown in Figure 5.11. The results for the three-dimensional plate silencers are shown in solid lines and those of the two-dimensional design are shown in dashed lines. The configurations for the two silencers are the same as those described in Sec. 5.3.1. Figure 5.11(a) compares the TL spectra between the two types of silencers. The two designs are denoted by ‘3D, Oct’ and ‘2D’ in the figure legends, respectively. The frequency positions of the four peaks of the circular model are marked by vertical dotted lines for easy reference. The sound reflections from all odd modes are lumped as one spectral curve and compared in Figure 5.11(b), and those from the even modes are compared in Figure 5.11(c). The general patterns shown in Figures 5.11(b) and 5.11(c) are similar for both the three- and two-dimensional designs. However, for the odd modes, the three-dimensional design has better reflection at higher frequencies, which can be shown to be mainly from more constructive interference between the first and the third modes instead of from an enhanced first mode. For the even modes,

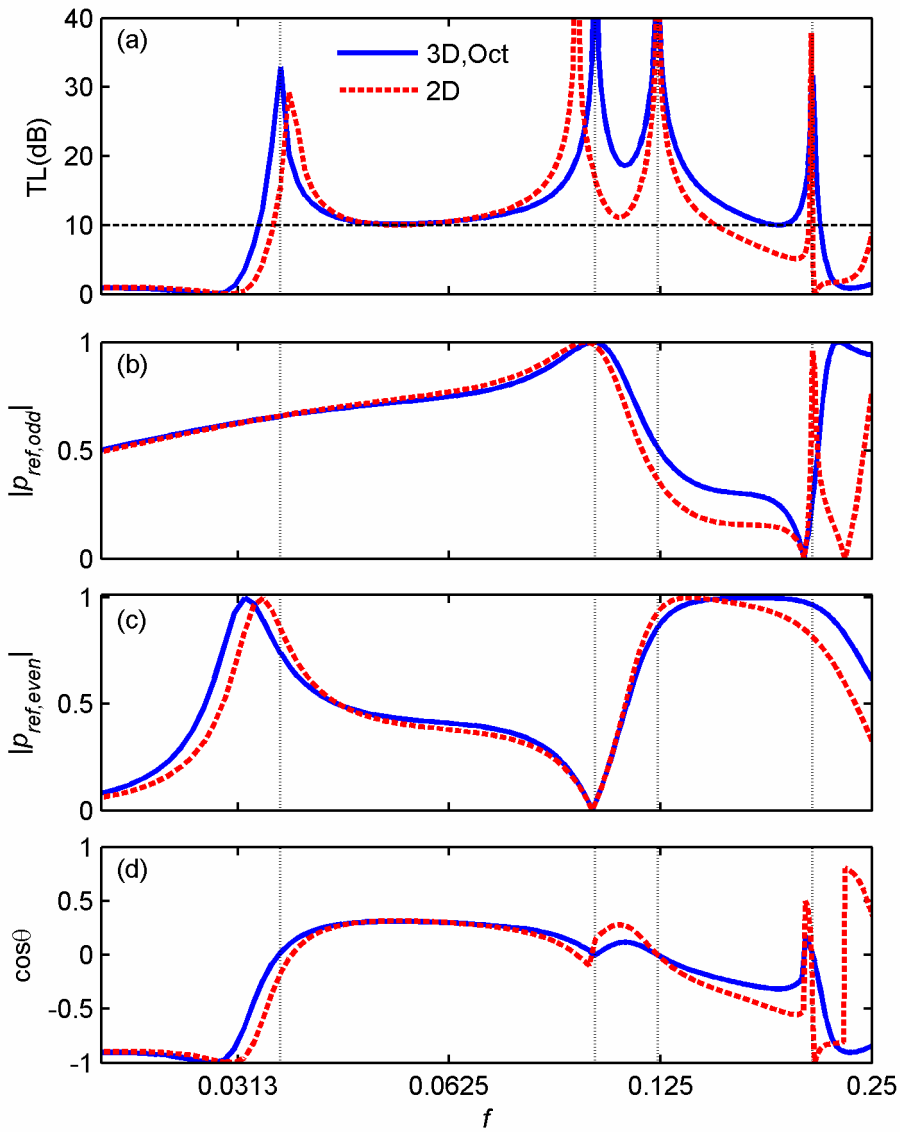

Figure 5.11: Comparison of the optimal performance for the circular wave reflector (3D plate silencer III) with the 2D design of the same total cavity volume $\Lambda = 10$. (a) TL spectra. (b) Contribution by the odd axial modes towards the total sound wave reflection. (c) Contribution by the even axial modes towards the total sound wave reflection. (d) Odd-even interference index. The positions of the three spectral peaks are marked by vertical dotted lines.

the spectrum for the three-dimensional design is stretched out towards lower and higher frequency regions relative to the two-dimensional design. Apart from higher sound reflection, the improved cross-modal interference also accounts for the performance improvement of the three-dimensional model from the two-dimensional model in the relative high frequency, as shown in Figure 5.11(d). The interference index is given by $\cos\theta$, in which θ is the phase angle between the reflected wave from the odd modes and that from the even modes. For frequencies between the third and fourth peaks, the odd-even interference for the three-dimensional silencer is less destructive than that for the two-dimensional silencer, hence, stronger total sound reflection is expected for the three-dimensional design. As a summary, it is pointed out that the three-dimensional design gives better plate response at higher axial modes than the simple two-dimensional (two-cavity) design.

5.4 Hybrid silencer

A hybrid arrangement of plate silencer and traditional duct lining is proposed to combine the advantages of the two noise control methods. The full configuration of the hybrid silencer consists of two opposite reflection cavities and two dissipative chambers. Figure 5.1 can be considered as a quarter model of the hybrid silencer with the bottom cavity working as the reflection cavity, and the back cavity as the dissipative chamber. The two reflection cavities are covered by plates with leading and trailing edges simply supported and other lateral edges free. The two dissipative chambers are filled with sound absorbing material of dimensionless flow resistivity R_{sam}. All four cavities are of length L=5h and depth h_c=h, which is the optimal cavity shape for the two-cavity plate silencer with the volume of $Lh_c = 5h^2$. Such a

configuration is similar to that of the four-cavity wave reflector except that only two out of the four cavities are used to reflect sound.

The performance of the hybrid silencer is optimized with respect to two controlling parameters: the bending stiffness B of the plates and the flow resistance R_{sam} of the sound absorption material. Unlike in the case of wave reflector, the lower boundary limit f_1 is chosen as the cost function above which TL is higher than the criterion value, TL_{cr}. The optimal results found with the following configurations:

$$R_{sam,opt} = 1.4,\ B_{opt} = 0.0627,\ m=1,\ TL_{cr} = 10 \text{ dB}, \tag{5.32}$$

are shown in Figure 5.12. The frequency position of the lower limit f_1 is marked by a vertical line in the figure. As shown in Figure 5.12(a), a wide stopband ranging from $f_1 = 0.0237$ to high frequency is obtained for the hybrid silencer. Figures 5.12(b) and 5.12(c) show the sound energy absorption coefficient, α and the sound energy reflection coefficient, β, respectively. An obvious peak can be observed just below f_1 in Figure 5.12(b), indicating that significant sound absorption occurs due to strong interaction between the plate vibration and the sound absorbing material at that frequency. It is a desirable property that may improve the silencing performance of the hybrid silencer in low frequency. However, in general, sound wave reflection is still the main mechanism for noise reduction in the low frequency region. Sound absorbing materials in the absorption cavities become effective only when the excitation frequency is high enough.

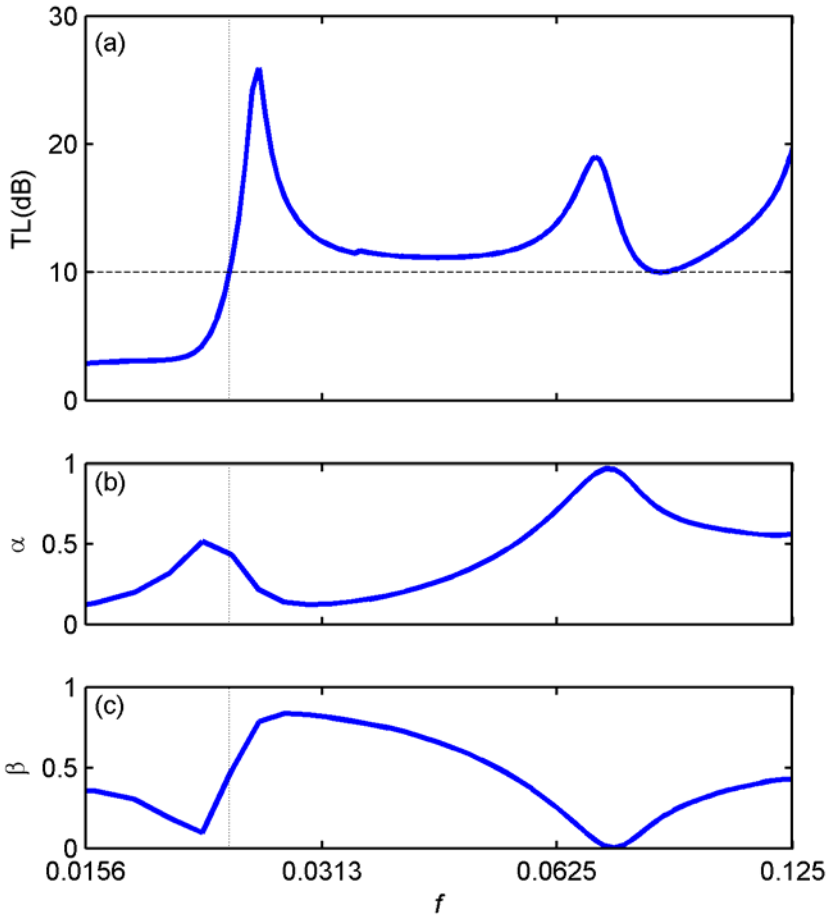

Figure 5.12: Optimal performance of the hybrid silencer. (a) TL. (b) Absorption coefficient, α. (c) Reflection coefficient, β. The optimal bending stiffness B_{opt} =0.0627 and optimal flow resistance $R_{sam,opt}$ =1.4 are obtained with the following parameters given: L =5, h_c =1, m=1.

A comparative study is conducted between the hybrid silencer and pure sound absorption. In doing so, the plates covering the reflection chambers are removed and all the four cavities are filled with sound absorbing materials. Such a device may be called a four-cavity absorptive chamber in the current context. The performance of the four-cavity absorptive chamber with two different configurations is calculated. In the first example, the absorption cavity is of length, L = 5, and depth h_c =1, so that the total cavity volumes of the absorptive chamber and the hybrid silencer are equal. In the second example, the cavity length of the absorptive chamber is extended to L=10 while the cavity depth remains h_c =1. The flow resistivity R_{sam} of the sound absorbing material is optimized in the same way as in the case of the hybrid silencer. With a criterion value TL_{cr} =10 dB, the same optimal flow resistance $R_{sam,opt}$ =1.4 is found for the two configurations. Figure 5.13 compares the TL spectra of the hybrid silencer (solid line) and the four-cavity absorptive chamber (dotted line, L=5; dashed line, L=10). Logarithmic scales are used on both axes. As shown in Figure 5.13, the lower band limits for the three silencers, being marked by open circles for easy identification, are 0.0237, 0.0451 and 0.0284, respectively. The lower boundary of the hybrid silencer (f_1 =0.0237) is almost half of the pure absorptive chamber of the same length L=5 (f_1 =0.0451), which demonstrates a significant improvement in the low frequency region. Doubling the length of the absorptive chamber can reduce its lower boundary to 0.0284 accordingly, but it is still higher than that of the hybrid silencer. Hence, compared with the pure absorptive chamber, one obvious advantage of the hybrid silencer is that it can achieve a good moderate bandwidth with a much reduced total length. However, since the noise reduction at low frequencies is mainly caused by sound reflection, a hybrid silencer cannot achieve better low frequency

performance than a pure wave reflector with the same cavity volume. In Figure 5.14, the solid line shows the TL of the hybrid silencer investigated above, and the dashed line shows that for a four-cavity wave reflector with the following configuration:

$$L = 7.6,\ Lh_c = 5,\ B = 0.81,\ m = 1. \tag{5.33}$$

The lower frequency limits of the hybrid silencer and the 4-cavity wave reflector are f_1 = 0.02 and f_1 =0.0238, respectively, as marked by the two open circles. So, if the main concern is the low frequency performance at the design stage, a wave reflector is preferred.

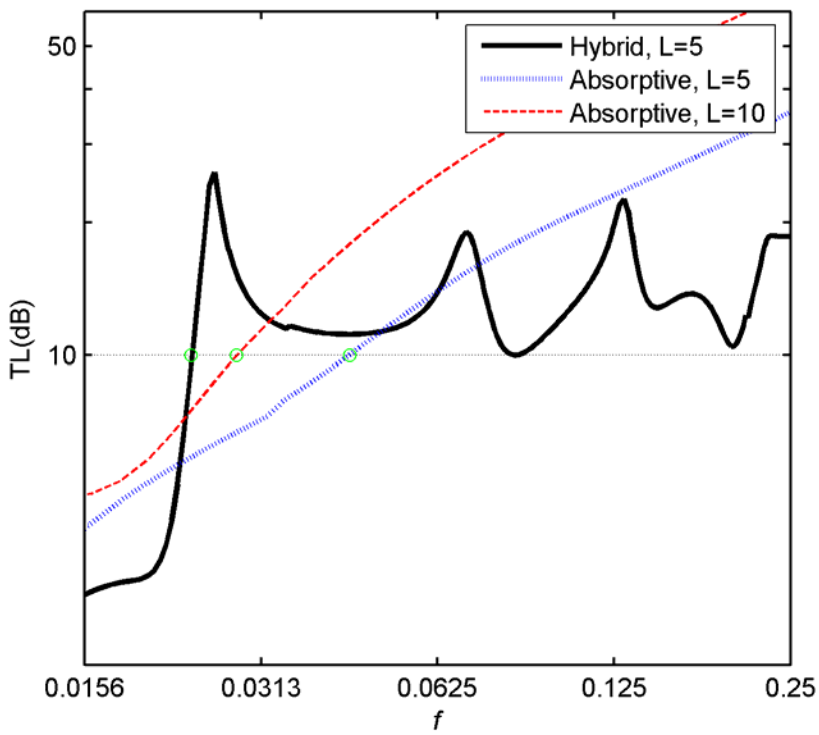

Figure 5.13: TL comparison between the four-cavity hybrid silencer (L=5, B_{opt} =0.0627, $R_{sam,opt}$ =1.4) and a four-cavity absorptive chamber (L=5, 10, $R_{sam,opt}$ =1.4). The cavity depth is h_c=1 for the two designs.

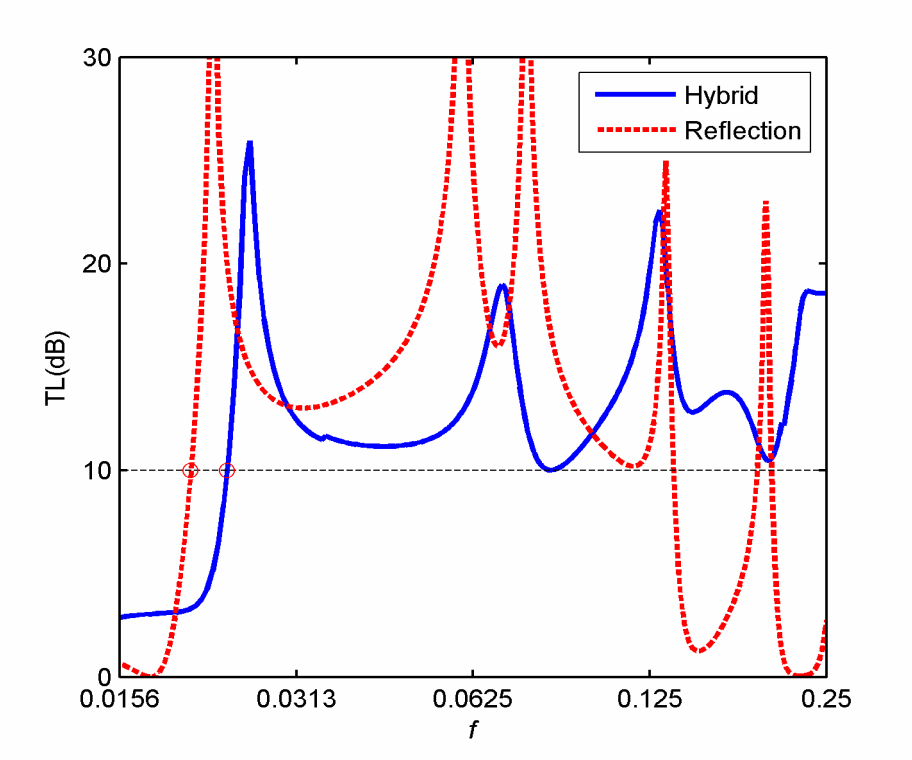

Figure 5.14: TL comparison between a hybrid silencer and a four-cavity wave reflector of the same total cavity volume Λ =20.

5.5. Summary

The acoustic benefit of using three-dimenaional configurations in a plate silencer design has been investigated with a verified finite element model. Numerical results show that the three-dimensional design expand the bandwidth in both lower and higher frequency regions relative to the corresponding two-dimensional design. However, the advantage of adopting a three-dimensional configuration mainly comes from the relatively higher frequency region, and its benefit in low frequency is marginal. Of the four three-dimensional silencers considered, an octagon duct with circular chamber (type III) has the widest bandwidth, followed by a rectangular duct

with circular chamber (type II), a four-cavity wave reflector (type I), and a rectangular duct with rectangular chamber. Vibroacoustics analyses on the plates show that the benefit of the three-dimensional design derives from better plate vibration response from axial modes of higher orders.

A hybrid silencer is proposed to combine the merits of the plate silencer and the traditional duct lining. Under the hybrid arrangement, the two-cavity plate silencer reflects the low-frequency sound waves, while the dissipative chambers attenuate effectively the high frequency sound energy. Compared with the pure absorption design, the hybrid silencer is able to achieve a good broadband noise reduction with much reduced total length. However, as far as the low frequency performance is concerned, a four-cavity wave reflector still outperforms the hybrid silencer with the same total cavity volume.

CHAPTER 6

CONCLUSIONS AND RECOMMENDATIONS

6.1 Summary and conclusions

Low frequency duct noise is difficult to deal with by traditional methods such as porous duct lining and expansion chamber. Lining a duct with porous sound absorbing materials is a very mature and reliable technique that can tackle the medium to high frequency noise easily. However, it does not work well for very low frequencies, for example, below 260 Hz for a $100\,mm \times 100\,mm$ rectangular duct. An expansion chamber type muffler may be used to reflect the low frequency noise, but such a device is usually bulky and passbands exist. Aiming for a broadband passive noise control device that works effectively in the low frequency range, a plate silencer is developed in this study. The working principle of the plate silencer can be described as follows. When a segment of a rigid duct is replaced by a plate covered by a hard-walled cavity, grazing incident sound waves induce plate vibration. The vibration radiates sound towards both ends of the duct. The upstream radiation forms the wave reflection while the downstream radiation combines with the incident wave and destructive acoustic interference then takes places. The principle of acoustic energy conservation guarantees that, whatever amount of sound reflection is, the same amount of reduction is induced in the sound energy flux transmitted to the downstream of the duct. As the sound reflection is solely caused by the plate

vibration, such a device is hence called plate silencer. The silencing performance of the proposed plate silencer is studied theoretically and experimentally in the present study.

A two-dimensional theoretical model is first established for a plate silencer which consists of an expansion chamber with two side-branch cavities covered by light but stiff plates. The leading and trailing edges of the plate can be either simply supported or clamped, while the other two lateral edges are set free. The two-dimensional theoretical model is tested experimentally using balsawood. The spectral peaks and shapes of the measured TL are in agreement with those calculated analytically, which demonstrates that the basic model of the clamped silencer is correct. In the relatively low frequency range, say, below 400Hz for a $100\,mm \times 100\,mm$ rectangular duct, the sound reflection dominates over the sound energy dissipation. Significant sound absorption exists in the plate silencer especially at high frequencies. The exact nature of the damping mechanism has not been identified, but the main mechanism is believed to be the plate damping. A Rayleigh damping model is adopted to represent the plate damping in the theoretical model. Results show that with a proper combination of mass and stiffness damping coefficients, the damping effect can be modelled roughly in agreement with the experimental data.

Based on the validated theoretical model, the silencing performance of the plate silencer is studied theoretically and, effects of various crucial design parameters are identified. The effect of plate mass is generally counterproductive. As the plate-to-air mass ratio increases, the maximum achievable bandwidth decreases, while the required optimal bending stiffness increases. The plate bending stiffness affects the resonant frequencies of the silencer and the TL level between them. It is found that

the plate should have extremely high bending stiffness with low mass ratio in order to achieve a broad stopband. The requirement for the plate properties is out of the reach of common homogeneous materials, but can be satisfied with a sandwich construction. The effect of mean flow on the plate silencer is to decrease its performance. Theoretical study shows that the existence of mean flow smoothes out and shifts the TL peaks. At the same time, the mean flow reduces the overall TL level, but the performance degradation is not critical for the typical flow speeds commonly seen in ventilation systems (e.g., M=0.045). A plate with higher bending stiffness can partially overcome the effect of the mean flow at the expense of reducing the stopband. Because the acoustic leakage due to the unavoidable gap between the plate and the neighbouring duct wall may compromise the performance of the plate silencer, the gap width τ should be adjusted below a certain level, for example, $\tau \leq 0.005$.

Although the leading and trailing edges of the plate can be either clamped or simply supported in the theoretical model, a clamped boundary condition is preferred in practice because of the difficulty associated with the implementation of the simply supported ends. It is found that when a uniform plate is used, the stopband of the clamped plate silencer turns out to be narrower than that of a simply supported one. One qualitative explanation is that the clamped boundary condition reduces the effective radiation length of the plate when responding to the incident sound.

Further numerical study reveals that the performance of the clamped plate silencer can be enhanced by adopting nonuniform plates with softer ends. It is found that, with a proper distribution of bending stiffness along the plate, the clamped plate silencer out-performs the simply supported configuration in every aspect. The

mechanism for the performance improvement is aimed as below. When excited by the incident sound wave, the clamped nonuniform plate responds in a way similar to the simply-supported plate, but the displacement peaks and troughs are much closer to the clamped ends. The extended length between the peaks and troughs increases the ability of the nonuniform plate in reflecting sound like a dipole which is not prohibited by the cavity. Comparisons between the clamped nonuniform plate and the simply supported plate in terms of modal reflection show that the second *in vacuo* mode contributes most to the expansion of stopband of the nonuniform plate silencer, especially in the high frequency region, which, to some extent, conforms to the above explanation.

Sound reflection and absorption mechanisms in a three-dimensional plate silencer are analyzed based on a verified finite element model. Simulation shows that the three-dimensional configuration expands the bandwidth in both lower and higher frequency regions relative to the corresponding two-dimensional design. However, the advantage of adopting a three-dimensional design mainly comes from the relatively higher frequency region, and its benefit at low frequencies is marginal. Vibroacoustic analyses on the plates show that the benefit of three-dimensional design derives from better plate vibration response from axial modes of higher orders. Hybrid arrangement, which combines plate silencer and traditional dissipative chambers in parallel, is also studied to achieve a silencer effective from low to high frequency range. Compared with the pure absorption design, the hybrid silencer is able to achieve a good broadband noise reduction with much reduced total length.

A broadband low frequency plate silencer is realized experimentally using sandwich plate. The cross section of the square duct is 100 *mm*×100 *mm*. The

backing cavity is 500 *mm* long and 100 *mm*. The sandwich plate has a dimensionless bending stiffness of B=0.061 and plate-to-air mass ratio of m=2.4. The prototype plate silencer results in a stopband from 133 Hz to 274 Hz with TL_{cr}=10 dB, in which the porous duct ling is usually ineffective. The plate silencer also outperforms the expansion chamber obviously as the peak TL of the corresponding expansion chamber is less than 5 dB. Sandwich plates with different mechanical properties are also tested and compared, which partially confirms the theoretical findings of the effect of plate properties on the silencer performance. The possibility of predicting the sandwich plate silencer using a simplified mathematical model is also demonstrated. As far as low frequency is concerned, the mathematical model based on homogeneous plates can provide satisfactory prediction on the performance of a sandwich plate silencer. Experimental results are found to be in fair agreement with the predictions.

6.2 Recommendations for future study

The work contained in this thesis provides a theoretical analysis and experimental study of a broadband passive plate silencer in a flow duct. Based on the present study, future work can be carried in the following areas, in order to enhance the understanding of the structure-acoustics interaction as well as to achieve better silencing performance:

1. The present study shows that complete sound reflection takes places at the resonant frequencies (corresponding to the spectral peaks in the TL spectrum) of the plate silencer if the effects of damping and mean flow are excluded. It is believed that a thorough understanding of the formation mechanism of the TL

spectral peaks is not only of academic interest, but may help improve the plate silencer design as well as develop new applications. Although attempts are made to explain the connection between the peak frequencies for the TL spectrum and the plate vibration, there is not yet a clear explanation for the occurrence of the spectral peaks. Hence, further study is suggested to investigate the formation mechanism of the spectral peaks in the TL spectrum.

2. A systematic study on the effect of flow should be carried out. Although the undesirable flow induced vibration is not observed for the typical flow speeds commonly seen in ventilation systems, it does take place at moderate to high flow speeds under certain structural and acoustic boundary conditions. Therefore, it is necessary to identify the limit of the flow speed beyond which the flow induced vibration may pose a problem. Also, it is of great help to fully understand the physics of the coupling between flow, sound and structural vibration. Additionally, a physical explanation for the effect of mean flow should be worked out.

3. Active structures, such as piezoceramic (PZT) actuators and shaped piezofilm (PVDF) sensors, may be integrated on the plate to increase its bending stiffness and/or cancel the plate mass actively. Unlike the existing active noise control system, the proposed active plate silencer does not require additional sensors (microphones) or actuators (loudspeakers) to detect and cancel the incident noise except the active elements integrated on the plate. Thus, such an active device could be much simple while being able to abate the incident noise over a wide frequency range.

APPENDIX

A.1 Limits of $I_2(r,j,l)$ and $I_{2conv}(r,j,l)$ at singular points

$$I_2\Big|_{\mathrm{K}_0^+L/\pi=l\neq j} = -\frac{i(k_0-M\mathrm{K}_0^+)j\pi}{2[(j\pi)^2-(\mathrm{K}_0^+L)^2]} + \frac{j\pi l\pi(k_0+M\mathrm{K}_0^-)\cos(j\pi)[\cos(l\pi)-e^{-i\mathrm{K}_0^-L}]}{[(j\pi)^2-(\mathrm{K}_0^-L)^2][(l\pi)^2-(\mathrm{K}_0^-L)^2]}$$

$$-\frac{jl(k_0-M\mathrm{K}_0^+)[1-\cos(j+l)\pi]}{(l^2-j^2)[(j\pi)^2-(\mathrm{K}_0^+L)^2]} + \frac{jl(k_0+M\mathrm{K}_0^-)[1-\cos(j+l)\pi]}{(l^2-j^2)[(j\pi)^2-(\mathrm{K}_0^-L)^2]}. \qquad \text{(A.1)}$$

$$I_2\Big|_{\mathrm{K}_0^-L/\pi=l\neq j} = \frac{j\pi l\pi(k_0-M\mathrm{K}_0^+)[1-\cos(l\pi)e^{-i\mathrm{K}_0^+L}]}{[(j\pi)^2-(\mathrm{K}_0^+L)^2][(l\pi)^2-(\mathrm{K}_0^+L)^2]} - \frac{i(k_0+M\mathrm{K}_0^-)\cos(j\pi)\cos(l\pi)j\pi}{2[(j\pi)^2-(\mathrm{K}_0^-L)^2]}$$

$$-\frac{jl(k_0-M\mathrm{K}_0^+)[1-\cos(j+l)\pi]}{(l^2-j^2)[(j\pi)^2-(\mathrm{K}_0^+L)^2]} + \frac{jl(k_0+M\mathrm{K}_0^-)[1-\cos(j+l)\pi]}{(l^2-j^2)[(j\pi)^2-(\mathrm{K}_0^-L)^2]}. \qquad \text{(A.2)}$$

$$I_2\Big|_{\mathrm{K}_0^+L/\pi=j\neq l} = -\frac{i(k_0-M\mathrm{K}_0^+)(\cos j\pi\cos l\pi)l\pi}{2[(l\pi)^2-(\mathrm{K}_0^+L)^2]} + \frac{j\pi l\pi(k_0+M\mathrm{K}_0^-)\cos(j\pi)[\cos(l\pi)-e^{-i\mathrm{K}_0^-L}]}{[(j\pi)^2-(\mathrm{K}_0^-L)^2][(l\pi)^2-(\mathrm{K}_0^-L)^2]}$$

$$-\frac{jl(k_0-M\mathrm{K}_0^+)[1-\cos(j+l)\pi]}{(l^2-j^2)[(l\pi)^2-(\mathrm{K}_0^+L)^2]} + \frac{jl(k_0+M\mathrm{K}_n^-)[1-\cos(j+l)\pi]}{(l^2-j^2)[(j\pi)^2-(\mathrm{K}_n^-L)^2]}. \qquad \text{(A.3)}$$

$$I_2\Big|_{\mathrm{K}_0^-L/\pi=j\neq l} = \frac{j\pi l\pi(k_0-M\mathrm{K}_0^+)[1-\cos(l\pi)e^{-i\mathrm{K}_0^+L}]}{[(j\pi)^2-(\mathrm{K}_0^+L)^2][(l\pi)^2-(\mathrm{K}_0^+L)^2]} - \frac{i(k_0+M\mathrm{K}_0^-)l\pi}{2[(l\pi)^2-(\mathrm{K}_0^-L)^2]}$$

$$-\frac{jl(k_0-M\mathrm{K}_0^+)[1-\cos(j+l)\pi]}{(l^2-j^2)[(j\pi)^2-(\mathrm{K}_0^+L)^2]} + \frac{jl(k_0+M\mathrm{K}_0^-)[1-\cos(j+l)\pi]}{(l^2-j^2)[(l\pi)^2-(\mathrm{K}_0^-L)^2]}. \qquad \text{(A.4)}$$

$$I_2\Big|_{\mathrm{K}_0^+L/\pi=j=l} = \left(\frac{1}{8}-\frac{3i}{8\mathrm{K}_0^+L}\right)(k_0-M\mathrm{K}_0^+) + \frac{j\pi l\pi(k_0+M\mathrm{K}_0^-)\cos(j\pi)[\cos(l\pi)-e^{-i\mathrm{K}_0^-L}]}{[(j\pi)^2-(\mathrm{K}_0^-L)^2][(l\pi)^2-(\mathrm{K}_0^-L)^2]}$$

$$+\frac{1}{2}\frac{(k_0+M\mathrm{K}_0^-)(i\mathrm{K}_0^-L)}{(j\pi)^2-(\mathrm{K}_0^-L)^2}. \tag{A.5}$$

$$I_2\Big|_{\mathrm{K}_0^-L/\pi=j=l}=\frac{j\pi l\pi(k_0-M\mathrm{K}_0^+)[1-\cos(l\pi)e^{-i\mathrm{K}_0^+L}]}{[(j\pi)^2-(\mathrm{K}_0^+L)^2][(l\pi)^2-(\mathrm{K}_0^+L)^2]}+\left(\frac{1}{8}-\frac{3i}{8\mathrm{K}_0^-L}\right)(k_0+M\mathrm{K}_0^-)$$

$$+\frac{1}{2}\frac{(k_0-M\mathrm{K}_0^+)(i\mathrm{K}_0^+L)}{(j\pi)^2-(\mathrm{K}_0^+L)^2}. \tag{A.6}$$

$$I_{2conv}\Big|_{\mathrm{K}_0^+L/\pi=l\neq j}=-\frac{(\mathrm{K}_0^+L)(k_0-M\mathrm{K}_0^+)}{2[(j\pi)^2-(\mathrm{K}_0^+L)^2]}-\frac{l\pi(i\mathrm{K}_0^-L)(k_0+M\mathrm{K}_0^-)\cos(j\pi)[e^{-i\mathrm{K}_0^-L}-\cos(l\pi)]}{[(j\pi)^2-(\mathrm{K}_0^-L)^2][(l\pi)^2-(\mathrm{K}_0^-L)^2]}$$

$$+\frac{l(k_0-M\mathrm{K}_0^+)(i\mathrm{K}_0^+L)[1-\cos(j+l)\pi]}{\pi(l^2-j^2)[(j\pi)^2-(\mathrm{K}_0^+L)^2]}+\frac{l(k_0+M\mathrm{K}_0^-)(i\mathrm{K}_0^-L)[1-\cos(j+l)\pi]}{\pi(l^2-j^2)[(j\pi)^2-(\mathrm{K}_0^-L)^2]}. \tag{A.7}$$

$$I_{2conv}\Big|_{\mathrm{K}_0^-L/\pi=l\neq j}=-\frac{l\pi(i\mathrm{K}_0^+L)(k_0-M\mathrm{K}_0^+)[1-\cos(l\pi)e^{-i\mathrm{K}_0^+L}]}{[(j\pi)^2-(\mathrm{K}_0^+L)^2][(l\pi)^2-(\mathrm{K}_0^+L)^2]}$$

$$+\frac{(\mathrm{K}_0^-L)\cos(j\pi)\cos(l\pi)(k_0+M\mathrm{K}_0^-)}{2[(j\pi)^2-(\mathrm{K}_0^-L)^2]}+\frac{l(k_0+M\mathrm{K}_0^-)(i\mathrm{K}_0^-L)[1-\cos(j+l)\pi]}{\pi(l^2-j^2)[(j\pi)^2-(\mathrm{K}_0^-L)^2]}$$

$$+\frac{l(k_0-M\mathrm{K}_0^+)(i\mathrm{K}_0^+L)[1-\cos(j+l)\pi]}{\pi(l^2-j^2)[(j\pi)^2-(\mathrm{K}_0^+L)^2]}. \tag{A.8}$$

$$I_{2conv}\Big|_{\mathrm{K}_0^+L/\pi=j\neq l}=-\frac{l\pi(i\mathrm{K}_0^-L)(k_0+M\mathrm{K}_0^-)\cos(j\pi)[e^{-i\mathrm{K}_0^-L}-\cos(l\pi)]}{[(j\pi)^2-(\mathrm{K}_0^-L)^2][(l\pi)^2-(\mathrm{K}_0^-L)^2]}$$

$$-\frac{l\pi(k_0-M\mathrm{K}_0^+)\cos(j\pi)\cos(l\pi)}{2[(l\pi)^2-(\mathrm{K}_0^+L)^2]}+i\cdot\frac{jl(k_0-M\mathrm{K}_0^+)[1-\cos(j+l)\pi]}{(l^2-j^2)[(l\pi)^2-(\mathrm{K}_0^+L)^2]}$$

$$+\frac{l(k_0+M\mathrm{K}_0^-)(i\mathrm{K}_0^-L)[1-\cos(j+l)\pi]}{\pi(l^2-j^2)[(j\pi)^2-(\mathrm{K}_0^-L)^2]}. \tag{A.9}$$

$$I_{2conv}\Big|_{\mathrm{K}_0^-L/\pi=j\neq l}=-\frac{l\pi(i\mathrm{K}_0^+L)(k_0-M\mathrm{K}_0^+)[1-\cos(l\pi)e^{-i\mathrm{K}_0^+L}]}{[(j\pi)^2-(\mathrm{K}_0^+L)^2][(l\pi)^2-(\mathrm{K}_0^+L)^2]}+\frac{l\pi(k_0+M\mathrm{K}_0^-)}{2[(l\pi)^2-(\mathrm{K}_0^-L)^2]}-$$

$$+\frac{l(k_0-M\mathrm{K}_0^+)(i\mathrm{K}_0^+L)[1-\cos(j+l)\pi]}{\pi(l^2-j^2)[(j\pi)^2-(\mathrm{K}_0^+L)^2]}+i\cdot\frac{jl(k_0+M\mathrm{K}_0^-)[1-\cos(j+l)\pi]}{(l^2-j^2)[(l\pi)^2-(\mathrm{K}_0^-L)^2]}. \quad \text{(A.10)}$$

$$I_{2conv}\Big|_{\mathrm{K}_0^+L/\pi=j=l}=-(\frac{i}{8}+\frac{3}{8\mathrm{K}_0^+L})(k0-M\mathrm{K}_0^+)-\frac{1}{2}\frac{j\pi(k_0+M\mathrm{K}_0^-)}{(j\pi)^2-(\mathrm{K}_0^-L)^2}$$

$$-\frac{l\pi(i\mathrm{K}_0^-L)(k_0+M\mathrm{K}_0^-)\cos(j\pi)[e^{-i\mathrm{K}_0^-L}-\cos(l\pi)]}{[(j\pi)^2-(\mathrm{K}_0^-L)^2][(l\pi)^2-(\mathrm{K}_0^-L)^2]}. \quad \text{(A.11)}$$

$$I_{2conv}\Big|_{\mathrm{K}_0^-L/\pi=j=l}=(\frac{i}{8}+\frac{3}{8\mathrm{K}_0^-L})(k0+M\mathrm{K}_0^-)+\frac{1}{2}\frac{j\pi(k_0-M\mathrm{K}_0^+)}{(j\pi)^2-(\mathrm{K}_0^+L)^2}$$

$$-\frac{l\pi(i\mathrm{K}_0^+L)(k_0-M\mathrm{K}_0^+)[1-\cos(l\pi)e^{-i\mathrm{K}_0^+L}]}{[(j\pi)^2-(\mathrm{K}_0^+L)^2][(l\pi)^2-(\mathrm{K}_0^+L)^2]}. \quad \text{(A.12)}$$

A.2. Coefficients of $I_{cj,p}$~$I_{cl,q}$ in Eq. (3.12)

$$I_{cj,1}=\int_0^1 e^{\beta_j\xi}\cos(r\pi\xi)d\xi=\frac{\beta_j[\cos(r\pi)e^{\beta_j}-1]}{\beta_j^2+(r\pi)^2}. \quad \text{(A.13)}$$

$$I_{cj,2}=\int_0^1 e^{-\beta_j\xi}\cos(r\pi\xi)d\xi=\frac{\beta_j[1-\cos(r\pi)e^{-\beta_j}]}{\beta_j^2+(r\pi)^2}. \quad \text{(A.14)}$$

$$I_{cj,3}=\int_0^1 \sin(\beta_j\xi)\cos(r\pi\xi)d\xi=\frac{\beta_j[1-\cos(\beta_j+r\pi)]}{\beta_j^2-(r\pi)^2}. \quad \text{(A.15)}$$

$$I_{cj,4}=\int_0^1 \cos(\beta_j\xi)\cos(r\pi\xi)d\xi=\frac{\beta_j\sin(\beta_j+r\pi)}{\beta_j^2-(r\pi)^2}. \quad \text{(A.16)}$$

$$I_{cl,1}=\int_0^1 e^{\beta_l\xi}\cos(r\pi\xi)d\xi=\frac{\beta_l[\cos(r\pi)e^{\beta_l}-1]}{\beta_l^2+(r\pi)^2}. \quad \text{(A.17)}$$

$$I_{cl,2} = \int_0^1 e^{-\beta_l \xi} \cos(r\pi\xi) d\xi = \frac{\beta_l [1 - \cos(r\pi) e^{-\beta_l}]}{\beta_l^2 + (r\pi)^2}. \tag{A.18}$$

$$I_{cl,3} = \int_0^1 \sin(\beta_l \xi) \cos(r\pi\xi) d\xi = \frac{\beta_l [1 - \cos(\beta_l + r\pi)]}{\beta_l^2 - (r\pi)^2}. \tag{A.19}$$

$$I_{cl,4} = \int_0^1 \cos(\beta_l \xi) \cos(r\pi\xi) d\xi = \frac{\beta_l \sin(\beta_l + r\pi)}{\beta_l^2 - (r\pi)^2}. \tag{A.20}$$

A.3. Double integration results in Eq. (3.17)

$$\Pi_{1,1} = \frac{k_0 - M\mathrm{K}_r^+}{\beta_j + i\mathrm{K}_r^+ L} \cdot \frac{e^{\beta_j + \beta_l} - 1}{\beta_j + \beta_l} - \frac{k_0 - M\mathrm{K}_r^+}{\beta_j + i\mathrm{K}_r^+ L} \cdot \frac{e^{\beta_l - i\mathrm{K}_r^+ L} - 1}{\beta_l - i\mathrm{K}_r^+ L}$$

$$- \frac{k_0 + M\mathrm{K}_r^-}{\beta_j - i\mathrm{K}_r^- L} \cdot \frac{e^{\beta_j + \beta_l} - 1}{\beta_j + \beta_l} + \frac{k_0 + M\mathrm{K}_r^-}{\beta_j - i\mathrm{K}_r^- L} \cdot \frac{e^{\beta_l} - e^{-i\mathrm{K}_r^- L}}{\beta_l + i\mathrm{K}_r^- L} \cdot e^{\beta_j}, \ (j = l) \tag{A.21a}$$

$$\Pi_{1,1} = -\frac{k_0 - M\mathrm{K}_r^+}{\beta_j - i\mathrm{K}_r^+ L} \cdot \frac{1 - e^{-(\beta_j - \beta_l)}}{\beta_j - \beta_l} + \frac{k_0 - M\mathrm{K}_r^+}{\beta_j - i\mathrm{K}_r^+ L} \cdot \frac{e^{\beta_l - i\mathrm{K}_r^+ L} - 1}{\beta_l - i\mathrm{K}_r^+ L}$$

$$+ \frac{k_0 + M\mathrm{K}_r^-}{\beta_j + i\mathrm{K}_r^- L} \cdot \frac{1 - e^{-(\beta_j - \beta_l)}}{\beta_j - \beta_l} - \frac{k_0 + M\mathrm{K}_r^-}{\beta_j + i\mathrm{K}_r^- L} \cdot \frac{e^{\beta_l} - e^{-i\mathrm{K}_r^- L}}{\beta_l + i\mathrm{K}_r^- L} \cdot e^{-\beta_j}. \ (j \neq l) \tag{A.21b}$$

$$\Pi_{1,2} = -\frac{k_0 - M\mathrm{K}_r^+}{\beta_j - i\mathrm{K}_r^+ L} + \frac{k_0 - M\mathrm{K}_r^+}{\beta_j - i\mathrm{K}_r^+ L} \cdot \frac{e^{\beta_l - i\mathrm{K}_r^+ L} - 1}{\beta_l - i\mathrm{K}_r^+ L}$$

$$+ \frac{k_0 + M\mathrm{K}_r^-}{\beta_j + i\mathrm{K}_r^- L} - \frac{k_0 + M\mathrm{K}_r^-}{\beta_j + i\mathrm{K}_r^- L} \cdot \frac{e^{\beta_l} - e^{-i\mathrm{K}_r^- L}}{\beta_l + i\mathrm{K}_r^- L} \cdot e^{-\beta_j} \tag{A.22}$$

$$\Pi_{1,3} = i\mathrm{K}_r^+ L \cdot \frac{k_0 - M\mathrm{K}_r^+}{\beta_j^2 - (\mathrm{K}_r^+ L)^2} \cdot \frac{(\beta_l \sin\beta_j - \beta_j \cos\beta_j)e^{\beta_l} + \beta_j}{\beta_j^2 + \beta_l^2}$$

$$+ \beta_j \cdot \frac{k_0 - M\mathrm{K}_r^+}{\beta_j^2 - (\mathrm{K}_r^+ L)^2} \cdot \frac{e^{\beta_l - i\mathrm{K}_r^+ L} - 1}{\beta_l - i\mathrm{K}_r^+ L} - \beta_j \cdot \frac{k_0 - M\mathrm{K}_r^+}{\beta_j^2 - (\mathrm{K}_r^+ L)^2} \cdot \frac{(\beta_j \sin\beta_j + \beta_l \cos\beta_j)e^{\beta_l} - \beta_l}{\beta_j^2 + \beta_l^2}$$

$$- \frac{k_0 + M\mathrm{K}_r^-}{\beta_j^2 - (\mathrm{K}_r^- L)^2}(i\mathrm{K}_r^- L \sin\beta_j + \beta_j \cos\beta_j) \cdot \frac{e^{\beta_l} - e^{-i\mathrm{K}_r^- L}}{\beta_l + i\mathrm{K}_r^- L}$$

$$+ i\mathrm{K}_r^- L \cdot \frac{k_0 + M\mathrm{K}_r^-}{\beta_j^2 - (\mathrm{K}_r^- L)^2} \cdot \frac{(\beta_l \sin\beta_j - \beta_j \cos\beta_j)e^{\beta_l} + \beta_j}{\beta_j^2 + \beta_l^2}$$

$$+ \beta_j \cdot \frac{k_0 + M\mathrm{K}_r^-}{\beta_j^2 - (\mathrm{K}_r^- L)^2} \cdot \frac{(\beta_j \sin\beta_j + \beta_l \cos\beta_j)e^{\beta_l} - \beta_l}{\beta_j^2 + \beta_l^2}. \qquad \text{(A.23)}$$

$$\Pi_{1,4} = -i\mathrm{K}_r^+ L \frac{k_0 - M\mathrm{K}_r^+}{\beta_j^2 - (\mathrm{K}_r^+ L)^2} \frac{e^{\beta_l - i\mathrm{K}_r^+ L} - 1}{\beta_l - i\mathrm{K}_r^+ L} + \beta_j \frac{k_0 - M\mathrm{K}_r^+}{\beta_j^2 - (\mathrm{K}_r^+ L)^2} \frac{(\beta_l \sin\beta_j - \beta_j \cos\beta_j)e^{\beta_l} + \beta_j}{\beta_j^2 + \beta_l^2}$$

$$+ i\mathrm{K}_r^+ L \cdot \frac{k_0 - M\mathrm{K}_r^+}{\beta_j^2 - (\mathrm{K}_r^+ L)^2} \cdot \frac{(\beta_j \sin\beta_j + \beta_l \cos\beta_j)e^{\beta_l} - \beta_l}{\beta_j^2 + \beta_l^2}$$

$$\frac{k_0 + M\mathrm{K}_r^-}{\beta_j^2 - (\mathrm{K}_r^- L)^2}(\beta_j \sin\beta_j - i\mathrm{K}_r^- L \cos\beta_j +) \cdot \frac{e^{\beta_l} - e^{-i\mathrm{K}_r^- L}}{\beta_l + i\mathrm{K}_r^- L}$$

$$- \beta_j \cdot \frac{k_0 + M\mathrm{K}_r^-}{\beta_j^2 - (\mathrm{K}_r^- L)^2} \cdot \frac{(\beta_l \sin\beta_j - \beta_j \cos\beta_j)e^{\beta_l} + \beta_j}{\beta_j^2 + \beta_l^2}$$

$$+ i\mathrm{K}_r^- L \cdot \frac{k_0 + M\mathrm{K}_r^-}{\beta_j^2 - (\mathrm{K}_r^- L)^2} \cdot \frac{(\beta_j \sin\beta_j + \beta_l \cos\beta_j)e^{\beta_l} - \beta_l}{\beta_j^2 + \beta_l^2}. \qquad (j=l) \qquad \text{(A.24a)}$$

$$\Pi_{1,4} = \frac{k_0 - M\mathrm{K}_r^+}{\beta_j + i\mathrm{K}_r^+ L} \cdot \frac{e^{\beta_j - \beta_l} - 1}{\beta_j - \beta_l} + \frac{k_0 - M\mathrm{K}_r^+}{\beta_j + i\mathrm{K}_r^+ L} \cdot \frac{e^{-(\beta_l + i\mathrm{K}_r^+ L)} - 1}{\beta_l + i\mathrm{K}_r^+ L}$$

$$- \frac{k_0 + M\mathrm{K}_r^-}{\beta_j - i\mathrm{K}_r^- L} \cdot \frac{e^{\beta_j - \beta_l} - 1}{\beta_j - \beta_l} - \frac{k_0 + M\mathrm{K}_r^-}{\beta_j - i\mathrm{K}_r^- L} \cdot \frac{e^{-\beta_l} - e^{-i\mathrm{K}_r^- L}}{\beta_l - i\mathrm{K}_r^- L} \cdot e^{\beta_j} \qquad (j \neq l) \qquad \text{(A.24b)}$$

$$\Pi_{2,1} = \frac{k_0 - M\mathrm{K}_r^+}{\beta_j + i\mathrm{K}_r^+ L} + \frac{k_0 - M\mathrm{K}_r^+}{\beta_j + i\mathrm{K}_r^+ L} \cdot \frac{e^{-(\beta_l + i\mathrm{K}_r^+ L)} - 1}{\beta_l + i\mathrm{K}_r^+ L}$$

$$-\frac{k_0+M\mathrm{K}_r^-}{\beta_j-i\mathrm{K}_r^-L}-\frac{k_0+M\mathrm{K}_r^-}{\beta_j-i\mathrm{K}_r^-L}\cdot\frac{e^{-\beta_l}-e^{-i\mathrm{K}_r^-L}}{\beta_l-i\mathrm{K}_r^-L}\cdot e^{\beta_j}\,. \tag{A.25}$$

$$\Pi_{2,2}=-\frac{k_0-M\mathrm{K}_r^+}{\beta_j-i\mathrm{K}_r^+L}\cdot\frac{1-e^{-(\beta_j+\beta_l)}}{\beta_j+\beta_l}+\frac{k_0-M\mathrm{K}_r^+}{\beta_j-i\mathrm{K}_r^+L}\cdot\frac{1-e^{-(\beta_l+i\mathrm{K}_r^+L)}}{\beta_l+i\mathrm{K}_r^+L}$$

$$+\frac{k_0+M\mathrm{K}_r^-}{\beta_j+i\mathrm{K}_r^-L}\cdot\frac{1-e^{-(\beta_j+\beta_l)}}{\beta_j+\beta_l}-\frac{k_0+M\mathrm{K}_r^-}{\beta_j+i\mathrm{K}_r^-L}\cdot\frac{e^{-i\mathrm{K}_r^-L}-e^{-\beta_l}}{\beta_l-i\mathrm{K}_r^-L}\cdot e^{-\beta_j}\,. \tag{A.26}$$

$$\Pi_{2,3}=i\mathrm{K}_r^+L\cdot\frac{k_0-M\mathrm{K}_r^+}{\beta_j^2-(\mathrm{K}_r^+L)^2}\cdot\frac{-(\beta_l\sin\beta_j+\beta_j\cos\beta_j)e^{-\beta_l}+\beta_j}{\beta_j^2+\beta_l^2}$$

$$-\beta_j\cdot\frac{k_0-M\mathrm{K}_r^+}{\beta_j^2-(\mathrm{K}_r^+L)^2}\cdot\frac{(\beta_j\sin\beta_j-\beta_l\cos\beta_j)e^{-\beta_l}+\beta_l}{\beta_j^2+\beta_l^2}$$

$$+\beta_j\cdot\frac{k_0-M\mathrm{K}_r^+}{\beta_j^2-(\mathrm{K}_r^+L)^2}\cdot\frac{1-e^{-(\beta_l+i\mathrm{K}_r^+L)}}{\beta_l+i\mathrm{K}_r^+L}$$

$$-\frac{k_0+M\mathrm{K}_r^-}{\beta_j^2-(\mathrm{K}_r^-L)^2}(i\mathrm{K}_r^-L\sin\beta_j+\beta_j\cos\beta_j)\cdot\frac{e^{-i\mathrm{K}_r^-L}-e^{-\beta_l}}{\beta_l-i\mathrm{K}_r^-L}$$

$$+i\mathrm{K}_r^-L\cdot\frac{k_0+M\mathrm{K}_r^-}{\beta_j^2-(\mathrm{K}_r^-L)^2}\cdot\frac{-(\beta_l\sin\beta_j+\beta_j\cos\beta_j)e^{-\beta_l}+\beta_j}{\beta_j^2+\beta_l^2}$$

$$+\beta_j\cdot\frac{k_0+M\mathrm{K}_r^-}{\beta_j^2-(\mathrm{K}_r^-L)^2}\cdot\frac{(\beta_j\sin\beta_j-\beta_l\cos\beta_j)e^{-\beta_l}+\beta_l}{\beta_j^2+\beta_l^2}\,. \tag{A.27}$$

$$\Pi_{2,4}=\beta_j\cdot\frac{k_0-M\mathrm{K}_r^+}{\beta_j^2-(\mathrm{K}_r^+L)^2}\cdot\frac{-(\beta_l\sin\beta_j+\beta_j\cos\beta_j)e^{-\beta_l}+\beta_j}{\beta_j^2+\beta_l^2}$$

$$-i\mathrm{K}_r^+L\cdot\frac{k_0-M\mathrm{K}_r^+}{\beta_j^2-(\mathrm{K}_r^+L)^2}\cdot\frac{1-e^{-(\beta_l+i\mathrm{K}_r^+L)}}{\beta_l+i\mathrm{K}_r^+L}$$

$$+i\mathrm{K}_r^+L\cdot\frac{k_0-M\mathrm{K}_r^+}{\beta_j^2-(\mathrm{K}_r^+L)^2}\cdot\frac{(\beta_j\sin\beta_j-\beta_l\cos\beta_j)e^{-\beta_l}+\beta_l}{\beta_j^2+\beta_l^2}$$

$$+\frac{k_0+M\mathrm{K}_r^-}{\beta_j^2-(\mathrm{K}_r^-L)^2}(\beta_j\sin\beta_j-i\mathrm{K}_r^-L\cos\beta_j)\cdot\frac{e^{-i\mathrm{K}_r^-L}-e^{-\beta_l}}{\beta_l-i\mathrm{K}_r^-L}$$

$$-\beta_j \cdot \frac{k_0 + M\mathrm{K}_r^-}{\beta_j^2 - (\mathrm{K}_r^- L)^2} \cdot \frac{-(\beta_l \sin\beta_j + \beta_j \cos\beta_j)e^{-\beta_l} + \beta_j}{\beta_j^2 + \beta_l^2}$$

$$+ i\mathrm{K}_r^- L \cdot \frac{k_0 + M\mathrm{K}_r^-}{\beta_j^2 - (\mathrm{K}_r^- L)^2} \cdot \frac{(\beta_j \sin\beta_j - \beta_l \cos\beta_j)e^{-\beta_l} + \beta_l}{\beta_j^2 + \beta_l^2}. \tag{A.28}$$

$$\Pi_{3,1} = -\frac{k_0 - M\mathrm{K}_r^+}{\beta_j + i\mathrm{K}_r^+ L} \cdot \frac{-(i\mathrm{K}_r^+ L \sin\beta_l + \beta_l \cos\beta_l)e^{-i\mathrm{K}_r^+ L} + \beta_l}{\beta_l^2 - (\mathrm{K}_r^+ L)^2}$$

$$+ \frac{k_0 - M\mathrm{K}_r^+}{\beta_j + i\mathrm{K}_r^+ L} \cdot \frac{(\beta_j \sin\beta_l - \beta_l \cos\beta_l)e^{\beta_j} + \beta_l}{\beta_j^2 + \beta_l^2}$$

$$+ \frac{k_0 + M\mathrm{K}_r^-}{\beta_j - i\mathrm{K}_r^- L} \cdot \frac{(i\mathrm{K}_r^- L \sin\beta_l - \beta_l \cos\beta_l) + \beta_l e^{-i\mathrm{K}_r^- L}}{\beta_l^2 - (\mathrm{K}_r^- L)^2} \cdot e^{\beta_j}$$

$$- \frac{k_0 + M\mathrm{K}_r^-}{\beta_j - i\mathrm{K}_r^- L} \cdot \frac{(\beta_j \sin\beta_l - \beta_l \cos\beta_l)e^{\beta_j} + \beta_l}{\beta_j^2 + \beta_l^2}. \tag{A.29}$$

$$\Pi_{3,2} = \frac{k_0 - M\mathrm{K}_r^+}{\beta_j - i\mathrm{K}_r^+ L} \cdot \frac{-(i\mathrm{K}_r^+ L \sin\beta_l + \beta_l \cos\beta_l)e^{-i\mathrm{K}_r^+ L} + \beta_l}{\beta_l^2 - (\mathrm{K}_r^+ L)^2}$$

$$- \frac{k_0 - M\mathrm{K}_r^+}{\beta_j - i\mathrm{K}_r^+ L} \cdot \frac{-(\beta_j \sin\beta_l + \beta_l \cos\beta_l)e^{-\beta_j} + \beta_l}{\beta_j^2 + \beta_l^2}$$

$$- \frac{k_0 + M\mathrm{K}_r^-}{\beta_j + i\mathrm{K}_r^- L} \cdot \frac{(i\mathrm{K}_r^- L \sin\beta_l - \beta_l \cos\beta_l) + \beta_l e^{-i\mathrm{K}_r^- L}}{\beta_l^2 - (\mathrm{K}_r^- L)^2} \cdot e^{-\beta_j}$$

$$\frac{k_0 + M\mathrm{K}_r^-}{\beta_j + i\mathrm{K}_r^- L} \cdot \frac{-(\beta_j \sin\beta_l + \beta_l \cos\beta_l)e^{-\beta_j} + \beta_l}{\beta_j^2 + \beta_l^2}. \tag{A.30}$$

$$\Pi_{3,3} = \frac{(k_0 - M\mathrm{K}_r^+)\beta_j[-(i\mathrm{K}_r^+ L \cdot \sin\beta_l + \beta_l \cdot \cos\beta_l) \cdot e^{-i\mathrm{K}_r^+ L} + \beta_l)}{[\beta_j^2 - (\mathrm{K}_r^+ L)^2][\beta_l^2 - (\mathrm{K}_r^+ L)^2]}$$

$$+ \frac{(k_0 - M\mathrm{K}_r^+)}{2[\beta_j^2 - (\mathrm{K}_r^+ L)^2]} \cdot i\mathrm{K}_r^+ L \cdot \left[\frac{\sin(\beta_j - \beta_l)}{\beta_j - \beta_l} - \frac{\sin(\beta_j + \beta_l)}{\beta_j + \beta_l}\right]$$

$$- \frac{(k_0 - M\mathrm{K}_r^+)}{2[\beta_j^2 - (\mathrm{K}_r^+ L)^2]} \cdot \beta_j \cdot \left[\frac{1 - \cos(\beta_j + \beta_l)}{\beta_j + \beta_l} - \frac{1 - \cos(\beta_j - \beta_l)}{\beta_j - \beta_l}\right]$$

$$-\frac{(k_0+M\mathrm{K}_r^-)(i\mathrm{K}_r^-L\cdot\sin\beta_j\cdot+\beta_j\cdot\cos\beta_j)\cdot([(i\mathrm{K}_r^-L\cdot\sin\beta_l-\beta_l\cos\beta_l)+\beta_l e^{-i\mathrm{K}_r^-L}]}{[\beta_j^2-(\mathrm{K}_r^-L)^2][\beta_l^2-(\mathrm{K}_r^-L)^2]}$$

$$+\frac{(k_0+M\mathrm{K}_r^-)}{2[\beta_j^2-(\mathrm{K}_r^-L)^2]}\cdot i\mathrm{K}_r^-L\cdot\left[\frac{\sin(\beta_j-\beta_l)}{\beta_j-\beta_l}-\frac{\sin(\beta_j+\beta_l)}{\beta_j+\beta_l}\right]$$

$$+\frac{(k_0+M\mathrm{K}_r^-)}{2[\beta_j^2-(\mathrm{K}_r^-L)^2]}\cdot\beta_j\cdot\left[\frac{1-\cos(\beta_j+\beta_l)}{\beta_j+\beta_l}-\frac{1-\cos(\beta_j-\beta_l)}{\beta_j-\beta_l}\right]\quad (j\neq l)\qquad \text{(A.31a)}$$

$$\Pi_{3,3}=\frac{(k_0-M\mathrm{K}_r^+)\beta_j[-(i\mathrm{K}_r^+L\cdot\sin\beta_l+\beta_l\cdot\cos\beta_l)\cdot e^{-i\mathrm{K}_r^+L}+\beta_l)}{[\beta_j^2-(\mathrm{K}_r^+L)^2][\beta_l^2-(\mathrm{K}_r^+L)^2]}$$

$$+\frac{(k_0-M\mathrm{K}_r^+)}{2[\beta_j^2-(\mathrm{K}_r^+L)^2]}\cdot i\mathrm{K}_r^+L\cdot\left[1-\frac{\sin(\beta_j+\beta_l)}{\beta_j+\beta_l}\right]$$

$$-\frac{(k_0-M\mathrm{K}_r^+)}{2[\beta_j^2-(\mathrm{K}_r^+L)^2]}\cdot\beta_j\cdot\left[\frac{1-\cos(\beta_j+\beta_l)}{\beta_j+\beta_l}\right]$$

$$-\frac{(k_0+M\mathrm{K}_r^-)(i\mathrm{K}_r^-L\cdot\sin\beta_j\cdot+\beta_j\cdot\cos\beta_j)\cdot([(i\mathrm{K}_r^-L\cdot\sin\beta_l-\beta_l\cos\beta_l)+\beta_l e^{-i\mathrm{K}_r^-L}]}{[\beta_j^2-(\mathrm{K}_r^-L)^2][\beta_l^2-(\mathrm{K}_r^-L)^2]}$$

$$+\frac{(k_0+M\mathrm{K}_r^-)}{2[\beta_j^2-(\mathrm{K}_r^-L)^2]}\cdot i\mathrm{K}_r^-L\cdot\left[1-\frac{\sin(\beta_j+\beta_l)}{\beta_j+\beta_l}\right]$$

$$+\frac{(k_0+M\mathrm{K}_r^-)}{2[\beta_j^2-(\mathrm{K}_r^-L)^2]}\cdot\beta_j\cdot\left[\frac{1-\cos(\beta_j+\beta_l)}{\beta_j+\beta_l}\right].\qquad (j=l)\qquad \text{(A.31b)}$$

$$\Pi_{3,4}=\frac{(k_0-M\mathrm{K}_r^+)(-i\mathrm{K}_r^+L)[-(i\mathrm{K}_r^+L\cdot\sin\beta_l+\beta_l\cdot\cos\beta_l)\cdot e^{-i\mathrm{K}_r^+L}+\beta_l]}{[\beta_j^2-(\mathrm{K}_r^+L)^2][\beta_l^2-(\mathrm{K}_r^+L)^2]}$$

$$+\frac{(k_0-M\mathrm{K}_r^+)}{2[\beta_j^2-(\mathrm{K}_r^+L)^2]}\cdot\beta_j\cdot\left[\frac{\sin(\beta_j-\beta_l)}{\beta_j-\beta_l}-\frac{\sin(\beta_j+\beta_l)}{\beta_j+\beta_l}\right]$$

$$+\frac{(k_0-M\mathrm{K}_r^+)}{2[\beta_j^2-(\mathrm{K}_r^+L)^2]}\cdot i\mathrm{K}_r^+L\cdot\left[\frac{1-\cos(\beta_j+\beta_l)}{\beta_j+\beta_l}-\frac{1-\cos(\beta_j-\beta_l)}{\beta_j-\beta_l}\right]$$

$$+\frac{(k_0+M\mathrm{K}_r^-)(\beta_j\cdot\sin\beta_j-i\mathrm{K}_r^-L\cdot\cos\beta_j)\cdot[(i\mathrm{K}_r^-L\cdot\sin\beta_l-\beta_l\cos\beta_l)+\beta_l e^{-i\mathrm{K}_r^-L}]}{[\beta_j^2-(\mathrm{K}_r^-L)^2][\beta_l^2-(\mathrm{K}_r^-L)^2]}$$

$$-\frac{(k_0+M\mathrm{K}_r^-)}{2[\beta_j^2-(\mathrm{K}_r^-L)^2]}\cdot\beta_j\cdot\left[\frac{\sin(\beta_j-\beta_l)}{\beta_j-\beta_l}-\frac{\sin(\beta_j+\beta_l)}{\beta_j+\beta_l}\right]$$

$$+\frac{(k_0+M\mathrm{K}_r^-)}{2[\beta_j^2-(\mathrm{K}_r^-L)^2]}\cdot i\mathrm{K}_r^-L\cdot\left[\frac{1-\cos(\beta_j+\beta_l)}{\beta_j+\beta_l}-\frac{1-\cos(\beta_j-\beta_l)}{\beta_j-\beta_l}\right].\ (j\neq l)\qquad\text{(A.32a)}$$

$$\Pi_{3,4}=\frac{(k_0-M\mathrm{K}_r^+)(-i\mathrm{K}_r^+L)[-(i\mathrm{K}_r^+L\cdot\sin\beta_l+\beta_l\cdot\cos\beta_l)\cdot e^{-i\mathrm{K}_r^+L}+\beta_l]}{[\beta_j^2-(\mathrm{K}_r^+L)^2][\beta_l^2-(\mathrm{K}_r^+L)^2]}$$

$$+\frac{(k_0-M\mathrm{K}_r^+)}{2[\beta_j^2-(\mathrm{K}_r^+L)^2]}\cdot\beta_j\cdot\left[1-\frac{\sin(\beta_j+\beta_l)}{\beta_j+\beta_l}\right]$$

$$+\frac{(k_0-M\mathrm{K}_r^+)}{2[\beta_j^2-(\mathrm{K}_r^+L)^2]}\cdot(i\mathrm{K}_r^+L)\cdot\left[\frac{1-\cos(\beta_j+\beta_l)}{\beta_j+\beta_l}\right]$$

$$+\frac{(k_0+M\mathrm{K}_r^-)(\beta_j\cdot\sin\beta_j-i\mathrm{K}_r^-L\cdot\cos\beta_j)\cdot([(i\mathrm{K}_r^-L\cdot\sin\beta_l-\beta_l\cos\beta_l)+\beta_l e^{-i\mathrm{K}_r^-L}]}{[\beta_j^2-(\mathrm{K}_r^-L)^2][\beta_l^2-(\mathrm{K}_r^-L)^2]}$$

$$-\frac{(k_0+M\mathrm{K}_r^-)}{2[\beta_j^2-(\mathrm{K}_r^-L)^2]}\cdot\beta_j\cdot\left[1-\frac{\sin(\beta_j+\beta_l)}{\beta_j+\beta_l}\right]$$

$$+\frac{(k_0+M\mathrm{K}_r^-)}{2[\beta_j^2-(\mathrm{K}_r^-L)^2]}\cdot(i\mathrm{K}_r^-L)\cdot\left[\frac{1-\cos(\beta_j+\beta_l)}{\beta_j+\beta_l}\right].\qquad (j=l)\qquad\text{(A.32b)}$$

$$\Pi_{4,1}=-\frac{k_0-M\mathrm{K}_r^+}{\beta_j+i\mathrm{K}_r^+L}\cdot\frac{(\beta_l\sin\beta_l-i\mathrm{K}_r^+L\cos\beta_l)e^{-i\mathrm{K}_r^+L}+i\mathrm{K}_r^+L}{\beta_l^2-(\mathrm{K}_r^+L)^2}$$

$$+\frac{k_0-M\mathrm{K}_r^+}{\beta_j+i\mathrm{K}_r^+L}\cdot\frac{(\beta_l\sin\beta_l+\beta_j\cos\beta_l)e^{\beta_j}-\beta_j}{\beta_j^2+\beta_l^2}$$

$$+\frac{k_0+M\mathrm{K}_r^-}{\beta_j-i\mathrm{K}_r^-L}\cdot\frac{(\beta_l\sin\beta_l+i\mathrm{K}_r^-L\cos\beta_l)-i\mathrm{K}_r^-L\cdot e^{-i\mathrm{K}_r^-L}}{\beta_l^2-(\mathrm{K}_r^-L)^2}\cdot e^{\beta_j}$$

$$-\frac{k_0+M\mathrm{K}_r^-}{\beta_j-i\mathrm{K}_r^-L}\cdot\frac{(\beta_l\sin\beta_l+\beta_j\cos\beta_l)e^{\beta_j}-\beta_j}{\beta_j^2+\beta_l^2}.\qquad\text{(A.33)}$$

$$\Pi_{4,2}=\frac{k_0-M\mathrm{K}_r^+}{\beta_j-i\mathrm{K}_r^+L}\cdot\frac{(\beta_l\sin\beta_l-i\mathrm{K}_r^+L\cos\beta_l)e^{-i\mathrm{K}_r^+L}+i\mathrm{K}_r^+L}{\beta_l^2-(\mathrm{K}_r^+L)^2}$$

$$-\frac{k_0 - M\mathrm{K}_r^+}{\beta_j - i\mathrm{K}_r^+ L}\cdot\frac{(\beta_l \sin\beta_l - \beta_j \cos\beta_l)e^{-\beta_j} + \beta_j}{\beta_j^2 + \beta_l^2}$$

$$-\frac{k_0 + M\mathrm{K}_r^-}{\beta_j + i\mathrm{K}_r^- L}\cdot\frac{(\beta_l \sin\beta_l + i\mathrm{K}_r^- L\cos\beta_l) - i\mathrm{K}_r^- L\cdot e^{-i\mathrm{K}_r^- L}}{\beta_l^2 - (\mathrm{K}_r^- L)^2}\cdot e^{-\beta_j}$$

$$\frac{k_0 + M\mathrm{K}_r^-}{\beta_j + i\mathrm{K}_r^- L}\cdot\frac{(\beta_l \sin\beta_l - \beta_j \cos\beta_l)e^{-\beta_j} + \beta_j}{\beta_j^2 + \beta_l^2}. \qquad \text{(A.34)}$$

$$\Pi_{4,3} = \frac{(k_0 - M\mathrm{K}_r^+)\beta_j[(\beta_l\cdot\sin\beta_l - i\mathrm{K}_r^+ L\cdot\cos\beta_l)\cdot e^{-i\mathrm{K}_r^+ L} + i\mathrm{K}_r^+ L]}{[\beta_j^2 - (\mathrm{K}_r^+ L)^2][\beta_l^2 - (\mathrm{K}_r^+ L)^2]}$$

$$+\frac{(k_0 - M\mathrm{K}_r^+)}{2[\beta_j^2 - (\mathrm{K}_r^+ L)^2]}\cdot i\mathrm{K}_r^+ L\cdot\left[\frac{1-\cos(\beta_j+\beta_l)}{\beta_j+\beta_l} + \frac{1-\cos(\beta_j-\beta_l)}{\beta_j-\beta_l}\right]$$

$$-\frac{(k_0 - M\mathrm{K}_r^+)}{2[\beta_j^2 - (\mathrm{K}_r^+ L)^2]}\cdot\beta_j\cdot\left[\frac{\sin(\beta_j+\beta_l)}{\beta_j+\beta_l} + \frac{\sin(\beta_j-\beta_l)}{\beta_j-\beta_l}\right]$$

$$-\frac{(k_0 + M\mathrm{K}_r^-)(i\mathrm{K}_r^- L\cdot\sin\beta_j\cdot + \beta_j\cdot\cos\beta_j)\cdot([(\beta_l\sin\beta_l + i\mathrm{K}_r^- L\cdot\cos\beta_l) - i\mathrm{K}_r^- L\cdot e^{-i\mathrm{K}_r^- L}]}{[\beta_j^2 - (\mathrm{K}_r^- L)^2][\beta_l^2 - (\mathrm{K}_r^- L)^2]}$$

$$+\frac{(k_0 + M\mathrm{K}_r^-)}{2[\beta_j^2 - (\mathrm{K}_r^- L)^2]}\cdot i\mathrm{K}_r^- L\cdot\left[\frac{1-\cos(\beta_j+\beta_l)}{\beta_j+\beta_l} + \frac{1-\cos(\beta_j-\beta_l)}{\beta_j-\beta_l}\right]$$

$$+\frac{(k_0 + M\mathrm{K}_r^-)}{2[\beta_j^2 - (\mathrm{K}_r^- L)^2]}\cdot\beta_j\cdot\left[\frac{\sin(\beta_j+\beta_l)}{\beta_j+\beta_l} + \frac{\sin(\beta_j-\beta_l)}{\beta_j-\beta_l}\right] \qquad (j\neq l) \qquad \text{(A.35a)}$$

$$\Pi_{4,3} = \frac{(k_0 - M\mathrm{K}_r^+)\beta_j[(\beta_l\cdot\sin\beta_l - i\mathrm{K}_r^+ L\cdot\cos\beta_l)\cdot e^{-i\mathrm{K}_r^+ L} + i\mathrm{K}_r^+ L)]}{[\beta_j^2 - (\mathrm{K}_r^+ L)^2][\beta_l^2 - (\mathrm{K}_r^+ L)^2]}$$

$$+\frac{(k_0 - M\mathrm{K}_r^+)}{2[\beta_j^2 - (\mathrm{K}_r^+ L)^2]}\cdot i\mathrm{K}_r^+ L\cdot\left[\frac{1-\cos(\beta_j+\beta_l)}{\beta_j+\beta_l}\right]$$

$$-\frac{(k_0 - M\mathrm{K}_r^+)}{2[\beta_j^2 - (\mathrm{K}_r^+ L)^2]}\cdot\beta_j\cdot\left[\frac{\sin(\beta_j+\beta_l)}{\beta_j+\beta_l} + 1\right]$$

$$-\frac{(k_0 + M\mathrm{K}_r^-)(i\mathrm{K}_r^- L\cdot\sin\beta_j\cdot + \beta_j\cdot\cos\beta_j)\cdot([(\beta_l\sin\beta_l + i\mathrm{K}_r^- L\cdot\cos\beta_l) - i\mathrm{K}_r^- L\cdot e^{-i\mathrm{K}_r^- L}]}{[\beta_j^2 - (\mathrm{K}_r^- L)^2][\beta_l^2 - (\mathrm{K}_r^- L)^2]}$$

$$+\frac{(k_0+M\mathrm{K}_r^-)}{2[\beta_j^2-(\mathrm{K}_r^-L)^2]}\cdot i\mathrm{K}_r^-L\cdot\left[\frac{1-\cos(\beta_j+\beta_l)}{\beta_j+\beta_l}\right]$$

$$+\frac{(k_0+M\mathrm{K}_r^-)}{2[\beta_j^2-(\mathrm{K}_r^-L)^2]}\cdot\beta_j\cdot\left[\frac{\sin(\beta_j+\beta_l)}{\beta_j+\beta_l}+1\right]. \qquad (j=l) \qquad \text{(A.35b)}$$

$$\Pi_{4,4}=\frac{(k_0-M\mathrm{K}_r^+)(-i\mathrm{K}_r^+L)[(\beta_l\cdot\sin\beta_l-i\mathrm{K}_r^+L\cdot\cos\beta_l)e^{-i\mathrm{K}_r^+L}+i\mathrm{K}_r^+L]}{[\beta_j^2-(\mathrm{K}_r^+L)^2][\beta_l^2-(\mathrm{K}_r^+L)^2]}$$

$$+\frac{(k_0-M\mathrm{K}_r^+)}{2[\beta_j^2-(\mathrm{K}_r^+L)^2]}\cdot\beta_j\cdot\left[\frac{1-\cos(\beta_j+\beta_l)}{\beta_j+\beta_l}+\frac{1-\cos(\beta_j-\beta_l)}{\beta_j-\beta_l}\right]$$

$$+\frac{(k_0-M\mathrm{K}_r^+)}{2[\beta_j^2-(\mathrm{K}_r^+L)^2]}\cdot i\mathrm{K}_r^+L\cdot\left[\frac{\sin(\beta_j+\beta_l)}{\beta_j+\beta_l}+\frac{\sin(\beta_j-\beta_l)}{\beta_j-\beta_l}\right]$$

$$+\frac{(k_0+M\mathrm{K}_r^-)(\beta_j\cdot\sin\beta_j-i\mathrm{K}_r^-L\cdot\cos\beta_j)\cdot[(\beta_l\sin\beta_l+i\mathrm{K}_r^-L\cdot\cos\beta_l)-i\mathrm{K}_r^-L\cdot e^{-i\mathrm{K}_r^-L}]}{[\beta_j^2-(\mathrm{K}_r^-L)^2][\beta_l^2-(\mathrm{K}_r^-L)^2]}$$

$$-\frac{(k_0+M\mathrm{K}_r^-)}{2[\beta_j^2-(\mathrm{K}_r^-L)^2]}\cdot\beta_j\cdot\left[\frac{1-\cos(\beta_j+\beta_l)}{\beta_j+\beta_l}+\frac{1-\cos(\beta_j-\beta_l)}{\beta_j-\beta_l}\right]$$

$$+\frac{(k_0+M\mathrm{K}_r^-)}{2[\beta_j^2-(\mathrm{K}_r^-L)^2]}\cdot i\mathrm{K}_r^-L\cdot\left[\frac{\sin(\beta_j+\beta_l)}{\beta_j+\beta_l}+\frac{\sin(\beta_j-\beta_l)}{\beta_j-\beta_l}\right]. \qquad (j\neq l) \qquad \text{(A.36a)}$$

$$\Pi_{4,4}=\frac{(k_0-M\mathrm{K}_r^+)(-i\mathrm{K}_r^+L)[(\beta_l\cdot\sin\beta_l-i\mathrm{K}_r^+L\cdot\cos\beta_l)e^{-i\mathrm{K}_r^+L}+i\mathrm{K}_r^+L]}{[\beta_j^2-(\mathrm{K}_r^+L)^2][\beta_l^2-(\mathrm{K}_r^+L)^2]}$$

$$+\frac{(k_0-M\mathrm{K}_r^+)}{2[\beta_j^2-(\mathrm{K}_r^+L)^2]}\cdot\beta_j\cdot\left[\frac{1-\cos(\beta_j+\beta_l)}{\beta_j+\beta_l}\right]$$

$$+\frac{(k_0-M\mathrm{K}_r^+)}{2[\beta_j^2-(\mathrm{K}_r^+L)^2]}\cdot i\mathrm{K}_r^+L\cdot\left[\frac{\sin(\beta_j+\beta_l)}{\beta_j+\beta_l}+1\right]$$

$$+\frac{(k_0+M\mathrm{K}_r^-)(\beta_j\cdot\sin\beta_j-i\mathrm{K}_r^-L\cdot\cos\beta_j)\cdot[(\beta_l\sin\beta_l+i\mathrm{K}_r^-L\cdot\cos\beta_l)-i\mathrm{K}_r^-L\cdot e^{-i\mathrm{K}_r^-L}]}{[\beta_j^2-(\mathrm{K}_r^-L)^2][\beta_l^2-(\mathrm{K}_r^-L)^2]}$$

$$-\frac{(k_0+M\mathrm{K}_r^-)}{2[\beta_j^2-(\mathrm{K}_r^-L)^2]}\cdot\beta_j\cdot\left[\frac{1-\cos(\beta_j+\beta_l)}{\beta_j+\beta_l}\right]$$

$$+\frac{(k_0+M\mathrm{K}_r^-)}{2[\beta_j^2-(\mathrm{K}_r^-L)^2]}\cdot i\mathrm{K}_r^-L\cdot\left[\frac{\sin(\beta_j+\beta_l)}{\beta_j+\beta_l}+1\right]. \qquad (j=l) \qquad \text{(A.36b)}$$

A.3. Integration results used in Eq. (3.18)

$$I_{in,1}=\int_0^1 e^{-i\mathrm{K}_0^+L\xi}e^{\beta_j\xi}d\xi=\frac{e^{\beta_j-i\mathrm{K}_0^+L}-1}{\beta_j-i\mathrm{K}_0^+L}. \qquad \text{(A.37)}$$

$$I_{in,2}=\int_0^1 e^{-i\mathrm{K}_0^+L\xi}e^{-\beta_j\xi}d\xi=\frac{1-e^{-(\beta_j+i\mathrm{K}_0^+L)}}{\beta_j+i\mathrm{K}_0^+L}. \qquad \text{(A.38)}$$

$$I_{in,3}=\int_0^1 e^{-i\mathrm{K}_0^+L\xi}\sin(\beta_j\xi)d\xi=\frac{\beta_j-(i\mathrm{K}_0^+L\sin\beta_j+\beta_j\cos\beta_j)e^{-i\mathrm{K}_0^+L}}{\beta_j^2-(\mathrm{K}_0^+L)^2}. \qquad \text{(A.39)}$$

$$I_{in,4}=\int_0^1 e^{-i\mathrm{K}_0^+L\xi}\cos(\beta_j\xi)d\xi=\frac{(\beta_j\sin\beta_j-i\mathrm{K}_0^+L\cos\beta_j)e^{-i\mathrm{K}_0^+L}+i\mathrm{K}_0^+L}{\beta_j^2-(\mathrm{K}_0^+L)^2}. \qquad \text{(A.40)}$$

REFERENCES

Ackermann, U., Fuchs, H. and Rambausek, N. (1988), "Sound absorbers of a novel membrane construction," *Applied Acoustics* **25**, 197-215.

Ackermann, U., and Fuchs, H. (1989), "Noise reduction in an exhaust stack of a papermill," *Noise Control Engineering Journal* **33**, 57-60.

Allard, J.I. (1993), *Propagation of Sound in Porous Media Modelling Sound Absorption Material*, Elsevier Applied Science, England.

Allen, H.G. (1969), *Analysis and Design of Structural Sandwich Panels*, Pergamon Press, Oxford.

Anderson, J.S. (1977), "The effect of an air flow on a single side branch Helmholtz resonator in a circlar duct," *Journal of Sound and Vibration* **52**, 423-431.

Ashby, M.F and Johnson, K. (2002), *Material and Design: the Art and Science of Material Selection in Product Design*, Butterworth Heinemann, Oxford.

Attenborough, K. (1983), "Acoustical characteristics of rigid fibrous absorbents and granular materials," *the Journal of the Acoustical Society of America* **73**, 785-799.

Batterman SA, Birge H.A. (1995), "HVAC system as emission sources affecting indoor air quality: a critical review," *ASHRAE, HVAC & R. Research Journal* **1,** 61-80.

Bedout, J.M., Franchek, M.A., Bernhard, R.J., and Mongeau, L. (1997), "Adaptive-passive noise control with self-tuning Helmholtz resonators," *Journal of Sound and Vibration* **202**, 109-123.

Bies, D.A., and Hansen, C.H. (1980), "Flow resistance information for acoustical design," *Applied Acoustics* **13**, 357-391.

Blockhintsev, D.I. (1946), *Acoustics of a Nonhomogeneous Moving Medium.* English translation NACA-TM-1399, 1956.

Bokil, V.B. and Shirahatti, U.S. (1994), "A technique for the modal analysis of sound-structure interaction problems," *Journal of Sound and Vibration* **173**, 23-41.

Brown, S. (1964), "Acoustic design of broadcasting studios," *Journal of Sound and Vibration* **1**, 239-257.

Chanaud, R.C. (1994), "Effects of geometry on the resonance frequency of Helmholtz resonators," *Journal of Sound Vibration* **178**, 337-348.

Choi, S. and Kim, Y.H. (2002), "Sound-wave propagation in a membrane-duct," *the Journal of the Acoustical Society of America* **112**, 1749-1752.

Choy, Y.S., and Huang, L. (2002), "Experimental studies of a drumlike silencer," *the Journal of the Acoustical Society of America* **112**, 2026-2035.

Choy, Y.S., and Huang, L. (2003), "Drum silencer with shallow cavity filled with helium," *the Journal of the Acoustical Society of America* **114**, 1477-1486.

Choy, Y.S., and Huang, L. (2005), "Effect of mean flow on the drumlike silencer," *the Journal of the Acoustical Society of America* **118**, 3077-3085.

Davis, D.D., Stokes, G.M., Moore, D., and Stevens, G.L. (1954), "Theoretical and experimental investigation of mufflers with comments on engine exhaust muffler design," *NASA Report* 1192.

Delany, M.E., and Bazley, E.N. (1970), "Acoustical properties of fibrous absorbent materials," *Applied Acoustics* **3**, 105-116.

Doak, P.E. (1973), "Excitation, transmission and radiation of sound from source distributions in hard-walled ducts of finite length. I. The effects of duct cross-section geometry and source distribution space-time pattern," *Journal of Sound and Vibration* **31**, 1-72.

Ellen, C.H. (1973), "The stability of simply supported rectangular surfaces in uniform subsonic flow," *Journal of Sound and Vibration* **40**, 68-72.

Fernyhough, M., Evans, D.V. (1996), "Comparison of a step approximation to an exact solution of acoustic scattering in a uniform-width pipe with non-uniform wall impedance," *The Quarterly Journal of Mechanics and Applied Mathematics* **49**, 419-437.

Ford, R.D. and Mccormick, M.A. (1969), "Panel sound absorbers," *Journal of Sound and Vibration* **10**, 411-423.

Frommhold, W., Fuchs, H.V. and Sheng, S. (1994), "Acoustic performance of membrane absorber," *Journal of Sound and Vibration* **170**, 621-636.

Fry, A. (1988), *Noise Control in Building Services*, Pergamon, Oxford.

Fuchs, H.V. (1993), "Sound absorbers for heavily fouling exhaust gas systems," *Cement Lime Gypsum* **46B**, E185-E191.

Fuchs, H.V. and Zha, X. (1997), "Acrylic-glass sound absorbers in the plenum of the Deutscher Bundestag," *Applied Acoustics* **51**, 211-217.

Grant, A.D., Lawrie, J.B. (2000), "Propagation of fluid-loaded structural waves along a duct with smoothly varying bending characteristics," *The Quarterly Journal of Mechanics and Applied Mathematics* **53**, 299-321.

Hansen, C.H. (1997), "Active noise control - from laboratory to industrial implementation," *Proceedings of Noise-Con 97*, Vol. **2**, 3-38.

Hansen, C.H. (2005), "Current and future industrial applications of active noise control," *Noise Control Engineering Journal* **53,** 181-196.

Hansen, C.H. and Snyder, S.D. (1997) *Active Control of Noise and Vibration*, London, Spon.

Harris, D.D. (1991), *Noise Control Manual: Guidelines for Problem Solving in the Industrial/Commercial Acoustical Environment*, New York, Van Nostrand Reinhold.

Hong Kong Environmental Protection Department (HKEPD), (*2003*), *Guidance Notes for the Management of Indoor Air Quality in Offices and Public Places*, Indoor Air Quality Management Group, Hong Kong.

Horoshenkov, K.V., and Sakagami, K. (2001), "A method to calculate the acoustic response of a thin, baffled, simply supported poroelastic plate," *the Journal of the Acoustical Society of America* **110**, 904-917.

Huang, L. (1999), "A theory of passive duct noise control by flexible panels," *the Journal of the Acoustical Society of America* **106**, 1801-1809.

Huang, L. (2001a), "A theoretical study of passive control of duct noise using panels of varying compliance," *the Journal of the Acoustical Society of America* **109**, 2805-2814.

Huang, L. (2001b), "Viscous flutter of a finite elastic membrane in poiseuille flow," *Journal of Fluids and Structures* **15**, 1061-1088.

Huang, L. (2002), "Modal analysis of a drumlike silencer," *the Journal of the Acoustical Society of America* **112**, 2014-2025.

Huang, L. (2004), "Parametric studies of a drumlike silencer," *Journal of Sound and Vibration* **269,** 467-488.

Huang, L. (2006), "Broadband sound reflection by plates covering side-branch cavities in a duct," *the Journal of the Acoustical Society of America* **119**, 2628-2638.

Huang, L., Choy, Y.S. (2005), "Vibroacoustics of three-dimensional drum silencer," *the Journal of the Acoustical Society of America* **118**, 2313-2320.

Huang, L., Choy, Y.S., So, R.M.C. and Chong, T.L. (2000), "Experimental study of sound propagation in a flexible duct," *the Journal of the Acoustical Society of America* **106**, 1801-1809.

Ingard, K.U. (1994), *Notes on Sound Absorption Technology*, Noise Control Foundation, U.S.A.

Ingard, U., and Pridmore-Brown, D. (1951), "The effect of partitions in the absorptive lining of sound attenuation ducts," *the Journal of the Acoustical Society of America* **23**, 589-590.

Ingard, U. (1953), "On the theory and design of acoustic resonators," *the Journal of the Acoustical Society of America* **25**, 1037-1061.

Inman, D.J. (2001), *Engineering Vibration*, Prentice Hall, Englewood Cliffs, N.J.

Kang, J. and Fuchs, H.V. (1999), "Predicting the absorption of open weave textiles and micro-perforated membranes backed by an air space," *Journal of Sound and Vibration* **220**, 905-920.

Kim, H.S., Hong, J.S. and Oh, J.E. (1998), "Active noise control with active muffler in automotive exhaust systems," *Noise Control Engineering Journal* **41**, 178-183.

Kim, H.Y. and Hwang, W. (2001), "Effect of debonding on natural frequencies and frequency response functions of honeycomb sandwich beams," *Composite Structures* **55**, 51-62.

Kiyama M., Sakagami, K. and Tanigawa M.A. (1998), "A basic study on acoustic properties of double-leaf membranes," *Applied Acoustics* **54**, 239-254.

Kuttruff, H. (2000). *Room Acoustics*, E & FN Spon, New York.

Lawrie, J.B. and Guled, I.M. (2006), "On tuning a reactive silencer by varying the position of an internal membrane," *the Journal of the Acoustical Society of America* **120**, 780-790.

Lee, J. and Swenson, G. (1992), "Compact sound absorbers for low frequencies," *Noise Control Engineering Journal* **38**, 109-117.

Li, D. and Vipperman, J.S. (2004), "On the design of long T-shaped acoustic resonators," *the Journal of the Acoustical Society of America* **116**, 2785-2792.

Li, D. and Cheng, L. (2007), "Acoustically coupled model of an enclosure and a Helmholtz resonator array," *Journal of sound and Vibration* **305**, 272-288.

Li, D., Cheng, L. and Yu, G.H. (2007), "Noise control in enclosures: Modeling and experiments with T-shaped acoustic resonators," *the Journal of the Acoustical Society of America* **122**, 2615-2625.

Lighthill, M.J. (1978), *Waves in Fluids* , Cambridge U.P., Cambridge.

Lim, M.K., Low, S.C., Jiang, L. and Liew, K.M. (1995), "Dynamic characteristics of disbonds in honeycomb structures," *Engineering Structures* **17**, 27-38.

Lingaiah, K. and Suryanarayana, B.G. (1991), “Strength and stiffness of sandwich beams in bending,” *Experimental Mechanics* **31**, 1-7.

Longhouse, R.E. (1976), “Noise mechanism separation and design considerations for low tip-speed, axial-flow fans,” *Journal of Sound and Vibration* 48, 461-474.

Maa, D.-Y, (1975), “Theory of microperforated panel absorber,” *Scientia Sinica*, **18**, 55-71 (in Chinese).

Maa, D.-Y, (1998), “Potential of microperforated panel absorber,” *the Journal of the Acoustical Society of America* **104**, 2861-2866.

Mechel, F.P. (1994), “Helmholtz resonators with slotted neck plates,” *Acustica* **80**, 321-331.

Mechel, F.P., and Ver, I.L. (1992), *Noise and Vibration Control Engineering: Principles and Applications*, edited by Ver, I.L. and Beranek, L.L ,Wiley, New York, Chapter 8.

Munjal, M.L. (1987), *Acoustics of ducts and mufflers with application to exhaust ventilation system design* , John Eiley and Sons.

Munjal, M.L., and Doige, A.G. (1990), “Theory of a two source-location method for direct experimental evaluation of the four-pole parameters of an aeroacoustic element,” *Journal of Sound and Vibration* **141**, 323-333.

Munjal, M.L., Krishnan, S., and Reddy, M.M. (1993), “Flow-acoustic performance of perforated element mufflers with application to design,” *Noise Control Engineering Journal* **40**, 159-167.

Morse, P.M., and Ingard, K.U. (1968), *Theoretical Acoustics*, Princeton University Press, New Jersey.

Nagaya, K., Hano, U., and Suda, A. (2001), “Silencer consisting of two-stage Helmholtz resonator with auto-tuning control,” *the Journal of the Acoustical Society of America* **110**, 289-295.

Nelson, P.A., and Elloitt, S.J. (1993), *Active control of sound*, Academic Press, London.

Nilsson, E., Nilsson, A.C. (2002), "Prediction and measurement of some dynamic properties of sandwich structures with honeycomb and foam cores," *Journal of Sound and Vibration* **251**, 409-430.

Okamoto, Y., Boden, H., and Abom, M. (1994), "Active noise control in ducts via side-branch resonators," *the Journal of the Acoustical Society of America* **96**, 1533-1538.

Pastuszka JS, Kyaw Tha Paw U, Lis DO, Wlazlo A and Ulfig K. (2000), "*Bacteria and fungal aerosol in indoor environment in upper Silesia, Poland,*", Atmospheric Environment, **34**, 3833-3842.

Pelton, H.K. (1993), *Noise Control Management*. New York: Van Nostrand Reihhold

Plantema, F.J. (1966), *Sandwich Construction, the Bending and Buckling of Sandwich Beams, Plates, and Shells*, John Wiley, New York.

Pretlove, A.J., (1965), "Free vibration of a rectangular panel backed by a closed rectangular cavity," *Journal of Sound and Vibration* **2**, 197-209.

Radcliffe, C.J., and Birdsong, C. (2002). "An electronically tunable resonator for noise control," *SAE Transaction* **110** (6), 2097-2013.

Ramamoorthy, S. and Grosh, K. (2002), "A theoretical study of structural acoustic silencers for hydraulic systems," *the Journal of the Acoustical Society of America* **111**, 2097-2108.

Ramamoorthy, S. and Grosh, K. (2003), "Structural acoustic silencers – Design and experiment," *the Journal of the Acoustical Society of America* **114**, 2812-2824.

ROHACELL, (1987), *Technical Manual*, Darmstadt: Röhm GmbH, Germany.

Sakagami, K., Kiyama, M., Morimoto, M. and Takahashi, D. (1996), "Sound absorption of a cavity-backed membrane: a step towards design method for membrane-type absorbers," *Applied Acoustics* **49**, 237-247.

Selament, A. and Lee, I.J. (2003), "Helmholtz resonator with extended neck," *the Journal of the Acoustical Society of America* **113**, 1975-1985.

Seo, S.H. and Kim, Y.H. (2005), "Silencer design by using array resonators for low-frequency band noise reduction," *the Journal of the Acoustical Society of America* **118**, 2332-2338.

Sharland, I.J. (1964), "Sources of noise in axial flow fan," *Journal of Sound and Vibration* **1**, 302-322.

Stewart, G.W. (1928), "The theory of the Herschel-Quincke tube," *Physical Review* **31**, 696-698.

Taki, M., Morishita, T., Kondo, T., and Mori, T. (1991). "Active silencer with side-branch resonator," *Proceedings of Inter-Noise 91*, Sydney, I-INCE, Washington, DC., 533-536.

Tang, S.K., (2005), "On Helmholtz resonators with tapered necks," *Journal of Sound and Vibration* **279**, 1085-1096.

Tang, W.C. and Lin, W.Z. (2003), "Stiff light composite panels for duct noise reduction," *Applied Acoustics* **64**, 511-524.

Utsumi, M. (2001), "Reduction of noise transmission in a duct by termination impedance control of a sidebranch resonator," *ASME Journal of Vibration and Acoustics* **123**, 289-296.

Utsuno H., Tanaka T., Fujikawa T., and Seybert, A.F. (1989), "Transfer function method for measuring characteristic impedance and propagation constant of porous materials," *the Journal of the Acoustical Society of America* 86, 637-643.

Woods, R.I., (1976), *Noise control in Mechanical Services*, John Wiley and Sons.

Yeo, K.S. and Lim, C.W. (1994), "The stability of flow over periodically supported plates-potential flow," *Journal of Fluids and Structures* **8**, 331-354.

Zha, X., Fuchs, H.V. and Drotleff, H. (2002), "Improving the acoustic working conditions for musicians in small spaces," *Applied Acoustics* **63**, 203-221.